Doctoral thesis

Doctoral theses at NTNU, 2021:388

Fredrik Tomas Bjørndalen Wergeland Göthner

Stability and Power Quality Improvements to Facilitate Wide-Scale Deployment of Future Microgrids

NTNU
Norwegian University of Science and Technology
Thesis for the Degree of
Philosophiae Doctor
Faculty of Information Technology and Electrical
Engineering
Department of Electric Power Engineering

NTNU
Norwegian University of
Science and Technology

Fredrik Tomas Bjørndalen Wergeland Göthner

Stability and Power Quality Improvements to Facilitate Wide-Scale Deployment of Future Microgrids

Thesis for the Degree of Philosophiae Doctor

Trondheim, November 2021

Norwegian University of Science and Technology
Faculty of Information Technology and Electrical Engineering
Department of Electric Power Engineering

NTNU
Norwegian University of
Science and Technology

NTNU
Norwegian University of Science and Technology

Thesis for the Degree of Philosophiae Doctor

Faculty of Information Technology and Electrical Engineering
Department of Electric Power Engineering

ISBN 978-82-326-6149-7 (printed ver.)
ISBN 978-82-326-5358-4 (electronic ver.)
ISSN 1503-8181 (printed ver.)
ISSN 2703-8084 (online ver.)

Doctoral theses at NTNU, 2021:388

Printed by NTNU Grafisk senter

Preface

This thesis is submitted to the Norwegian University of Science and Technology (NTNU) in partial fulfillment of the requirements for the degree of Philosophiae Doctor (PhD).

The work has been carried out at the Department of Electric Power Engineering at NTNU. The funding for the work has been provided by CINELDI - Centre for Intelligent Electricity Distribution, an 8-year Research Centre under the FME-scheme (Centre for Environment-Friendly Energy Research, 257626/E20). The centre is funded by the Research Council of Norway and the CINELDI partners.

Acknowledgments

First of all, I would like to express my gratitude to my supervisor, Professor Ole-Morten Midtgård, for the opportunity to undertake the exciting journey that the PhD has been. His guidance, support, and encouragement have been important for the outcome of the work.

I am deeply indebted to my co-supervisor Dr. Raymundo E. Torres-Olguin for his excellent guidance, as well as continuous encouragement throughout the period. His insight into the control of power electronics and continued motivation has been very helpful. In addition, I am grateful for the discussions and feedback from my co-supervisor Professor Morten Hovd.

I would like to express my sincerest gratitude to Dr. Javier Roldán-Pérez, who has been incredibly generous with his time and advice, in addition to providing me the opportunity for a research stay at IMDEA Energy. His feedback and input truly have been invaluable. I am also very grateful for the advice and feedback provided by Dr. Atle Rygg, which has been of great help to the work.

I also want to acknowledge several collaborators and colleagues that I have been fortunate to work with. In particular, I would like to thank Dr. Salvatore D'Arco, Professor Elisabetta Tedeschi, Professor Danilo I. Brandao, Augusto M. S. Alonso, Sondre Berg, Dr. Sigurd H. Jakobsen, Hallvar Haugdal, and Sjur Føyen for their valuable discussions and feedback. In addition, I am grateful to Dr. Santiago Sanchez-Acevedo and Kjell Ljøkelsøy for their help with lab implementations.

The Department of Electric Power Engineering at NTNU has been a great place to carry out my PhD studies, among other things owing to its advanced lab facilities and excellent administrative staff. In addition, I am very grateful for the social environment at the department, particularly between PhD students.

Finally, my wife Ingrid deserves my deepest gratitude for her love and support throughout this journey. Not only have you been continuously encouraging, but you have also helped me in lifting my perspective. I am truly blessed to have you in my life.

Summary

The massive integration of distributed energy resources (DERs) represents a paradigm shift for the traditional power system, which until recently has been dominated by large, centralized power generation units. In addition to being located at lower voltage levels, DERs are typically smaller, intermittent, and interfaced by power electronic converters, thereby presenting substantially different characteristics to conventional synchronous generators. This creates new challenges and opportunities for the operation of power systems. An attractive alternative that has emerged over the past two decades as a response to this trend is the microgrid approach. Microgrids enable an organized implementation of distributed generators (DGs), various ancillary services to the grid, as well as improved reliability and resilience. Nonetheless, there are still pending issues related to the stability and power quality of such grids, particularly in scenarios with a large deployment of DGs. The objective of this work is to develop control strategies and models that target these issues, in order to obtain improved performance for future microgrids.

In particular, to address the stability issue from a system perspective, a centralized controller for improving the microgrid stability margins is proposed. The stability margins of such systems have been shown to be poor, particularly when DGs are located close to each other. Hence, this will likely become more challenging with increased DG deployment. The controller adaptively changes the droop controller gains of the DGs according to the location of the dominant modes in the system. The modes are estimated by using the apparent impedance method, which links impedance measurements with the eigenvalues of the corresponding system. The method does not rely on any information of the system topology or parameter values. It is shown that the proposed controller can greatly enhance the system stability margins while maintaining accurate active power sharing between DGs. In addition, the low communication requirements of the conventional droop control are maintained with the proposed controller. As such, this method enables microgrids with larger amounts of DGs.

To further study the stability of microgrids, a reduced-order model of a DG is also developed. Such models have gained interest in the technical literature for being less computationally expensive and simpler to analyze. Unlike most of the models in the literature, the developed model includes the dynamics of internal control loops and virtual impedances, while simultaneously achieving a low model order. However, reduced-order models are inherently a trade-off between simplicity and accuracy. Therefore, the validity of the model assumptions is investigated, and a method for choosing an appropriate model order is proposed. By using the model, differences between quasi-stationary and transient virtual impedances are shown. In particular, it is analytically demonstrated that the system stability region is larger when using the quasi-stationary virtual impedance.

Finally, a method for improving the power quality of microgrids is proposed. Power quality is an increasing concern for microgrids, due to the widespread use of nonlinear loads. This issue can be addressed by appropriate control of the DGs, such as by incorporating harmonic virtual impedances. However, there exists an inherent trade-off between voltage quality and current harmonic sharing among the DGs. To address this issue, an optimization algorithm is proposed to set the harmonic virtual impedances of DGs in a multibus microgrid. Improving the voltage quality is the main objective of the algorithm, while any degree of harmonic current sharing can be specified as a constraint. The algorithm is executed periodically to account for changes in the grid conditions. While communications are necessary for the functioning of the proposed method, these are not time-critical such that a low-bandwidth communication can be used.

Each of these applications is described in detail and placed in the context of the relevant state-of-the-art. The proposed control schemes and analytical models were validated through numerical simulations and experimental results.

Contents

Preface **i**

Acknowledgments **iii**

Summary **v**

1 Introduction **1**
- 1.1 Background and Motivation 1
- 1.2 Objectives and Scope 4
- 1.3 Overview of Contributions 5
- 1.4 Overview of Publications 6
- 1.5 Outline of the Thesis 7

2 Theoretical Foundations and State of the Art **9**
- 2.1 Control of Distributed Generators 9
  - 2.1.1 Droop Control 11
  - 2.1.2 Inner Controllers 14
  - 2.1.3 Virtual Impedance-Based Control 16
- 2.2 State-Space Analysis 17
  - 2.2.1 DG Model 18
  - 2.2.2 Complete Microgrid Model 18
- 2.3 Reduced Order Modeling 18
  - 2.3.1 Reduced-Order DG Models 19
  - 2.3.2 Approximating Network Dynamics 20
- 2.4 Impedance-Based Small-Signal Modeling 21
  - 2.4.1 Modeling Small-Signal Impedances in Three-Phase Systems 22
  - 2.4.2 Impedance-Based Stability Analysis 24
  - 2.4.3 Apparent Impedance Analysis 25
  - 2.4.4 Vector Fitting 26
- 2.5 Power Quality in Microgrids 27

2.5.1 Harmonic Current Sharing in Microgrids 28
2.5.2 Proposed Control Solutions 29

3 Contributions **31**
3.1 Apparent Impedance-Based Adaptive Controller - Paper I 31
3.1.1 Overview of Proposed Controller 32
3.1.2 Discussion of Control Design 33
3.1.3 Mode Identification Accuracy 35
3.1.4 Simulation Results 35
3.1.5 Main Contribution 37
3.2 Including Realistic Effects in Reduced-Order Converter Modeling - Paper II 37
3.2.1 Simplifying Internal Dynamics 38
3.2.2 Proposed Method for Selecting Model Order 41
3.2.3 Analytical Results 42
3.2.4 Main Contributions 43
3.3 Harmonic Virtual Impedance Design for Optimal Power Quality Management - Paper III 44
3.3.1 Overview of Proposed Optimization Algorithm 44
3.3.2 Analytical Results 46
3.3.3 Main Contributions 47
3.4 Discussion 47

4 Conclusions and Recommendations for Further Work **51**
4.1 Conclusions 51
4.2 Further work 52

Bibliography **64**

Publications **65**
Paper I 67
Paper II 81
Paper III 93

Appendices **107**
A Complete Description of Optimization Algorithm 109
A.1 Notation and Algorithm Overview 109
A.2 Optimization Problem Formulation 110
B Laboratory Facilities 113
B.1 National Smart Grid Laboratory 113
B.2 Smart Energy Integration Lab 114

Chapter 1

Introduction

1.1 Background and Motivation

The traditional power system is currently undergoing unparalleled changes due to the proliferation of renewable energy sources (RES), and it is expected that the future power system will consist of a vast number of distributed generators (DGs). While there are several drivers to this trend, limiting the detrimental effects of global warming is one of the key motivations [1]. Moreover, the rapid development of RES has also improved their competitiveness against other energy sources, to the point where RES are the cheapest source of energy in some places [2]. While the introduction of RES can significantly reduce greenhouse gas emissions from power production, they pose a challenge for the power system planning and operation. Not only are many of these sources intermittent and non-dispatchable, but their control and stability properties are also fundamentally different to those of synchronous machines, which have constituted the lion's share of electricity production [3]. The latter issue stems from the fact that RES are typically interfaced by power electronics converters. In contrast to synchronous machines, the power electronic interfaces have no inherent inertia and introduce faster dynamics. On the other hand, they also allow for faster system response and the possibility to provide various ancillary services [4].

One attractive alternative for interfacing RES together with other technologies that has emerged over the last two decades is the microgrid paradigm [5]. Although a unanimous definition of microgrids is lacking, a commonly cited definition by the U.S. Department of Energy defines a microgrid as [6]:

> *A group of interconnected loads and distributed energy resources within clearly defined electrical boundaries that acts as a single controllable entity with respect to the grid. A microgrid can connect and discon-*

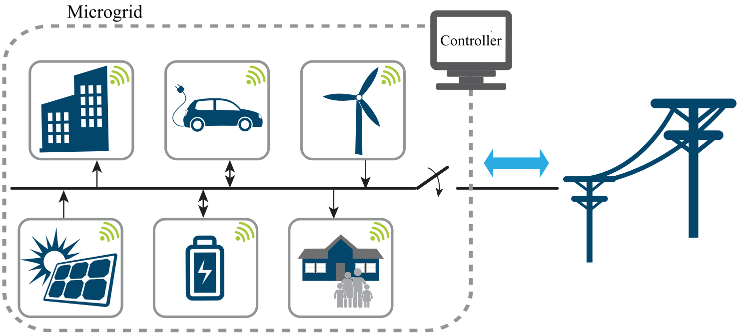

Figure 1.1: Illustration of a microgrid, including DGs, energy storage, loads, a connection to the main grid, and a microgrid controller.

> *nect from the grid to enable it to operate in both grid-connected or island-mode.*

Three of the main attributes of a microgrid are therefore that 1) it contains interconnected loads and distributed production, 2) the microgrid appears as a single unit to the main grid, and 3) the microgrid can operate connected to or independently from the main grid. These elements are illustrated in the microgrid schematic in Fig. 1.1. Appearing as a single unit to the main grid is an important microgrid trait, as active and reactive power injection then can be easily controlled from the distribution system operator (DSO). The ability to operate in island mode is also an advantageous characteristic because it can improve the reliability and resilience of smaller parts of the power system in case of blackouts of the main grid. This has been the main motivation for microgrid development in the United States [1].

In a European context, the main motivation for microgrid development has been the reduction of emissions [1]. Most notably, this is achieved through the introduction of RES. However, having local production also reduces transmission losses in the main grid, which also can contribute to reduced emissions. In a Norwegian context, microgrids are currently considered to avoid or defer distribution system investments, particularly for remote islands. Similarly, microgrids are deemed promising for providing electricity to people living in rural areas without this good, which make up the largest share of the 840 billion people currently living without access to electricity [1,7]. This is because the cost of extending the main grid over longer distances can be substantially higher than establishing a microgrid where the power is needed. In such cases, the microgrid will not have a connection to the main grid and is thus not strictly a microgrid according to the definition above. However, the definitions are usually not interpreted so literally.

Despite its merits, microgrids also have challenges that have been addressed to various degrees in the literature. These challenges include protection issues resulting from bi-directional power flow [4], and regulatory challenges as microgrids do not fit neatly into the current market structure [1]. Of special interest for this thesis are challenges related to stability [8] and power quality [9], which will be explained in greater detail in the following. Although a microgrid in many aspects resembles a smaller version of the conventional power system, some key differences make stability analysis different in these two cases [8]. The small microgrid size typically results in a higher uncertainty, due to the small number of loads as well as the intermittent and highly correlated RES. Moreover, the R/X ratio of the grid is typically larger for microgrids than in the conventional power system due to the lower voltage levels of the former. In addition, microgrids are also characterized by relatively short feeders and small internal converter impedances, which result in very different stability properties compared to the conventional system [10]. Another challenge for stability analysis in microgrids is that the necessary information might not be readily available if multiple DG vendors are used [11]. The reason for this is that the DG control system is typically proprietary, yet it is also largely responsible for the converter dynamics within the bandwidth of the DG. Combined, these factors give microgrids some distinct stability properties, which call for different models and control strategies compared to those of the conventional power system.

For operators of future microgrids, it is crucial to describe these stability properties with accurate models. Such microgrid models can be found in the literature, which typically use very detailed models of the DG. These models accurately describe the DG dynamics and can therefore be used for designing control systems or evaluating the performance of the DG. However, incorporation of the complete dynamics of a large number of converters is intractable for numerical simulations. In addition, the wide timescale of the converters implies that a small time step simulated over a long time is needed to capture the fast and slow dynamics [12]. On the other hand, the wide timescale suggests that reduced-order models could be effective in representing the slow dynamics, as is commonly done in studies of the conventional power system. This can provide an acceptable compromise between model accuracy and numerical efficiency. Yet, while the assumptions of reduced-order models is agreed upon for power system modeling, this is still being researched in a microgrid context [10].

Power quality is another challenge for future microgrids. This is a growing issue due to the increased use of power electronics interfaced loads, such as computers and TVs, LED lighting, charging of electric vehicles, and variable speed motors. These devices draw nonlinear currents, which can be detrimental for the power quality of the grid. In addition, microgrids are often unbalanced, which can further reduce the power quality [13]. This is a serious issue as it can cause reduced lifetime or in the worst case malfunction of components. Power quality issues have traditionally been addressed by using active or passive filters. This provides an adequate solution, but it requires installing extra equipment in the grid. In a microgrid context, the possibility to modify the control of the DGs to address the power quality issues might therefore be a preferred approach. However, if several DGs are used to this end, this should be coordinated to ensure optimal use of the resources.

Both stability and power quality issues have been addressed in the literature by using virtual impedances in the control of DGs [14]. Virtual impedances emulate a physical impedance in a certain range of the bandwidth of the converter. In the context of microgrid stability, this is typically used to increase the impedance magnitude and/or reshape the R/X ratio. Although this technique has been extensively used, there exist some differences in the implementation of the virtual impedances that have not been thoroughly discussed in the literature. In regard to power quality, virtual impedances have been employed at harmonic frequencies to facilitate harmonic current sharing between DGs. However, this approach typically leads to reduced voltage quality, thereby presenting a trade-off between harmonic current sharing and voltage quality. How to design the virtual impedances for improved microgrid performance is therefore still an open question.

The challenges related to stability and power quality are important to address in accomplishing a widespread deployment of microgrids. In particular, they are key in enabling future microgrids with many DGs. Future microgrids should also be characterized by plug-and-play capabilities, as several of the DGs might connect or disconnect depending on the availability of power. However, from a stability point of view, this indicates that the system stability margins might change rapidly. A rapidly changing amount of connected DGs can also significantly affect the power quality improvements provided by the DGs. Hence, flexible control strategies that adapt to changing operating conditions are necessary for realizing future microgrids. In addition, efficient and accurate models are crucial for planning and operating these grids. The aim of this thesis is to answer some of the related challenges and propose control strategies that enable these future microgrids. The following sections will present the scope and contributions of this thesis in more detail.

1.2 Objectives and Scope

The main objective of this thesis is to develop models and control strategies to facilitate a larger deployment of microgrids and DGs. In particular, the modeling and control of DGs for improved stability and power quality of ac microgrids are addressed. The considered DGs are interfaced with a power electronic converter.

In addition, a special emphasis is placed on island operation of the microgrid.

While there exist several control philosophies for managing microgrids, a hierarchical approach with a decentralized primary control has been used a baseline in this thesis. In particular, droop control is used to this end, which is the most common scheme for microgrid applications. The control scheme only needs measurements from the DG terminals to achieve the primary control objective, thereby having a very small communication requirement. Moreover, the scheme enables accurate active power sharing between DGs. However, the stability margins of the basic scheme are known to be poor. The basic scheme also performs poorly with nonlinear loads. In particular, sharing of the nonlinear loads between DGs is not satisfactory for the general case.

In light of these issues, the work in this thesis has been focused on the following research questions:

1. How can the performance of microgrids with droop-controlled DGs be improved, without compromising the benefits of a decentralized approach?
2. How should virtual impedances be designed for improved performance?
3. What DG elements should be represented to obtain a sufficiently accurate model in network stability studies?

1.3 Overview of Contributions

The main contributions of this thesis are summarized in the following:

- An adaptive centralized controller for improving the stability of droop-controlled microgrids was proposed, developed, and experimentally verified. The controller first identifies the system eigenvalues by using the apparent impedance method. Depending on the location of the identified modes, a control law reduces or increases the droop gains of the DGs in the system. The method allows all DGs to collaborate in ensuring adequate system stability margins while maintaining adequate performance. Conditions that guarantee stable operation of the control law are derived.
- An accurate reduced-order model of a DG is developed. The model accounts for virtual impedances and an estimation of the fast dynamics of the converter. By using the model, it is analytically demonstrated that different virtual impedance implementations can give significantly different stability margins. In particular, it is shown that quasi-stationary virtual impedances give a larger system stability region than transient virtual impedances.

- A method for selecting an appropriate order of the reduced-order model is proposed. The model order is selected based on the frequency of the dominant modes.
- An optimization algorithm for calculating the harmonic virtual impedances for DGs in a microgrid is proposed. The algorithm minimizes the voltage Total Harmonic Distortion (THD) in selected microgrid nodes, while ensuring a degree of current harmonic sharing between DGs. The degree of sharing can be varied by changing a parameter of the optimization algorithm, thereby reflecting the trade-off between DG current harmonic sharing and voltage distortion in the microgrid nodes.

1.4 Overview of Publications

The results of this work have been compiled and submitted for publication in scientific journals. The main publications associated with this thesis are listed in the following:

1. **F. Göthner**, R. Torres-Olguin, J. Roldán-Pérez, A. Rygg and O. -M. Midtgard, "Apparent Impedance-Based Adaptive Controller for Improved Stability of Droop-Controlled Microgrid," in *IEEE Transactions on Power Electronics*, vol. 36, no. 8, pp. 9465-9476, Aug. 2021.
2. **F. Göthner**, J. Roldán-Pérez, R. Torres and O. -M. Midtgard, "Reduced-Order Model of Distributed Generators with Internal Loops and Virtual Impedance," in *IEEE Transactions on Smart Grid*, doi: 10.1109/TSG.2021.3120323.
3. **F. Göthner**, J. Roldán-Pérez, R. Torres and O. -M. Midtgard, "Harmonic Virtual Impedance Design for Optimal Management of Power Quality in Microgrids," in *IEEE Transactions on Power Electronics*, vol. 36, no. 9, pp. 10114-10126, Sept. 2021.

In addition, the publications listed below were published as a part of the PhD. These works have not been included in this thesis, either due to being preliminary explorations that were further developed in the main publications or being outside the scope of the final thesis.

1. **F. Göthner**, O. Midtgård, R. Torres-Olguin and S. D'Arco, "Effect of Including Transient Virtual Impedance in Droop-Controlled Microgrids," *2018 IEEE International Conference on Environment and Electrical Engineering and 2018 IEEE Industrial and Commercial Power Systems Europe (EEEIC / I&CPS Europe)*, Palermo, 2018, pp. 1-6.

2. **F. Göthner**, O. Midtgård, R. Torres-Olguin and J. Roldán-Pérez, "Virtual Impedance Design for Power Quality and Harmonic Sharing Improvement in Microgrids," *2019 20th Workshop on Control and Modeling for Power Electronics (COMPEL)*, Toronto, ON, Canada, 2019, pp. 1-7.

3. **F. Göthner**, E. Tedeschi and D. I. Brandao, "Unbalanced Load Compensation by Power-Based Control in the Synchronous Reference Frame," *2019 10th International Conference on Power Electronics and ECCE Asia (ICPE 2019 - ECCE Asia)*, Busan, Korea (South), 2019, pp. 1383-1388.

4. F. P. Marafao, A. M. S. Alonso, **F. Göthner**, E. Tedeschi and D. I. Brandao, "Power- and Current-Based Control of Distributed Inverters in Low-Voltage Microgrids: Considerations in Relation to Classic Droop Control," *2020 Fifteenth International Conference on Ecological Vehicles and Renewable Energies (EVER)*, Monte-Carlo, Monaco, 2020, pp. 1-10.

5. S. J. K. Berg, **F. Göthner**, V. V. Vadlamudi and D. Peftitsis, "The Effect of Non-Ideal Operating Conditions on Reliability of Inverters in Microgrids," *2020 IEEE 11th International Symposium on Power Electronics for Distributed Generation Systems (PEDG)*, Dubrovnik, Croatia, 2020, pp. 573-577.

6. S. J. K. Berg, **F. Göthner**, V. V. Vadlamudi and D. Peftitsis, "Investigation of the Effect of Operating Conditions on Reliability of DC-link Capacitors in Microgrids," *2020 IEEE PES Innovative Smart Grid Technologies Europe (ISGT-Europe)*, The Hague, Netherlands, 2020, pp. 26-30.

7. W. Zhou, R. Torres-Olguin, **F. Göthner**, J. Beerten, M. K. Zadeh, Y. Wang and Z. Chen "A Robust Circuit and Controller Parameters Identification Method of Grid-Connected Voltage Source Converters Using Vector Fitting Algorithm," in IEEE Journal of Emerging and Selected Topics in Power Electronics, doi: 10.1109/JESTPE.2021.3059568.

1.5 Outline of the Thesis

This PhD thesis consists of two main parts. In the first part, the underlying theoretical concepts are presented, and the main scientific contributions are summarized. The second part consists of the three papers that represent the main research contributions of the work. The detailed analysis, results, and discussion, as well as the main contributions, are clearly stated in each paper.

The first part of the thesis is organized as follows. Chapter 2 provides a literature review and an overview of the theoretical foundations that have been used in the work. These aspects have been assumed to be known or have only been briefly addressed in the papers due to the page limitations. The chapter includes an outline of control of DGs, as well as state-space analysis, reduced-order modeling, and impedance-based modeling. Finally, an introduction to the topic of power quality is given. Chapter 3 offers a summary of the main papers, including key results and discussions. How the papers relate to each other are also highlighted. The main findings of the papers are discussed in relation to the objectives of the thesis. Finally, Chapter 4 concludes and presents proposals for future work.

Chapter 2

Theoretical Foundations and State of the Art

This chapter presents an overview of the fundamental concepts that are used in the thesis. This includes an overview of the control of DGs, state-space analysis of microgrids, reduced-order modeling, impedance-based modeling, and power quality in microgrids. The state of the art of these topics is also reviewed.

2.1 Control of Distributed Generators

Several schemes have been proposed in the technical literature for controlling DGs. These schemes can be classified according to the converter operating mode and the level of communication between the DGs. In addition, the control of a DG typically consists of a hierarchical structure. In [15], the possible operating modes of a DG are characterized as grid-following, grid-forming, or grid-supporting. In the grid-following mode, the DG synchronizes to an energized grid and injects power into it. Hence, this operating mode necessitates that the grid voltage is already established. If the microgrid is operating in the grid-connected mode, the main grid establishes this voltage. In island mode, the grid voltage can be established by a DG operating in the grid-forming mode. Then, the DG acts as an ideal voltage source by imposing the voltage magnitude and frequency of the grid. DGs operating in the grid-supporting mode are regulated to keep the grid voltage and frequency around their nominal values. These devices can either be voltage or current controlled. While the current-controlled devices typically need a voltage to synchronize to, the voltage-controlled ones can operate in both grid-connected and islanded mode.

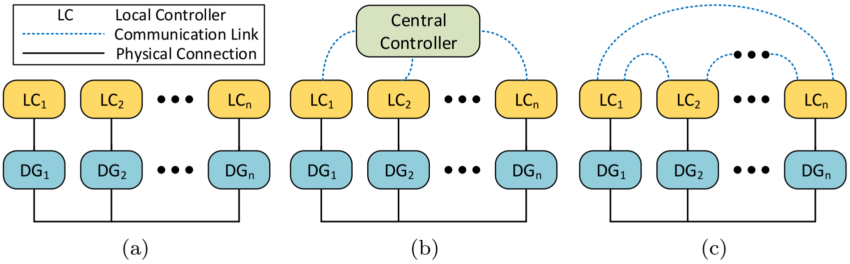

Figure 2.1: (a) Decentralized, (b) centralized, and (c) distributed control schemes for microgrid control.

Several control philosophies have also been adopted for coordinating the control of several DGs in microgrids. These schemes can be broadly categorized as decentralized, centralized, or distributed. An illustration of the schemes is shown in Fig. 2.1. In the decentralized scheme, each DG is solely controlled based on local measurements [16]. Hence, no communication between the DGs is needed in a decentralized approach. Centralized control implies that a centralized controller determines the set-points of each DG, meaning that communication is needed between each DG and the central controller. The distributed control relies on collaboration between several controllers to achieve the desired control goals [17]. Thus, this scheme requires communication between the DGs.

In addition to these schemes, the microgrid control system usually comprises a hierarchical structure [18]. Fig. 2.2 shows an example of a hierarchical control structure consisting of primary, secondary, and tertiary controllers, including typical tasks for each control layer. The bandwidths of the controllers are also shown. The inner loops regulate the current and voltage at the DG terminals. Their reference is provided by the primary control, which is responsible for maintaining the voltage and frequency within acceptable limits. The secondary control is typically related to restoring the voltage and frequency to their nominal values. It also manages transitions between the islanded and grid-connected modes. Finally, the tertiary control manages the power flow between the microgrid and the main grid and optimizes the microgrid performance.

The previously described DG operating modes relate to the primary control in the hierarchical structure. Meanwhile, the control philosophies can be applied at the different hierarchical layers. Centralized or distributed control is more common in the secondary and tertiary layers [17]. On the other hand, decentralized approaches are the most common in the literature for primary control, although some schemes have a communication-based primary control [19, 20]. The reason for the widespread use of decentralized primary control is the enhanced reliability

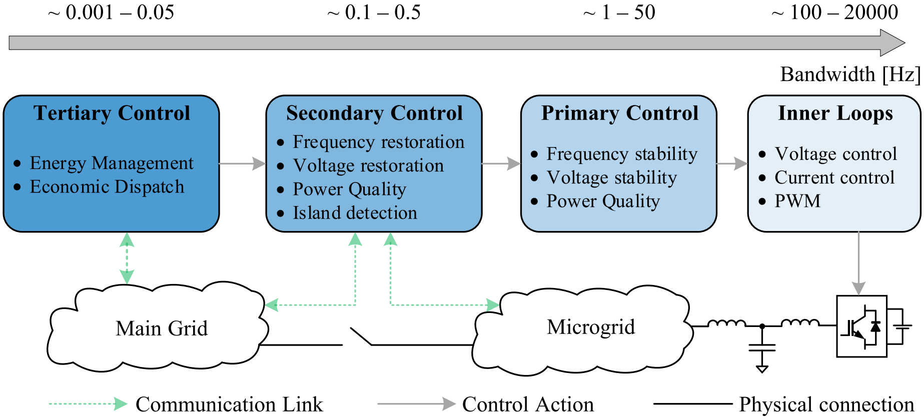

Figure 2.2: Hierarchical control structure of a microgrid, including tertiary, secondary, and primary control loops.

resulting from the lack of communication between DGs. Common decentralized control schemes include droop control and virtual synchronous machines [21, 22].

In this thesis, droop control has been used for the primary control scheme due to its high degree of flexibility and reliability. Therefore, this control scheme will be described in greater detail in the following.

2.1.1 Droop Control

The main objective of the droop control scheme is to support the grid voltage and frequency and to enable parallel operation and adequate load sharing between converters. The control provides a voltage amplitude and frequency set-point for the inner loops of the converter. The original scheme was proposed for uninterruptible power supply (UPS) systems and was made to mimic the behavior of synchronous machines in the traditional power system [21]. In these systems, deviations in frequency are used to alter the injected power. This enables the machines to share the load according to the droop gain of each machine.

The background for droop control is best understood by considering the power flow across a resistive-inductive line, as shown in Fig. 2.3. By expressing the current by the terminal voltages and line impedance, the complex power S is given by:

$$S = Ee^{j\delta}\left(\frac{Ee^{j\delta} - V}{R + jX}\right)^{*}, \tag{2.1}$$

where E and V are voltage magnitudes of the system nodes, δ is the angle between

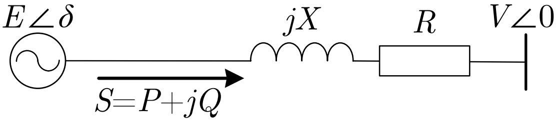

Figure 2.3: Power flow across a resistive-inductive line.

these, while R and X are the line resistance and reactance. This expression can be developed further to obtain the active and reactive powers:

$$P = \frac{RE^2 - REV\cos\delta + XEV\sin\delta}{R^2 + X^2}, \tag{2.2a}$$

$$Q = \frac{XE^2 - XEV\cos\delta - jREV\sin\delta}{R^2 + X^2}. \tag{2.2b}$$

It is evident from (2.2) that the active and reactive powers are coupled with both the voltage magnitude and angle in the general case. However, some of these quantities can be decoupled depending on the R/X ratio when considering the small signal dynamics. In particular, for systems with a low R/X ratio, active power is predominantly connected with the angle, while reactive power is mainly connected with the voltage. This is typical for transmission systems [23], and it was also assumed for the first works using droop control for UPS and microgrid applications [21]. Since the angle is the integral of the frequency, there is also a strong connection between active power and frequency. Therefore, the following droop relations were proposed [21]:

$$\omega = \omega^* - m_p(P - P^*) \tag{2.3a}$$

$$E = E^* - n_q(Q - Q^*) \tag{2.3b}$$

where ω and E are the angular frequency and voltage of the DG, * denotes reference value, while m_p and n_q are the active and reactive power droop gains. The active and reactive powers P and Q are low-pass filtered according to:

$$P = \frac{1}{1+\tau s}\tilde{p} \tag{2.4a}$$

$$Q = \frac{1}{1+\tau s}\tilde{p} \tag{2.4b}$$

where τ is the time constant of the low-pass filter (LPF), while $\tilde{p}$ and $\tilde{q}$ are the instantaneous active and reactive powers. The angle needed for the Park transformations (θ) is obtained by integrating the angular frequency:

$$\theta = \int \omega dt. \tag{2.5}$$

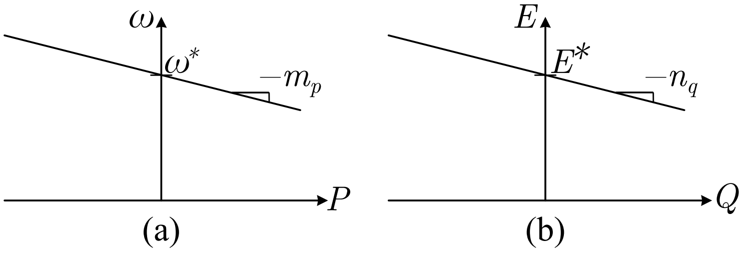

Figure 2.4: (a) Conventional $P\omega$ and (b) QV droop control.

The control law in (2.3) is denoted as conventional droop control, and it is illustrated in Fig. 2.4. Whenever the power produced by the DG exceeds its reference, the DG frequency is less than the nominal value. Likewise, whenever the reactive power exceeds its reference, the DG voltage magnitude is less than its nominal value. A particularly appealing feature of the conventional droop control is that the active power can be shared between DGs in proportion to their rating by proper selection of m_p. This is possible because the frequency is the same for all DGs in steady state. Meanwhile, the reactive power is not inherently shared in the general case, as voltage is a local quantity. Achieving reactive power sharing through supplementary control schemes has consequently attracted significant attention in the literature [24, 25].

Although the initial works using droop control assumed predominantly inductive lines, the feeders in low-voltage systems are typically resistive. This means that the connections between the quantities in (2.2) are different and that another droop scheme could be more effective. In particular, in cases where the R/X ratio is high, (2.2) simplifies to give a strong connection between active power and voltage, and reactive power and frequency. In this case, the opposite droop control is applicable, in which the active power is drooped against voltage and reactive power is drooped against frequency [26]. In cases where the R/X ratio is around unity, both active and reactive power are coupled with frequency and voltage. In this case, a mixed droop approach has been used, in which both the active and reactive powers are drooped against the frequency and voltage [27, 28].

Several proposals have also been made for improving the stability and transient performance of different droop schemes. One popular approach is to use derivative action in the droop controllers, effectively making it a PD controller [26, 29, 30]. This approach is similar to the implementation of virtual impedances [31]. Virtual impedances will be described in Section 2.1.3. Also, integral terms have been added to the droop control to ensure accurate tracking of power references when operating in grid-connected mode [32]. However, this can cause instability in island mode and is therefore often avoided.

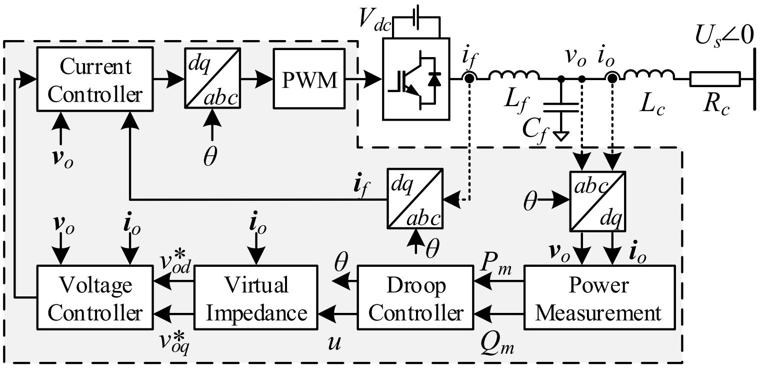

Figure 2.5: Overview of the control scheme for a droop-controlled converter with cascaded voltage and current controllers.

2.1.2 Inner Controllers

While some control designs directly use the droop controller voltage reference to control the converter voltage [33], inner controllers are often employed to form a closed-loop voltage control. The main goal of the internal controllers is then to track the voltage reference provided by the droop controller [15]. In addition, the inner controllers provide an effective means for implementing protection features, such as protecting the converter from over-currents [34]. The internal controllers are commonly designed with significantly larger bandwidths than the droop controller to achieve proper time-scale separation between them. Fig. 2.5 shows an overview of a common implementation of cascaded inner loop controllers [35]. Here, the control is performed using PI controllers in the dq reference frame, but the control can be similarly performed using proportional-resonance (PR) controllers in the $\alpha\beta$ or abc reference frames [36, 37]. The outer voltage controller regulates the voltage over the capacitor C_f, while the inner current controller regulates the current through the inductor L_f. These controllers will be described in the following.

The equations describing the dynamics of the capacitor voltage ($v_{o,dq}$) in the dq reference frame is given by:

$$C_f \frac{dv_{o,d}}{dt} = i_{f,d} - i_{o,d} + \omega C_f v_{o,q}, \tag{2.6a}$$

$$C_f \frac{dv_{o,q}}{dt} = i_{f,q} - i_{o,q} - \omega C_f v_{o,d}, \tag{2.6b}$$

where $i_{f,dq}$ and $i_{o,dq}$ are the converter and grid side currents, respectively, and C_f is filter capacitance. The voltage controller for this plant typically includes decoupling terms and feedforward of the output current. With a PI controller to track the desired voltage reference, the complete voltage controller is given by:

$$i^*_{f,d} = K_{pv}(v^*_{o,d} - v_{o,d}) + K_{iv}\int (v^*_{o,d} - v_{o,d})dt - \omega C_f v_{o,q} + F i_{o,d}, \tag{2.7a}$$

$$i^*_{f,q} = K_{pv}(v^*_{o,q} - v_{o,q}) + K_{iv}\int (v^*_{o,q} - v_{o,q})dt + \omega C_f v_{o,d} + F i_{o,q}, \tag{2.7b}$$

where K_{pv} and K_{iv} are the proportional and integral gains of the voltage controller, F is current feedforward gain, and $i^*_{f,dq}$ is the reference to the inner current controller. The dynamics of the inner filter current ($i_{f,dq}$) is given by:

$$L_f\frac{di_{f,d}}{dt} = v_{i,d} - v_{o,d} - R_f i_{f,d} + \omega L_f i_{f,q}, \tag{2.8a}$$

$$L_f\frac{di_{f,q}}{dt} = v_{i,q} - v_{o,q} - R_f i_{f,q} - \omega L_f i_{f,d}, \tag{2.8b}$$

where $v_{i,dq}$ is the voltage at the converter terminals and L_f is the converter-side filter inductance. Similarly to the voltage controller, the current controller contains decoupling and feedforward terms in addition to a PI controller. The complete current controller is then given by:

$$v^*_{i,d} = K_{pi}(i^*_{f,d} - i_{f,d}) + K_{ii}\int (i^*_{f,d} - i_{f,d})dt - \omega L_f i_{f,q} + F_i v_{o,d}, \tag{2.9a}$$

$$v^*_{i,q} = K_{pi}(i^*_{f,q} - i_{f,q}) + K_{ii}\int (i^*_{f,q} - i_{f,q})dt + \omega L_f i_{f,d} + F_i v_{o,q}. \tag{2.9b}$$

where K_{pi} and K_{ii} are the proportional and integral gains of the PI controller, F_i is a feedforward gain, and $v^*_{i,dq}$ is the reference voltage passed to the PWM.

In microgrids with significantly unbalanced or harmonically distorting loads, resonance controllers are also commonly employed to improve the tracking or mitigation capabilities at certain frequencies. A resonant controller is almost exclusively effective at its resonance frequency, and it is therefore often used in parallel with other controllers. In the Laplace domain, the resonant controller is written on the following form [38]:

$$G_R(s) = \frac{2K_i\omega_c s}{s^2 + 2\omega_c s + \omega_0^2} \tag{2.10}$$

where K_i is a gain, ω_c is the cutoff frequency and ω_0 denotes the resonance frequency. At the resonance frequency, the gain of the controller is determined by K_i, while ω_c is a parameter that can modify the bandwidth of the controller. Since this type of controller is only effective at its resonance frequency, it is common to use several controllers in parallel to address several harmonic frequencies simultaneously. This will substantially increase the controller gain at these frequencies.

2.1.3 Virtual Impedance-Based Control

The virtual impedance concept was first introduced for shaping the output impedance of a converter [39]. This can improve the droop control performance by enforcing a certain R/X ratio. Since then, the concept has been used in several applications, such as active stabilization, harmonic or unbalance compensation, and grid fault ride-through. An overview of numerous virtual impedances applications is given in [14]. The virtual impedance applications of particular interest for this work include improvement of the stability margins of droop-controlled microgrids [40, 41] and improvement of the harmonic power sharing [24, 42–44].

A common implementation of virtual impedances in droop-controlled DGs is to subtract a voltage drop from the voltage reference provided by the droop controller. This is an example of an outer virtual impedance [14]. The voltage drop is obtained by multiplying the DG output current (i_o) with the virtual impedance (Z_v). To discuss some aspects of the implementation of the virtual impedance, consider the voltage drop over an impedance in the dq reference frame:

$$\Delta v_d = Ri_d - \omega L i_q + L\frac{di_d}{dt}, \tag{2.11a}$$

$$\Delta v_q = Ri_q + \omega L i_d + L\frac{di_q}{dt}, \tag{2.11b}$$

where R and L respectively denote the line resistance and inductance, Δv_{dq} is the voltage drop over the impedance, and i_{dq} is the current through the impedance. When implementing virtual impedances, the transient term in (2.11) is typically not used directly in order to avoid amplification of noise [14]. A common strategy is to omit the transient term completely, which replicates the effect of an impedance in steady state. This implementation is denoted as the quasi-stationary approximation. The resulting voltage reference is then:

$$v_{o,d}^* = E - R_v i_{o,d} + \omega L_v i_{o,q}, \tag{2.12a}$$

$$v_{o,q}^* = -\omega L i_{o,d} - R_v i_{o,q}. \tag{2.12b}$$

Another possibility is to include an LPF of the transient term. This is denoted as transient virtual impedance and is given in the Laplace domain by:

$$v_{o,d}^* = E - R_v i_{o,d} + \omega L_v i_{o,q} - \frac{sL_v}{1+\tau_v s} i_{o,d}, \tag{2.13a}$$

$$v_{o,q}^* = -\omega L i_{o,d} - R_v i_{o,q} - \frac{sL_v}{1+\tau_v s} i_{o,q}, \tag{2.13b}$$

where τ_v is the time constant of the LPF. Differences between these two virtual impedance implementations are one of the contributions that will be highlighted in Section 3.2.

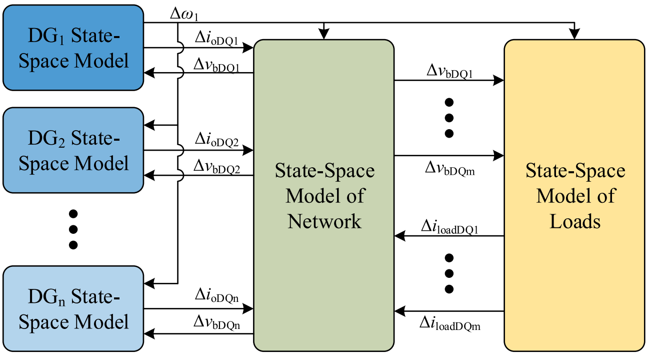

Figure 2.6: Overview of modeling approach for representing a microgrid consisting of DGs, loads, and a network.

2.2 State-Space Analysis

To study the dynamics and small-signal stability of a single DG or an entire microgrid, state-space analysis has been employed. The method has also been widely used in power system studies for decades [23]. This section outlines a methodology for obtaining a small-signal model of a microgrid consisting of droop-controlled DGs, passive loads, and an interconnecting network. The methodology is based on the work of Pogaku *et al.* [35], which has served as a benchmark for studying small-signal stability in microgrids.

An overview of the modeling approach is shown in Fig. 2.6. First, the microgrid is split into sub-models of DGs, network, and loads. Then, the linearized state-space model of each of the sub-models is obtained. These models are on the standard state-space form:

$$\begin{aligned} \Delta\dot{x} &= A\Delta x + B\Delta u \\ \Delta y &= C\Delta x + D\Delta u \end{aligned} \tag{2.14}$$

where x is the state vector, u and y are the input and output vectors, while A, B, C, and D are matrices. The input to one sub-module is the output from another, as illustrated by the arrows in Fig. 2.6. The state-space model of the entire microgrid is finally obtained by aggregating the sub-models.

Each of the DG sub-models is modeled in its own dq reference frame. The lines and loads are modeled in a common reference frame, which is the reference frame of one of the DGs. The common reference frame is denoted as DQ. The complete microgrid model is constructed by translating all DG models to the common reference frame according to the following transformation:

$$\begin{bmatrix} x_D \\ x_Q \end{bmatrix} = \begin{bmatrix} \cos\delta_i & -\sin\delta_i \\ \sin\delta_i & \cos\delta_i \end{bmatrix} \begin{bmatrix} x_d \\ x_q \end{bmatrix}, \tag{2.15}$$

where δ_i denotes the angle between the reference frame of the ith DG and the common reference frame.

2.2.1 DG Model

In the following, the DG models with and without transient virtual impedances will be outlined. The models are obtained by linearizing and combining the controller equations and the equations describing the dynamics of the LCL-filter. The dynamics of the outer filter inductor L_c is given by:

$$L_o \frac{di_{o,d}}{dt} = v_{o,d} - v_{s,d} - R_c i_{o,d} + \omega L_c i_{o,q}, \tag{2.16a}$$

$$L_o \frac{di_{o,q}}{dt} = v_{o,q} - v_{s,q} - R_c i_{o,q} - \omega L_c i_{o,d}, \tag{2.16b}$$

where $v_{s,dq}$ is the grid-side voltage of the filter inductor L_c. In addition, the angle between the DG and the common reference frame is needed to relate the two. This angle is obtained as:

$$\delta = \int (\omega - \omega_{com}) dt \tag{2.17}$$

The small-signal model of the DG is now obtained by linearizing and combining (2.3), (2.4), (2.6)-(2.9), (2.16), and (2.17). In addition, (2.12) or (2.13) should be linearized and included, respectively, for quasi-stationary and transient virtual impedance implementations.

2.2.2 Complete Microgrid Model

The lines and loads are modeled directly in the common reference frame. These are modeled as resistive-inductive branches. The complete MG model is finally obtained by combining the models of the DGs, loads, and the network. For a detailed description, see [35].

2.3 Reduced Order Modeling

While detailed analytical state-space models are useful for obtaining an accurate representation of the microgrid dynamics, several works have advocated the need for reduced-order models [10]. These models try to capture the most relevant dynamics by neglecting or approximating a part of the dynamics, thereby achieving a lower order. Reduced-order models can not only reduce the computational speeds of numerical simulations but also aid in the analytical understanding of the dynamics. As opposed to detailed models, reduced-order models do not require knowledge of all parameters, thereby reducing the possibility of incorrect predictions due to modeling errors. On the other hand, it is imperative that the reduced-order models accurately represent the most important dynamics to be useful. This illustrates an important trade-off between the model complexity and accuracy.

The first reduced-order models for studying the low-frequency dynamics in microgrids approached the modeling similarly as when studying small-signal stability in transmission systems [45, 46]. In particular, the network dynamics and inner controllers were neglected. While these assumptions have been validated for small-signal modeling in the transmission system, it has later been shown that they play an important role in microgrid dynamics [35]. The reason why modeling network dynamics is necessary in microgrids, while it can be omitted in transmission system modeling, is related to the much smaller p.u. impedances between DGs in the former [10]. As a result, several recent reduced-order models have included network dynamics, thereby significantly improving the model accuracy [10, 47–51].

Recent works have also found that the internal controllers in droop-controlled DGs can significantly affect the microgrid low-frequency dynamics, despite their significantly larger bandwidth compared to the droop controller [12, 52]. The coupling between the fast and slow dynamics is partly occurring because of insufficient time-scale separation [12]. Naturally, this depends on the tuning of the droop and inner controllers. However, the type of inner controllers also affects the degree to which the internal controllers affect the low-frequency dynamics. This was clearly shown in [53], in which the small-signal stability margins of the conventional PI-based inner controllers were found to be significantly smaller than an implementation using an internal model-based controller.

In the following, selected reduced-order models of a droop-controlled DG are presented. A method for approximating the network dynamics is also outlined. The importance of accounting for the internal loops is discussed further in Section 3.2.

2.3.1 Reduced-Order DG Models

In [10], a 5th-order DG model denoted as an electromagnetic model was proposed. It contained the dynamics of the droop controller and the network but neglected the effect of fast internal dynamics. Three states (angle, frequency, and voltage) model the internal droop dynamics, while another two states (d and q current phasor components) model the network dynamics. Contrary to the model in [10], real values will be used instead of a per-unit representation. The model is given by:

$$\begin{aligned}
\frac{d\delta}{dt} &= \omega - \omega_0, && (2.18a)\\
\tau\frac{d\omega}{dt} &= \omega^* - \omega - m_p P_m, && (2.18b)\\
\tau\frac{dU}{dt} &= U^* - U - n_q Q_m, && (2.18c)\\
L\frac{dI_d}{dt} &= U\cos\delta - U_s - RI_d + \omega_0 L I_q, && (2.18d)\\
L\frac{dI_q}{dt} &= U\sin\delta - \omega_0 L I_d - RI_q. && (2.18e)
\end{aligned}$$

where $U\angle\delta$ is the effective output voltage of the DG, U_s is the grid voltage, τ is the low-pass filter time constant, P_m and Q_m are the measured active and reactive powers, while the line is a resistive-inductive branch with components R and L. An uppercase variable refers to the dynamic phasor of the signal (e.g. I_d is the dynamic phasor of i_{od}) and ω_0 is the angular frequency of the grid.

This model can be further reduced by neglecting the network dynamics completely, which corresponds to setting the left-hand sides of (2.18)(d)-(e) to zero. Then, the current phasor can be used to calculate the active and reactive powers, which are inserted in (2.18) (b) and (c) to obtain a third-order model. The resulting model is often termed the conventional 3rd-order model [10]. However, a significantly more accurate model is obtained by approximating the effect the network dynamics has on the low-frequency modes, as shown in the following.

2.3.2 Approximating Network Dynamics

A method for approximating the network dynamics was presented in [10]. Under certain assumptions, this method can greatly improve the accuracy of the reduced-order model while maintaining a low computational requirement. The method will be briefly explained in the following.

The network dynamics are governed by 2.18(d)-(e). These equations can be transferred to the Laplace domain and represented by the following current phasor (where $X = \omega_0 L$):

$$I = \frac{Ue^{j\delta} - U_s}{R + jX + sL} = \frac{Ue^{j\delta} - U_s}{R + jX}\frac{1}{1 + \frac{sL}{R + jX}}. \tag{2.19}$$

As noted previously, the first reduced-order models neglected the dynamic term sL in (2.19) and used the resulting quasi-stationary approximation of the current to calculate the active and reactive powers of the DG. This approximation is also called zero's order approximation [10]. A more accurate representation can be obtained by approximating (2.19) by using its first-order Macluarin series:

$$I \approx \frac{Ue^{j\delta} - U_s}{R + jX}\left(1 - \frac{sL}{R + jX}\right). \tag{2.20}$$

This approximation is valid for frequencies such that:

$$\left|\frac{j\omega L}{(R + jX)}\right| \ll 1. \tag{2.21}$$

This criterion can be assumed to hold when studying the low-frequency dynamics [10]. However, it should be noted that the accuracy of the approximation is relevant for the accuracy of the final model. This is further discussed in Section 3.2.

To obtain the final reduced-order model, the active and reactive powers P_m and Q_m should be calculated. These can be obtained by calculating the complex power $S_m = (3/2)Ue^{j\delta}I^*$. After inserting (2.20) and returning to the time-domain, the complex power is given by:

$$S_m = \frac{3}{2}\left(\frac{U^2 - U_s U e^{j\delta}}{R - jX} - L\frac{U\dot{U} - j\dot{\delta}U^2}{(R - jX)^2}\right), \tag{2.22}$$

where the dot refers to the time derivative. The final model is then obtained by linearizing and inserting this equation in (2.18) (b)-(c). For a detailed derivation, see [10].

2.4 Impedance-Based Small-Signal Modeling

Small-signal analysis has traditionally been performed by using state-space analysis in power system applications. However, impedance-based stability analysis is a small-signal method that has gained increased interest in recent years, particularly for applications dominated by power electronics. The method has been extensively used for dc systems, and it was first proposed in [54]. The method was later extended for three-phase ac systems in [55]. The first step in the modeling is to divide the system into source and load subsystems. Then, after finding the small-signal impedances of each subsystem, the stability of the interconnected system can be investigated by using the generalized Nyquist criterion.

The impedances of the subsystems can either be found analytically or by measurements. If they are found analytically, detailed knowledge of the system parameters and configuration is needed. Notable examples of obtaining small-signal impedances analytically are given in [56, 57]. If the impedances are found by measurements, detailed information is not needed as the impedance can be estimated from the terminals of the subsystem. Hence, one of the main advantages of impedance-based stability analysis is that it can be performed without detailed information of the system. This is in clear contrast to state-space analysis, in which detailed information of all components is needed. In addition, by measuring the small-signal impedances online, it is possible to design controllers that adapt to varying grid conditions [58]. On the other hand, impedance-based stability analysis can sometimes suffer from limited observability [59]. Moreover, as the system is compressed into two equivalent subsystems, it may be challenging to find the underlying reasons for any instability in case the subsystems are extensive [12].

In the following, modeling of small-signal impedances will be explained. Then, stability analysis using the impedance-based methods will be outlined. Finally, a related small-signal method named apparent impedance analysis will be described. This method will later be used in Section 3.1.

2.4.1 Modeling Small-Signal Impedances in Three-Phase Systems

To obtain a small-signal impedance, it is necessary to be at an equilibrium point. Then, the small-signal impedance is given by the transfer function from current to voltage. Since voltages and currents are oscillating with the fundamental frequency in three-phase systems, the variables need to be transformed into another domain [11]. One of the most used domains for this purpose is the sequence domain [60], which models the system by using its positive and negative sequence components. By assuming negligible coupling between these, the resulting model is given by two independent single-input single-output (SISO) models. Although it is simpler to analyze the decoupled system, this model has been shown to be inaccurate in some cases [61].

Another commonly used domain for impedance analysis is the *dq* domain [55]. The transformation between the *abc* and *dq* reference frames is accomplished by Park's transformation. As opposed to the sequence domain approach, there is a more pronounced coupling between the *d* and *q* axes. For this reason, impedances in the *dq* domain must be represented by 2x2 matrices, which makes the impedance analysis more involved than in the sequence domain. However, it has been shown that the *dq* domain approach has superior accuracy over the sequence domain in some cases [61]. Therefore, the *dq* domain will be utilized in the following. It can be noted, however, that the same accuracy can be obtained if using the modified sequence domain proposed in [61], but this requires including the coupling effect between the positive and negative sequences in the general case.

The following will define the dq small-signal impedance based on [11], with some differences in notation. To define the small-signal impedance, consider a balanced three-phase system with fundamental frequency ω_1 without any switching dynamics. A variable x_{abc} can then be transformed to the dq domain by using Park's transformation:

$$\begin{bmatrix} x_d \\ x_q \end{bmatrix} = \sqrt{\frac{2}{3}} \begin{bmatrix} \sin(\omega_1 t + \phi_a) & \sin(\omega_1 t + \phi_a - \frac{2\pi}{3}) & \sin(\omega_1 t + \phi_a - \frac{4\pi}{3}) \\ \cos(\omega_1 t + \phi_a) & \cos(\omega_1 t + \phi_a - \frac{2\pi}{3}) & \cos(\omega_1 t + \phi_a - \frac{4\pi}{3}) \end{bmatrix} \begin{bmatrix} x_a \\ x_b \\ x_c \end{bmatrix} \tag{2.23}$$

where ϕ_a is an angle that is normally set to align the d-axis with the peak of the phase a voltage. In steady state, the dq variables will be constant under the stated assumptions. Now, assume that a small perturbation with amplitude $\hat{v}_{dq}$ and frequency ω_p is superimposed on the voltage such that:

$$\begin{bmatrix} v_d(t) \\ v_q(t) \end{bmatrix} = \begin{bmatrix} V_{d0} \\ V_{q0} \end{bmatrix} + \begin{bmatrix} \hat{v}_d \sin(\omega_p t) \\ \hat{v}_q \sin(\omega_p t) \end{bmatrix} \tag{2.24}$$

where subscript 0 denotes the steady-state operating point. The perturbation $\hat{v}_{dq}$ should be much smaller than the steady-state voltage to be eligible for small-signal analysis. The resulting dq currents will then consist of steady-state components, in addition to sinusoidal components of frequency ω_p with amplitudes $\hat{i}_{dq}$ and phase displacements ϕ_{dq}:

$$\begin{bmatrix} i_d(t) \\ i_q(t) \end{bmatrix} = \begin{bmatrix} I_{d0} \\ I_{q0} \end{bmatrix} + \begin{bmatrix} \hat{i}_d \sin(\omega_p t + \phi_d) \\ \hat{i}_q \sin(\omega_p t + \phi_q) \end{bmatrix} \tag{2.25}$$

Upon neglecting the steady-state variables due to the small-signal assumption, the frequency domain voltages and currents can be written as:

$$V_d(j\omega_p) = \hat{v}_d, \quad V_q(j\omega_p) = \hat{v}_q, \quad I_d(j\omega_p) = \hat{i}_d e^{j\phi_d}, \quad I_q(j\omega_p) = \hat{i}_q e^{j\phi_d} \tag{2.26}$$

The dq domain small-signal impedance $\boldsymbol{Z}_{dq}$ is then defined by the 2x2 matrix that relates the voltage and current:

$$\begin{bmatrix} V_d(j\omega_p) \\ V_q(j\omega_p) \end{bmatrix} = \begin{bmatrix} Z_{dd}(j\omega_p) & Z_{dq}(j\omega_p) \\ Z_{qd}(j\omega_p) & Z_{qq}(j\omega_p) \end{bmatrix} \begin{bmatrix} I_d(j\omega_p) \\ I_q(j\omega_p) \end{bmatrix} \tag{2.27}$$

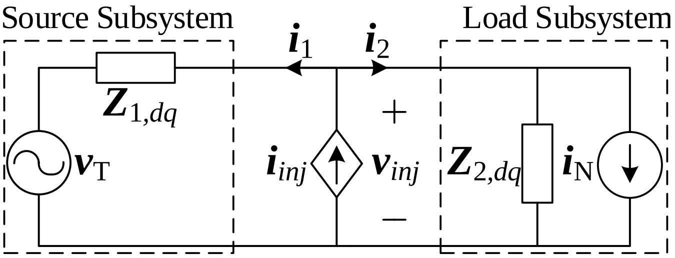

Figure 2.7: System partitioning for impedance-based stability analysis. © 2021 IEEE.

where Z_{dd}, Z_{dq}, Z_{qd}, and Z_{qq} are the elements of the dq impedance matrix. It is also common to define the small-signal impedance in the Laplace domain as given by:

$$\begin{bmatrix} V_d(s) \\ V_q(s) \end{bmatrix} = \begin{bmatrix} Z_{dd}(s) & Z_{dq}(s) \\ Z_{qd}(s) & Z_{qq}(s) \end{bmatrix} \begin{bmatrix} I_d(s) \\ I_q(s) \end{bmatrix} \tag{2.28}$$

Measurement-based impedance estimation has been an important topic of research due to the possible applications for online stability analysis and adaptive control. This consists of perturbing the system at a range of frequencies. Both shunt current injection and series voltage injection have been used for acquiring the necessary perturbation to measure the impedance [62]. Two independent perturbations are needed to obtain the full 2x2 impedance matrix, and this is commonly accomplished by injecting into the disturbances sequentially in the d and q axes [63]. The most straightforward method of acquiring the impedance is to perturb one frequency at a time, which is known as single-tone frequency sweep. While this is an accurate method for obtaining the impedance, it might be time-consuming when it is desired to measure the impedance at many frequencies. To address this issue, the multi-tone frequency sweep perturbs the system at several frequencies simultaneously. A detailed overview of implementing these frequency sweeps is given in [11]. Impedances can also be obtained using broadband excitation of converters, including impulse [58] and pseudo-random sequences [64–66].

2.4.2 Impedance-Based Stability Analysis

An illustration of the complete system is shown in Fig. 2.7, where the source and load subsystems are modeled by their Thevenin and Norton equivalents, respectively. Once the subsystem impedances are obtained, the stability of the interconnected system can be studied, given that the following assumptions are satisfied [60]:

1. The source subsystem must be stable when operating in open loop.
2. The load subsystem must be stable when operating connected to an ideal grid with zero impedance.

For SISO systems, the stability of the interconnected system is then guaranteed if the ratio Z_s/Z_L satisfies the Nyquist criterion [67]. When analyzing multiple-input multiple-output (MIMO) systems, such as when performing impedance analysis in the *dq* domain, the generalized Nyquist criterion should be applied to the minor-loop gain $\boldsymbol{Z}_S \boldsymbol{Z}_L^{-1}$ [55].

2.4.3 Apparent Impedance Analysis

A method that is closely related to the traditional impedance-based stability analysis is the apparent impedance analysis. It was first proposed for dc systems in [68] and later extended for three-phase systems in [69]. Contrary to the conventional impedance-based methods, however, only a single impedance is estimated. This impedance represents a closed-loop transfer function in the system, which enables the method to estimate the eigenvalues that are observable from the point of injection. As such, the method provides a link between impedance-based and state-space stability analysis.

The apparent impedance is obtained by perturbing the system at a point in the system. This can be achieved by a shunt current or series voltage injection. The apparent impedance $\boldsymbol{Z}_{a,dq}$ is defined as the equivalent impedance seen from the point of injection:

$$\boldsymbol{V}_{inj} = \boldsymbol{Z}_{a,dq} \boldsymbol{I}_{inj}, \tag{2.29}$$

where $\boldsymbol{V}_{inj}$ and $\boldsymbol{I}_{inj}$ are the perturbed voltage and current in the *dq* frame in the Laplace domain. Thus, the apparent impedance can be viewed as the parallel connection of the subsystem impedances in Fig. 2.7.

The relation between the poles of the apparent impedance and the eigenvalues of a state-space representation can then be established by considering the perturbation current ($\boldsymbol{i}_{inj}$) and the voltage ($\boldsymbol{v}_{inj}$) as the input and output, respectively. The state-space representation of the system can then be written as:

$$sx = Ax + B\boldsymbol{i}_{\text{inj}} \tag{2.30a}$$

$$\boldsymbol{v}_{\text{inj}} = Cx + D\boldsymbol{i}_{\text{inj}} + Es\boldsymbol{i}_{\text{inj}}, \tag{2.30b}$$

where the input and output are $\boldsymbol{i}_{\text{inj}} = [i_{inj,d},\ i_{inj,q}]^T$ and $\boldsymbol{v}_{\text{inj}} = [v_{inj,d},\ v_{inj,q}]^T$, respectively. If the state vector x contains n states, the state matrix A has dimension $n \times n$, the input matrix B has dimension $n \times 2$, and the output matrix C has dimension $2 \times n$. In addition, the matrices D and E have dimensions 2×2. Upon combining (2.30a) and (2.30b), and comparing the result to (2.29), the apparent impedance is obtained as:

$$\boldsymbol{Z}_{a,dq} = C(sI - A)^{-1}B + D + sE. \tag{2.31}$$

Hence, the poles of the apparent impedance correspond to the eigenvalues of the system. More precisely, only the eigenvalues of the system that are observable from the point of injection are identical to the poles of the apparent impedance. Hence, the method may not capture all eigenvalues in a system. This drawback also occurs for the traditional impedance method, where limited observability of certain states can occur based on where the system is partitioned [59].

To find the system eigenvalues, an estimate of the apparent impedance should first be obtained. This can be achieved by perturbing the system at several frequencies with two linearly independent injections [63]. A non-parametric estimate of the apparent impedance is then calculated for each frequency in the frequency sweep as:

$$\boldsymbol{Z}_{a,dq}=\begin{bmatrix} V_{inj1,d} \, V_{inj2,d} \\ V_{inj1,q} \, V_{inj2,q} \end{bmatrix} \begin{bmatrix} I_{inj1,d} \, I_{inj2,d} \\ I_{inj1,q} \, I_{inj2,q}. \end{bmatrix}^{-1}, \tag{2.32}$$

where the subscripts $inj1$ and $inj2$ refer to the first and second injections, respectively. The apparent impedance in (2.32) can then be used as input to system identification methods to extract the system eigenvalues. The following section will describe the vector fitting technique, which has been used to this end.

2.4.4 Vector Fitting

Vector fitting is a mathematical technique that enables fitting frequency responses to rational function approximations, by using poles and residues [70–72]. In doing so, it can estimate the state-space model of a transfer function based on curve fitting [69]. Vector fitting is applicable to SISO systems, while an extension that is applicable to MIMO systems also exists. In this case, the method is denoted as matrix fitting. The method is also available online [73].

An approximation of a transfer function matrix $\boldsymbol{H}(s)$ is given by the following rational function [11, 70]:

$$\boldsymbol{H}(s) \approx \sum_{i=1}^{n} \frac{\boldsymbol{R}_i}{s - \lambda_i} + \boldsymbol{D} + s\boldsymbol{E} \tag{2.33}$$

where $\boldsymbol{R}_i$ is the ith residue matrix corresponding to the poles λ_i, while $\boldsymbol{D}$ and $\boldsymbol{E}$ are matrices. The unknowns in (2.33) are the poles, residue matrices and the matrices $\boldsymbol{D}$ and $\boldsymbol{E}$. Vector fitting solves the problem in two stages, where known poles are used for both stages. In the first stage, a set of starting poles are specified. These are used to solve an augmented least-squares problem, from which an estimate of the poles is obtained. This process is repeated until convergence occurs, which is typically achieved within a few iterations. Then, these poles are used to find the residue matrices and matrices $\boldsymbol{D}$ and $\boldsymbol{E}$ in (2.33). For more details on vector fitting, see [70].

In addition to the frequency response input, the order of the model needs to be specified. However, the actual number of states of a system is generally unknown. By choosing a sufficiently large model order, the system modes can be identified, but this might also give a number of insignificant modes. Therefore, a method for reducing the model order was proposed in [69] to remove insignificant eigenvalues. The method is based on the fact that a state is not contributing to the measured response if its residue divided by its eigenvalue has a small absolute value [70]. The model order can therefore be reduced until the following holds [69]:

$$\|\boldsymbol{R}_i\|_2/|\lambda_i| \geq \epsilon \tag{2.34}$$

where $\|\cdot\|_2$ is the 2-norm of a matrix. The value for ϵ is set to 10^{-4} based on the discussion in [69].

2.5 Power Quality in Microgrids

The previous sections have described important concepts for studying the stability of microgrids. Another topic that has attracted attention in microgrid research is power quality, as a large amount of power electronics-interfaced DGs and loads can lead to significantly deteriorated voltage quality [9]. Moreover, the voltage quality can also be reduced because of unbalance between phases in the distribution grid. Although the term power quality encompasses a variety of effects, the focus in this thesis is placed on power quality issues resulting from harmonics. Since reduced voltage quality can be detrimental for electrical equipment, several standards limit the allowed distortion in the grid [74, 75]. Traditionally, power quality issues have been addressed by using active or passive filters [76]. However, an attractive alternative for microgrids is to address these issues by modifying the control of the DGs. This is possible because of the flexibility provided by the power electronic interface and the fact that the DGs are often not operating at full capacity. Hence, the spare capacity can be used for improving the power quality.

If DGs are used to address power quality issues, one important aspect to consider is the degree to which each DG should contribute to the harmonic compensation. While the simplest approach is to let a single DG compensate the

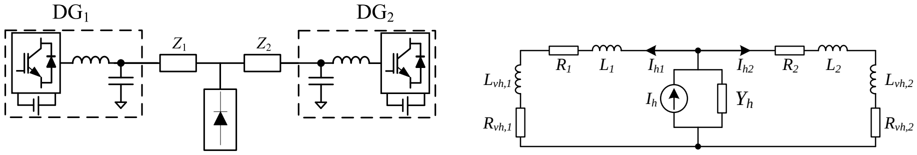

(a) (b)

Figure 2.8: (a) Two parallel DGs with a common nonlinear load and (b) its simplified electrical model at harmonic frequency h. © 2021 IEEE.

harmonics, this might lead to reduced reliability of that particular DG. On the other hand, the harmonic compensation can also be performed by a group of DGs, but this requires more coordination between the devices. In the following, fundamental aspects of a cooperative harmonic compensation are addressed, in addition to a review of proposed control solutions.

2.5.1 Harmonic Current Sharing in Microgrids

Consider first the simple microgrid in Fig. 2.8 (a), in which two DGs are operating in parallel to feed a non-linear load. A simplified equivalent model at harmonic frequency h is given in 2.8 (b). At harmonic frequencies, the load is modeled as a current source (I_h in parallel with the admittance Y_h), while the DGs are modeled as impedances. The impedance of a DG consists of the output impedance and any virtual impedance of the DG [77]. The lines are modeled as a series connection of resistance and inductance (R and L). The term *equivalent impedance* will be used to denote the sum of the line and DG impedances. These impedances are denoted as Z_1 and Z_2 for DG1 and DG2, respectively.

To achieve equal harmonic current sharing, the equivalent impedances of the DGs need to match. This can be shown by considering the harmonic current drawn by the DGs with respect to the harmonic load current:

$$\frac{i_{h1}}{I_h} = \frac{1/Z_1}{1/Z_1 + 1/Z_2 + Y_h}, \tag{2.35a}$$

$$\frac{i_{h2}}{I_h} = \frac{1/Z_2}{1/Z_1 + 1/Z_2 + Y_h}. \tag{2.35b}$$

The harmonic sharing between the DGs can then be expressed by combining (2.35):

$$i_{h1} Z_1 = i_{h2} Z_2. \tag{2.36}$$

Thus, equal harmonic current sharing necessitates equal equivalent impedances. Otherwise, the DG with the smaller equivalent impedance will consume a larger share of the harmonic currents. Equivalent impedances can be achieved by increasing the virtual impedance of the DG with the smaller equivalent impedance. Another possibility is to use large virtual impedances for both DGs, so that differences in the line impedances become negligible. However, this will produce a larger harmonic voltage drop, thereby deteriorating the voltage quality [42]. This, therefore, represents a trade-off between harmonic current sharing and voltage quality.

2.5.2 Proposed Control Solutions

Several solutions have been proposed for addressing harmonic current sharing and improving the voltage quality in MGs [9]. These strategies can be categorized as droop-based, hierarchical-based, and virtual impedance-based approaches. An overview of these approaches is given next.

One of the first droop-based strategies that dealt with cooperative harmonic compensation was proposed in [78]. Here, a harmonic conductance was drooped against harmonic power, where harmonic power was defined as in [79]. The harmonic power was calculated at the DG terminals, thereby enabling a decentralized scheme. However, in cases where the DGs are interfaced with LCL filters and electrical lines are long, this method can give undamped oscillations at the point of common coupling. Another harmonic droop controller was proposed in [80], which addressed the harmonic sharing between DGs and the voltage quality of the PCC. The method is based on measuring the harmonic content at the PCC, based on which each DG update their droops. A drawback of this method is that it requires relatively fast communication systems.

Centralized strategies have also been used to improve the power quality in microgrids. In [81], the voltage quality of a sensitive load bus was regulated by using a hierarchical approach. Based on the harmonic content of the load bus, the secondary controller provides a reference to the primary controller. This scheme can improve the voltage quality, but its performance is uncertain in more general topologies. To address this issue, a tertiary controller that includes an optimization algorithm ensuring acceptable voltage quality of all buses was proposed in [82]. However, this was only performed for unbalanced systems. In [83], a centralized controller for ensuring harmonic current sharing between parallel-connected DGs was proposed. The controller is applicable to both current- and voltage-controlled DGs operating in parallel. As such, it is unclear how well this approach can be extended for more general topologies.

Several virtual impedance schemes have also been devised for improving power quality. As noted in Section 2.5.1, accurate harmonic current sharing can be achieved by setting the virtual impedances sufficiently large. The simplest implementation is to use the same virtual impedance at all frequencies [37]. However, it is also common to have a different virtual impedance for the fundamental and harmonic frequencies, as their requirements might differ. For instance, only inductive harmonic virtual impedance was included in [42], while resistive harmonic and inductive fundamental virtual impedances were used in [29]. Similar approaches can be found in [43,84]. Capacitive virtual impedances have also been explored to compensate for harmonic voltage drops of long lines [85, 86]. While many works have emphasized the importance of sharing the harmonic compensation between DGs, some works have also argued that the compensation effort should not necessarily be split equally [87, 88]. By letting the DG(s) closest to the nonlinear load compensate the most, the distribution losses can be reduced. On the other hand, this will pose larger stress on the DGs that perform the compensation.

A majority of the research on harmonic compensation strategies in microgrids has focused on topologies with parallel-connected DGs and a common load. However, there has recently been an increased interest in strategies encompassing more complex network topologies [89–91]. In [89], an optimization algorithm for reducing the voltage unbalance in a general radial microgrid was proposed. Although improving the voltage quality, the scheme requires voltage references to be sent from the central controller to the DGs continuously. Another optimization algorithm that addressed the voltage quality in a microgrid was proposed in [90]. However, this method did not consider harmonic current sharing between the DGs. In [91], real-time supervisory control for addressing power quality in multi-area microgrids was proposed. In this case, current harmonic sharing is not addressed, as the main goal of the paper was to allocate the least number of DGs or active power filters while ensuring the desired power quality.

In conclusion, several control solutions address power quality in microgrids. However, many of these are only applicable to certain topologies. A proposal that addresses this issue is provided in Section 3.3.

Chapter 3

Contributions

This chapter provides a summary of the main articles. An overview of the contributions of each article is provided, and it is explained how the papers address the research questions in this thesis. The research questions are repeated here:

1. How can the performance of microgrids with droop-controlled DGs be improved, without compromising the benefits of a decentralized approach?
2. How should virtual impedances be designed for improved performance?
3. What DG elements should be represented to obtain a sufficiently accurate model in network stability studies?

Selected analytical results that highlight the contributions are also presented. The detailed developments, analysis, discussion, and experimental work are further explained in the papers. In addition, extended details regarding the laboratory facilities are given in Appendix B. Finally, the chapter is concluded with a discussion of how the papers relate to each other.

3.1 Apparent Impedance-Based Adaptive Controller - Paper I

The stability of droop-controlled microgrids is known to be susceptible to the droop parameter values and system topology. In particular, small distances between the DGs can cause instability for a given droop value. The rapid deployment of DGs can therefore be challenging, as the efficient electrical distance between DGs reduce with increased deployment. To address this issue, a centralized controller for improving the stability of droop-controlled microgrids was proposed in this paper. The controller first estimates the dominant low-frequency modes by using the apparent impedance method. Depending on the location of these modes, the droop gains of the DGs are subsequently modified by using a control law.

As the proposed controller targets improved microgrid stability, this work contributes to answering the first research question. Although being centralized, the proposed controller does not reduce the reliability of the conventional droop control. This is because the proposed controller can be considered a supplement to the conventional droop control, such that the basic primary control still works even if the proposed controller is unavailable, e.g. due to a communication breakdown. It should also be noted that only a low-bandwidth communication channel is required.

The following subsections will outline and discuss the proposed controller, in addition to the accuracy of the mode identification. Simulation results illustrating the proposed controller are also given.

3.1.1 Overview of Proposed Controller

An overview of the proposed method is presented in the flowchart in Fig. 3.1 (a). In the first step, the allowed and damped regions of the complex plane are specified. The regions are shown in Fig. 3.1 (b). The allowed and damped regions are specified by a minimum damping, respectively given by ζ_- and ζ_+. In addition, the regions are limited by the maximum frequency ω_{lim}. The damped region is a subset of the allowed region. The main purpose of the proposed controller is to place the low-frequency modes of the microgrid inside the allowed region.

In the second step, the system modes are identified by using the apparent impedance and matrix fitting methods. A dedicated converter is used to perturb the system to obtain the apparent impedance and the associated system modes. It is then checked if any of these modes are outside the allowed region. If so, the droop gain is reduced for all DGs. Otherwise, it is checked whether all modes are in the damped region. If this is the case, the system is considered to be unnecessarily damped, such that the droop gain is increased. If all modes are in the allowed region, but not all are in the damped region, no change in the control occurs. The last step in the flow chart is to wait before the process is repeated from identifying the system modes.

The increase or reduction in the effective droop gain is achieved by introducing a factor γ in the conventional droop control law:

$$\omega = \omega^* - \gamma m_p P, \quad \gamma \in (0, 1] . \tag{3.1}$$

Here, γ is a parameter calculated by the centralized controller. This parameter is calculated recursively, according to the location of the identified low-frequency

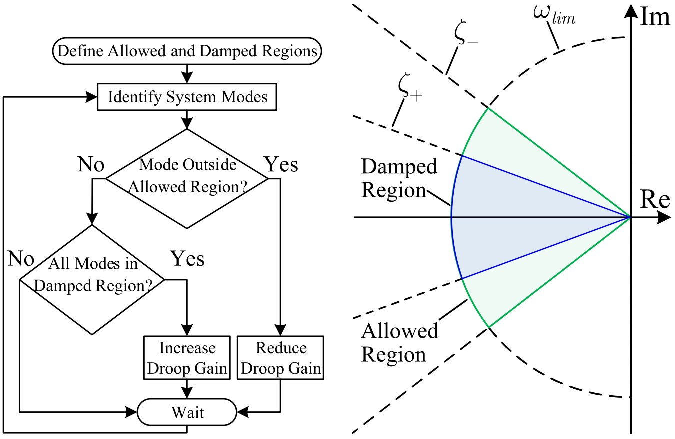

(a) (b)

Figure 3.1: (a) Flowchart of the proposed control and (b) allowed and damped regions for the system eigenvalues. © 2021 IEEE.

modes:

$$\gamma[k] = \begin{cases} \alpha_i \gamma[k-1], \text{ if } \zeta_i \geq \zeta_+ \vee |\lambda_i| \geq \omega_{lim} \ \forall i \\ \gamma[k-1], \text{ if } \zeta_i \geq \zeta_- \vee |\lambda_i| \geq \omega_{lim} \ \forall i \\ \alpha_r \gamma[k-1], \text{ otherwise} \end{cases} \tag{3.2}$$

where α_i and α_r are constants, λ_i and ζ_i denote the ith eigenvalue and its corresponding damping ratio, and $\gamma[1] = 1$. The constants α_i and α_r are, respectively, larger than and less than unity. Thus, γ is reduced by α_r if any mode is located outside the allowed region, and it is increased by α_i if all modes are located in the damped region. Otherwise, γ maintains its previous value.

3.1.2 Discussion of Control Design

The active power droop gain is known to be an important parameter for the stability of droop-controlled microgrids. However, other control parameters also affect the stability, indicating that these could have been used in the adaptive controller. Therefore, a justification for using the active power droop gain is given in the following.

Participation factor analysis of droop-controlled microgrids has shown that the dominant low-frequency modes are associated with the states of the droop controller [35]. This makes sense intuitively, given that DGs typically have a cascaded control structure where the droop controller is the slowest outer loop (see Fig. 2.5). Hence, the parameters of the droop controller are candidates for being used to relocate the low-frequency modes. However, when examining the participation factor analysis in [35] more closely, it is seen that the dominant low-frequency modes are mainly associated with the active power and angle states. This suggests that the low-frequency modes are more sensitive to variations in m_p than in variations of n_q. This is supported by the reduced-order models in [10], where it is shown that m_p is typically the droop gain that is limiting stability for practical droop values. To illustrate this, consider the root-locus diagrams in Fig. 3.2. The diagrams are obtained from a microgrid consisting of four DGs. In Fig. 3.2 (a), m_p is reduced from 1e-4 to 5e-5. This results in a significantly increased damping of the low-frequency modes. In Fig. 3.2 (b), n_q is reduced from 5e-4 to 5e-5. It can be seen that this results in an increase in the damping of the least oscillatory eigenvalues. Meanwhile, the complex pair of eigenvalues with the largest imaginary part first move towards the real axis, before moving away from it as n_q is further reduced. This indicates that reducing n_q can lead to reduced damping at some operating points. It should also be noted that the range in which n_q is varied is much larger than the corresponding range of m_p values. This suggests that the sensitivity of the low-frequency modes are more sensitive to variations of m_p.

Another advantage of modifying the effective active power droop gain is that this does not affect the power sharing in steady state. To show this, consider (3.1) in steady state. Since the frequency is a global quantity, and γ is the same

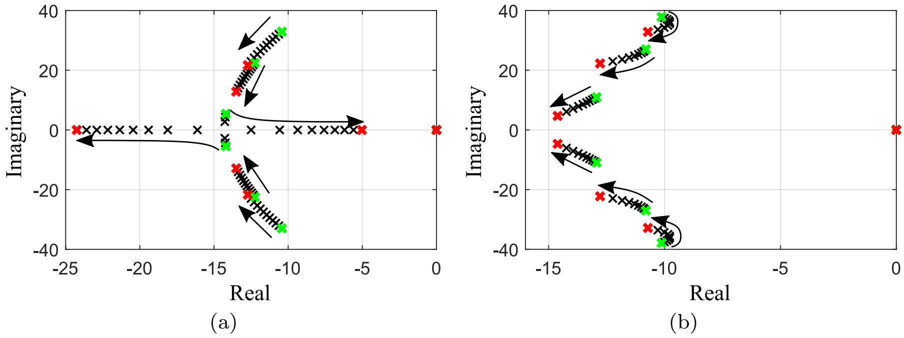

(a) (b)

Figure 3.2: Root locus diagram of the low-frequency modes when reducing (a) m_p and (b) n_q. The green and red crosses indicate the starting and stopping position of a mode, respectively. The arrows show the direction of reducing values.

for all DGs, the power sharing between DGs j and k will be determined by:

$$\frac{P_j}{P_k} = \frac{\gamma m_{p,k}}{\gamma m_{p,j}} = \frac{m_{p,k}}{m_{p,j}} \tag{3.3}$$

Thus, the proposed control does not affect the steady-state active power sharing, even if the droop gains between the DGs differ.

3.1.3 Mode Identification Accuracy

The successful implementation of the proposed controller requires accurate identification of the low-frequency modes. To discuss this, the frequency injections and the matrix fitting technique itself should be considered in closer detail.

As noted in Section 2.4.4, the model order needs to be selected to use the matrix fitting technique. In this case, the maximum order of the identified system is limited to the number of frequency injections. Hence, a minimum number of frequency injections should be used to identify the apparent impedance. On the other hand, it is not desired to have an excessive number of frequency injections, as this leads to increased harmonic distortion in the microgrid. The frequency range in which the injections are performed should also be selected carefully. In particular, the frequency range should be selected in the range where the low-frequency modes reside. This is because the matrix fitting technique is only accurate in the frequency range of the measured response [70].

The model order is also determined so that the criterion in (2.34) holds. Combined with the limited number of frequency injections, this means that not all eigenvalues are likely to be identified in most practical applications. However, the matrix fitting technique will identify the least damped modes, given that they are observable from the point of injection. This is clear by considering how the matrix fitting technique works. The technique minimizes the rms error between the rational function approximation and actual frequency response. Complex conjugate poles give a well-observable resonance peak in the measured response, such that the technique estimates these poles accurately. Otherwise, the rms error would be substantial. Meanwhile, real poles may not be estimated with the same degree of accuracy. This occurs because the contribution from these eigenvalues can be less visible in the frequency response, such that a smooth response can be fitted quite accurately with several choices of real eigenvalues. As the method proposed here mainly focuses on the least damped eigenvalues, this is considered an acceptable performance.

3.1.4 Simulation Results

The proposed controller will be illustrated with a case where a DG is added to a microgrid consisting of three DGs. This represents a relevant scenario for future microgrids, as the availability of renewable energy sources might lead to relatively frequent connection and disconnection of DGs. Fig. 3.3 displays the resulting operating points the system is undergoing. The colors mark different operating points. Estimated eigenvalues are shown with circles, while the analytical eigenvalues are shown by x-marks. The dark blue circles show the initial operating point, in which all eigenvalues are inside the allowed region. It can be seen that there is a good match between the analytical and estimated eigenvalues in this case.

Next, a new DG is connected to the system, and the resulting estimated eigenvalues are shown in light blue. This results in a new pair of complex eigenvalues. It can be seen that the two least damped complex conjugate eigenvalues are accurately estimated, while there is a mismatch in the estimation of the most damped complex conjugate eigenvalues. Also, the least damped complex eigenvalues marked by (1) are now outside the allowed region. Therefore, the centralized controller reduces γ.

The subsequent operating point is shown in dark green. There is again a slight mismatch in the estimation of the most damped pair of eigenvalues. The dominant eigenvalues (2) are still outside the allowed region, thus leading to another reduction of γ. The new operating point is shown in bright green. Now, the least damped complex pair of eigenvalues (3) is inside the allowed region such that the desired stability margin is attained. For this operating point, only two complex pairs of eigenvalues remain, and these are estimated with a good degree of accuracy. The other two eigenvalues became real, and there is a notable mismatch in the estimation of these eigenvalues. This supports the previous

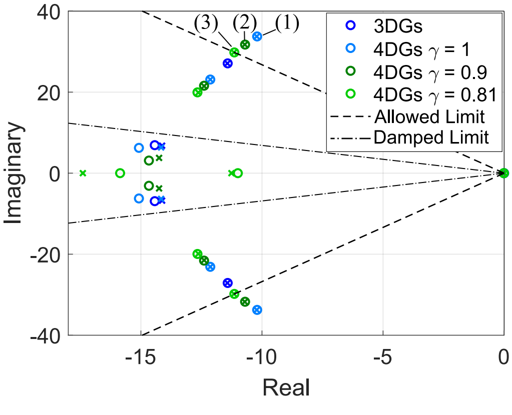

Figure 3.3: Estimated (circles) and analytical (x-marks) eigenvalues as a result of connecting an additional DG and reducing γ. © 2021 IEEE.

discussion indicating that the least damped modes are accurately identified, while there may be a mismatch for more damped and purely real modes.

3.1.5 Main Contribution

The main contribution from the paper can be summarized as follows:

- A method for safeguarding the stability of a microgrid is proposed by adaptively updating the active power droop gain of the DGs. No previous information of the system topology or parameter values is required in doing so. Moreover, the stability is improved without compromising the inherent power sharing, transient performance, and low dependence on communication systems of the droop control.

3.2 Including Realistic Effects in Reduced-Order Converter Modeling - Paper II

Reduced-order modeling is being increasingly applied for microgrids as it can give numerically efficient and accurate models. This will not only improve computational speeds when analyzing larger systems, but it can also aid in the analytical understanding of more complex models. However, what to include in these models to obtain a sufficiently accurate model is not straightforward. Although virtual impedances are commonly used in microgrid applications to achieve adequate damping and transient response, their effects have usually not been included in reduced-order models. In addition, the effect of the internal dynamics has also commonly been neglected. To address these issues, a reduced-order model of a DG that includes virtual impedances and internal dynamics was developed in this paper. The assumptions used in developing the model were examined, and a criterion for deciding the applicability of the reduced-order model was presented. Based on the proposed model, differences between transient and quasi-stationary virtual impedances in terms of low-frequency stability were highlighted.

This work contributes to answering all the research questions in the thesis. In response to the third research question, it is found that an approximation of the internal DG dynamics is important to include to accurately model the DG. The criterion for deciding the model applicability also contributes to answering this question. In addition, it is found that quasi-stationary virtual impedances present improved stability characteristics over their transient counterparts. Thus, this contributes to answering the first and second research questions.

In the following, the modeling of the DG and the criterion for selecting the model order are outlined. In addition, some of the main analytical results are presented.

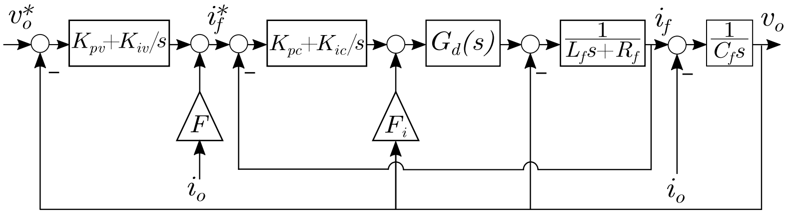

Figure 3.4: Block diagram representing the dq axes dynamics of the output filter and the internal control loops. The d and q axes are assumed decoupled. © 2021 IEEE.

3.2.1 Simplifying Internal Dynamics

Despite the significantly faster inner loops, there exists a coupling between these and the outer droop controller dynamics. The fast dynamics are almost linear, as it is composed of linear controllers and linear circuits. This means that it is possible to approximate the fast dynamics without distorting the slow dynamics [12]. This will be used to simplify the internal loops to evaluate their effect on the slower dynamics. In particular, this will be done by approximating the frequency response of the fast dynamics at low frequencies.

By assuming that the d and q axes are decoupled, the internal dynamics of both axes can be represented by the block diagram in Fig. 3.4. The plant is represented by the filter capacitor (C_f) and inductor (L_f). The inner current controller is represented by its PI controller ($K_{pc} + K_{ic}/s$) and feedforward of the capacitor voltage (through the gain F_i). Similarly, the outer voltage controller is represented by its PI controller ($K_{pv} + K_{iv}/s$) and feedforward of the output current (through the gain F). The PWM is modeled by the block G_d. The capacitor voltage can be expressed as:

$$\begin{bmatrix} v_{od} \\ v_{oq} \end{bmatrix} = T_v(s)\boldsymbol{I} \begin{bmatrix} v_{od}^* \\ v_{oq}^* \end{bmatrix} - Z_o(s)\boldsymbol{I} \begin{bmatrix} i_{od} \\ i_{oq} \end{bmatrix}, \tag{3.4}$$

where T_v is the complementary sensitivity function, Z_o is the inner DG impedance, and $\boldsymbol{I}$ is the identity matrix. As the inner current loop is designed to have a significantly larger bandwidth than the outer voltage controller, it is reasonable to assume that $i_f \approx i_f^*$ at low frequencies. This assumption is confirmed by considering the bode plots in Fig. 3.5. The dashed lines show T_v and Z_o when the internal loops are included, while the solid lines display the same transfer functions when the internal loops are neglected. It can be seen that neglecting the inner current dynamics is an appropriate assumption for frequencies lower than about 1000 rad/s. Hence, this assumption is justified in the low-frequency range.

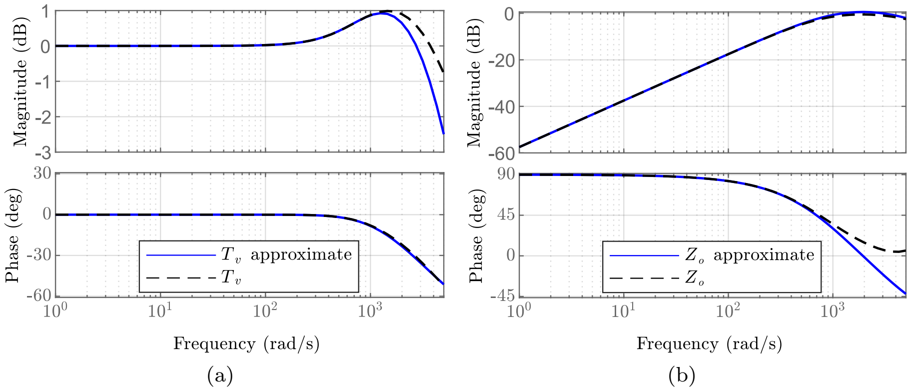

Figure 3.5: Frequency responses of T_v and Z_o. © 2021 IEEE.

With this assumption, the matrices in (3.4) are given by:

$$T_v(s) = \frac{K_{pv}s + K_{iv}}{C_f s^2 + K_{pv}s + K_{iv}}, \tag{3.5a}$$

$$Z_o(s) = (1 - F)\frac{s}{C_f s^2 + K_{pv}s + K_{iv}}. \tag{3.5b}$$

The effect of the fast dynamics on the slow dynamics can then be found by considering these transfer functions. In the low-frequency range, these can be further approximated by:

$$T_v \approx 1 \text{ and } Z_o \approx sL_o, \tag{3.6}$$

where $L_o = (1 - F)K_{iv}^{-1}$. Hence, the effect of the internal dynamics can be modeled as the transient part of an inductor at low frequencies. By approximating the transient term in (2.13) as sL_v at low frequencies, the DG output voltage with a transient virtual impedance can be calculated by combining (2.13), (3.4) and (3.6):

$$\begin{bmatrix} v_{od} \\ v_{oq} \end{bmatrix} = \begin{bmatrix} u \\ 0 \end{bmatrix} - \begin{bmatrix} R_v & -\omega L_v \\ \omega L_v & R_v \end{bmatrix} \begin{bmatrix} i_{od} \\ i_{oq} \end{bmatrix} - s(L_o + L_v)\boldsymbol{I} \begin{bmatrix} i_{od} \\ i_{oq} \end{bmatrix}. \tag{3.7}$$

It should be noted that the DG output voltage with only quasi-stationary virtual impedance is obtained by setting $L_v = 0$ for the last term in 3.7. It can be seen from (3.7) that the internal dynamics and virtual impedances can be represented by an ideal voltage source in series with a form of impedance.

By including this in the electromagnetic model in (2.18), the following 5th-order model is obtained:

$$\frac{d\delta}{dt} = \omega - \omega_0, \tag{3.8a}$$

$$\tau\frac{d\omega}{dt} = \omega^* - \omega - m_p P_m, \tag{3.8b}$$

$$\tau\frac{dU}{dt} = U^* - U - n_q Q_m, \tag{3.8c}$$

$$L_t\frac{dI_d}{dt} = U\cos\delta - U_s - R_{eq}I_d + X_{eq}I_q, \tag{3.8d}$$

$$L_t\frac{dI_q}{dt} = U\sin\delta - X_{eq}I_d - R_{eq}I_q, \tag{3.8e}$$

where the effect of real and virtual impedances, as well as the effect of internal loops, is included in the values of $R_{eq} = R_c + R_v$, $X_{eq} = \omega_0(L_c + L_v)$ and $L_t = L_c + L_o + L_v$. Note that $L_t = L_c + L_o$ for a quasi-stationary virtual impedance implementation.

The model in 3.8 has the exact same form as the electromagnetic model in [10]. Hence, the network dynamics can be approximated as shown in Section 2.3.2. The resulting small-signal 3rd-order model can then be written as:

$$\frac{\tau}{m_p}\Delta\ddot{\delta} + \left(\frac{1}{m_p} - B'\right)\Delta\dot{\delta} + B\Delta\delta + \frac{G}{U_0}\Delta\dot{U} - \frac{G'}{U_0}\Delta U = 0 \tag{3.9a}$$

$$\left(\frac{\tau}{n_q} - \frac{B'}{U_0}\right)\Delta\dot{U} + \left(\frac{1}{n_q} + \frac{B'}{U_0}\right)\Delta U - G\Delta\dot{\delta} + G'\Delta\delta = 0 \tag{3.9b}$$

where

$$B = \frac{3X_{eq}U_0^2}{2(R_{eq}^2 + X_{eq}^2)}, \quad G = \frac{3R_{eq}U_0^2}{2(R^2 + X_{eq}^2)}, \tag{3.10a}$$

$$B' = \frac{3L_tR_{eq}X_{eq}U_0^2}{(R_{eq}^2 + X_{eq}^2)^2}, \; G' = \frac{3L_t(R_{eq}^2 - X_{eq}^2)U_0^2}{2(R_{eq}^2 + X_{eq}^2)^2}. \tag{3.10b}$$

A simplistic estimate of the small-signal stability boundary in (3.9) is to require positive coefficients in front of $\Delta\dot{\delta}$ and $\Delta\dot{U}$ [10]. This can equivalently be written in terms of the droop coefficients as:

$$m_p < \frac{(R_{eq}^2 + X_{eq}^2)^2}{3L_tR_{eq}X_{eq}U_0^2}, \quad n_q < \frac{\tau(R_{eq}^2 + X_{eq}^2)^2}{3L_tR_{eq}X_{eq}U_0}. \tag{3.11}$$

Since L_t is larger for transient virtual impedances than for quasi-stationary virtual impedances, the estimates of the stability regions are smaller for the tran-

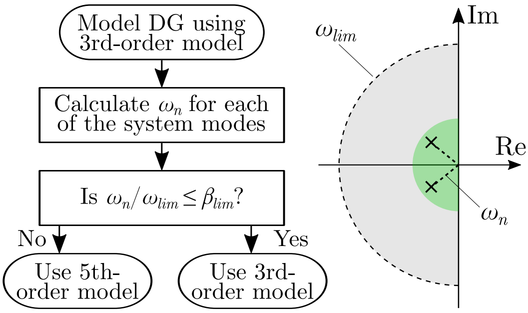

Figure 3.6: Flow diagram for selecting whether to use 3rd- or 5th-order model. © 2021 IEEE.

sient virtual impedances. Hence, this suggests that the stability region of droop-controlled DGs can be enlarged by using quasi-stationary virtual impedances instead of transient virtual impedances.

3.2.2 Proposed Method for Selecting Model Order

As reduced-order models essentially are a trade-off between complexity and accuracy, it is important to consider when the reduced-order model is applicable. To address this issue, a method for selecting the model order is proposed. As noted in Section 2.3.2, the first-order Maclaurin approximation of the network dynamics is only valid for sufficiently small frequencies. Now that the internal dynamics L_o has been included in the model, the criterion in (2.21) can be written as:

$$\left|\frac{sL_t}{R_{eq}+jX_{eq}}\right| \ll 1, \tag{3.12}$$

As an aside, it can be noted that this represents a stricter criterion compared to (2.21), since including the internal dynamics effectively increases the left-hand side of (3.12). By rearranging (3.12), the frequency for which the model is valid is given by:

$$\omega \ll \frac{\sqrt{R_{eq}^2+X_{eq}^2}}{L_t} = \omega_{lim}. \tag{3.13}$$

Hence, the reduced-order model is valid for frequencies much less than ω_{lim}. It can be seen that increasing the quasi-stationary virtual impedances increases ω_{lim}, while increased inner DG impedance reduces it. In addition, it is also evident that including the transient term in the virtual impedances will give a smaller ω_{lim}.

To determine whether the 3rd- or 5th-order model should be used in a given application, the flow diagram in Fig. 3.6 is proposed. In the first step, the DG

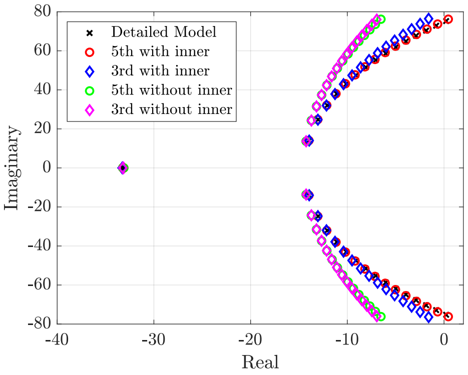

Figure 3.7: Root locus diagram for the detailed model, and 5th-order and 3rd-order models with and without including internal dynamics. © 2021 IEEE.

is modeled by using the 3rd-order model. Subsequently, the natural frequency (ω_n) is calculated for each of the resulting modes. Then, ω_n/ω_{lim} is evaluated to test whether the approximation of the network dynamics is accurate. If the ratio is less than a parameter β_{lim}, the assumption is considered valid, meaning that the 3rd-order model can be applied. Otherwise, the 5th-order model should be used. The value of β_{lim} should be chosen depending on the desired accuracy for the specific application. In particular, if a high degree of accuracy is needed, a low value of β_{lim} should be used.

3.2.3 Analytical Results

To validate the accuracy of the presented reduced-order models, a detailed average model of a DG was used as a benchmark. This model is obtained as described in Section 2.2. Fig. 3.7 displays a root locus diagram when increasing m_p for the detailed model, as well as the 5th- and 3rd-order models with and without inner dynamics. For this case, the transient virtual impedance is used. The 5th-order model including inner dynamics is seen to be the most accurate. Meanwhile, the 3rd-order model including inner dynamics is also quite accurate, although it is predicting a more damped response as the system is approaching the stability limit. Although accurate for low values of m_p, the models neglecting the internal dynamics deviate significantly from the detailed one for larger values of m_p. In particular, the deviation is mainly related to the real value, thereby completely overestimating the damping of the system. This underscores the importance of accounting for the internal dynamics of the DG.

To consider the differences between quasi-stationary and transient virtual

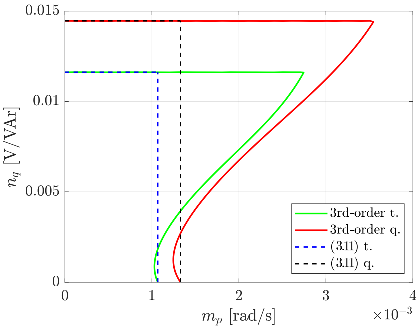

Figure 3.8: Parametric stability limits predicted by the 3rd-order model with transient (t.) and quasi-stationary (q.) virtual impedance. The simplistic estimates based on (3.11) are also shown. © 2021 IEEE.

impedance implementations, consider the parametric stability regions in Fig. 3.8. The stability regions are obtained based on the 3rd-order model in (3.9) for the quasi-stationary (red) and transient (green) virtual impedances. The stable region is to the left and below the curves. The simplistic estimates of the stability region provided by (3.11) are also shown for the quasi-stationary (black) and transient (blue) virtual impedances. For this operating point, the estimates are accurate for the limit on n_q, while they are mostly restrictive for the limit on m_p. Again, it is observed that the system stability region is smaller when using the transient virtual impedance compared to when the quasi-stationary virtual impedance.

3.2.4 Main Contributions

The main results from the paper are summarized in the following:

- It is analytically shown that transient virtual impedances lead to a smaller system stability region compared to quasi-stationary virtual impedances. The improved performance of the latter in terms of low-frequency stability is also shown experimentally.

- A criterion for deciding when reduced-order models of droop-controlled DGs can be used is presented. Although simple, the criterion effectively predicts when the reduced-order model is accurate.

- Despite being several times faster than the slow droop dynamics, it is shown that the internal dynamics can significantly affect the low-frequency dynamics. Hence, this should be included for accurate modeling of the DGs.

3.3 Harmonic Virtual Impedance Design for Optimal Power Quality Management - Paper III

Power quality is an important topic for microgrids due to the proliferation of nonlinear loads. While DGs can be used to improve the power quality, there exists a trade-off between current harmonic sharing and voltage quality, as explained in Section 2.5.1. This trade-off is difficult to manage with a general microgrid configuration with several DGs. To address this issue, an optimization algorithm for determining the harmonic virtual impedances of DGs in a multibus microgrid was presented in this paper. The main objective of the algorithm is to reduce the harmonic voltages of the microgrid nodes. A certain degree of harmonic current sharing between the DGs by selecting a single parameter in the algorithm. Hence, the power quality trade-off between accurate current sharing and harmonic distortion is taken into account in the algorithm.

The work in this paper contributes to answering the first two research questions. Firstly, as the design of the harmonic virtual impedances for improved power quality is addressed, the paper contributes to answering the second research question. A centralized unit calculates the harmonic virtual impedance values of the DGs in the microgrid. These values are updated periodically to account for varying grid conditions. Despite being a centralized unit, this does not interfere with the main function of the droop controller, so that the work also addresses the first research question.

In the following, an overview and discussion of the proposed optimization algorithm are given. In addition, analytical results highlighting the main features of the algorithm are provided.

3.3.1 Overview of Proposed Optimization Algorithm

An overview of the application of the proposed algorithm is shown in Fig. 3.9. In the first step, the harmonic content of the load currents is extracted. Hence, a dedicated current sensor is needed for each load. Subsequently, the harmonic content from all DGs is sent to the microgrid central controller (MGCC). This is used as input to the optimization algorithm, which is run for all harmonics where harmonic virtual impedances are implemented. The harmonic virtual impedances are then sent to all DGs where they are updated. Finally, the process is repeated after a certain time. In practical applications, the duration between updating the harmonic virtual impedances can be quite long. This is because the method is aimed at improving the power quality in steady state. This makes sense considering that standards typically assess harmonic voltages over longer time intervals (e.g. 10 min in EN50160 [74]).

In the following, an overview of the optimization algorithm will be provided.

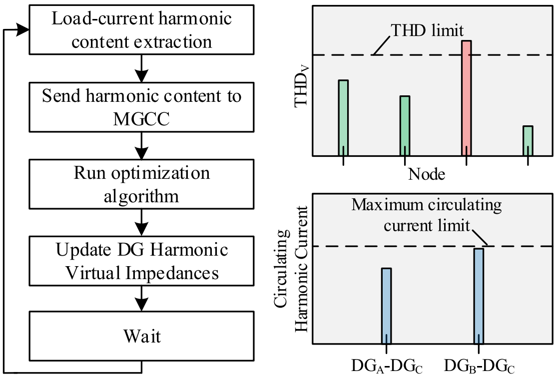

Figure 3.9: Sequence showing the application of the proposed optimization. The optimization reduces node harmonic voltages while ensuring a degree of DG current harmonic sharing. © 2021 IEEE.

In addition to the objective function that minimizes the harmonic voltages, the algorithm contains four constraints:

1. Kirchhoff's Current Law applied to all system nodes.
2. The equivalent harmonic impedances of each DG should be greater than a minimum.
3. Node harmonic voltages should comply with standards.
4. A certain degree of DG current harmonic sharing should be maintained.

The first constraint represents a physical restriction that applies to all nodes in the system. The second constraint limits the excessive use of negative virtual impedances. This is included for preserving the stability of the microgrid. The third constraint ensures that the harmonic voltages are kept within the values specified by standards (e.g. EN 50160 [74]). The fourth constraint reflects the power quality trade-off in terms of current harmonic sharing and voltage quality. A detailed formulation of the optimization algorithm can be found in Appendix A.

The decision variables for the algorithm are the harmonic virtual impedances and the harmonic voltages at the microgrid nodes. Meanwhile, the network impedances and configuration are assumed to be known. While the assumption of a known configuration is reasonable from a system perspective, exact knowledge of the network impedances is unlikely. However, the impedance values are used for several system-level functions, and this is therefore not an unusual assumption. The line impedances can also be readily estimated when the type of conductor and the cable length is known [13], or more advanced methods on line impedance estimation can be used [92].

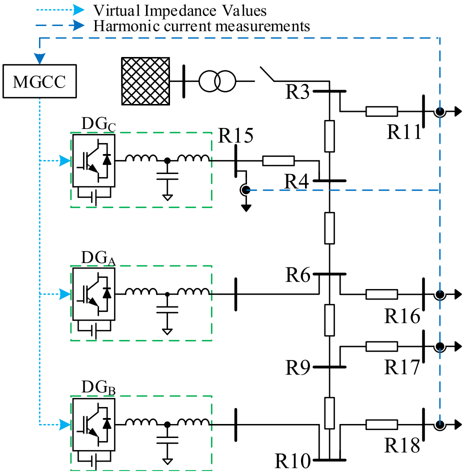

Figure 3.10: Simulated test system based on the microgrid benchmark in [13]. © 2021 IEEE.

3.3.2 Analytical Results

The proposed algorithm was implemented for a microgrid consisting of three DGs and five loads based on the benchmark microgrid in [13]. The system is shown in Fig. 3.10. This system will be used to highlight the ability of the method to vary the trade-off between harmonic sharing and voltage quality. In the optimization algorithm, this is achieved by setting a parameter β. In particular, setting $\beta = 0$ forces equal harmonic sharing between the DGs, while increasing values of β allows for increasing mismatch in the harmonic sharing.

For the simulated case, nonlinear loads were applied at nodes R16 and R17. In addition, all load nodes included linear loads. The following results were obtained for different values of β, upon reaching steady after application of the virtual impedances resulting from the optimization algorithm. Fig. 3.11 (a) shows the THD of the circulating currents between DGA and DGC, and DGB and DGC. For $\beta = 0$, the THD value is very low. This shows that the current harmonics are accurately shared between the DGs. It can also be seen that the THD of the circulating currents increases for increasing values of β. This occurs because β represents a degree of freedom; smaller values enforce sharing between the DGs, while larger values allow a mismatch in the sharing. This degree of freedom is used to improve the voltage quality, as this is set as the main objective. This is clearly shown in Fig. 3.11 (b), which displays the voltage THD at the load nodes for different values of β. The voltage THD is the largest when $\beta = 0$, and it

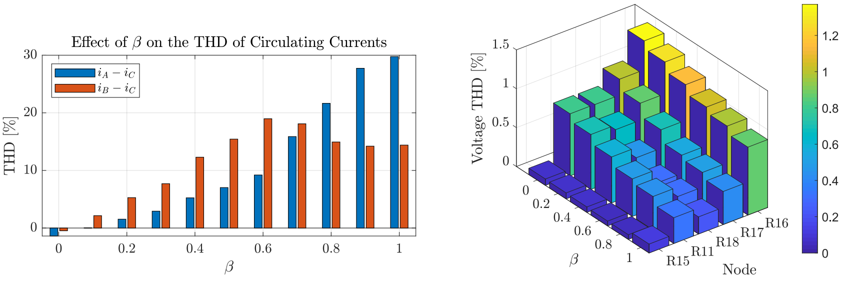

(a) (b)

Figure 3.11: (a) the THD of the circulating currents and (b) the voltage THD at selected nodes when changing the value β. © 2021 IEEE.

decreases for increasing values of β.

3.3.3 Main Contributions

The main contributions from the paper are summarized in the following:

- The optimization algorithm minimizes the voltage THD while ensuring a degree of current harmonic sharing. In this way, the algorithm reflects the trade-off between voltage distortion in the MG nodes and DG harmonic current sharing. This trade-off can be easily adjusted by selecting a parameter of the optimization problem.
- The proposed optimization algorithm is applicable for any MG topology.
- The method does not rely on time-critical communications.

3.4 Discussion

The main objective of the work in this thesis has been to facilitate an increased integration of microgrids and DGs, through the development of models and control strategies. Although they are addressing different aspects, the presented papers contribute to this end. In particular, the accurate and efficient reduced-order model in paper II can be useful in the planning and operation of future microgrids. Meanwhile, the proposed controller in paper I automatically adapts the controllers of the DGs based on the system stability margins, so that the system stability is guaranteed. Thus, this enables increased integration of DGs in a plug-and-play manner. Finally, paper III addresses how the power quality of a generic microgrid can be enhanced by employing the spare capacity of DGs for ancillary services.

As noted in the previous sections, all papers aim at improving the microgrid performance, thereby contributing to answering the first research question. While both papers I and II are related to improving the stability of DGs in microgrids, this is done at different levels. Paper II addresses the stability of a single DG, while paper I is concerned with the stability of the entire microgrid. Hence, these papers somewhat complement each other. Meanwhile, paper III aims at improving the power quality of the microgrid. Similar to paper I, this is performed from a system perspective.

The first research question states that improved performance should be investigated, without compromising the advantages of a decentralized approach. To discuss this in more detail, the advantages of a decentralized approach should be clear. One of the main advantages is the high degree of reliability since no communication between DGs or a central controller is necessary. Hence, no single unit is indispensable for the proper operation of the microgrid. Another advantage of avoiding communication is simplicity. Clearly, as paper II addresses the stability of a single DG, this is a completely decentralized approach. As such, it cannot compromise any of the stated advantages. On the other hand, papers I and III depend on centralized controllers and communication. At the first glance, this might seem to undermine the advantages of the decentralized approach. However, in terms of reliability, the methods in these papers can be considered supplements to the basic control scheme for enhancing the system performance. As such, they are not critical for the system operation, meaning that the basic control scheme will continue to function even if the central controller or the communication breaks down. However, if this occurs, the improved performance provided by the methods will, of course, not be attainable. As for the simplicity, it is clear that the proposed methods add some complexity due to the added communication requirements. Yet, the communication requirements are low for both methods. Considering that some level of communication typically is needed in hierarchically controlled microgrids anyway, the added requirements from the proposed methods will not significantly increase the complexity of the system.

The methods in papers I and III can also be considered a type of secondary control. However, in contrast to the conventional secondary control that sends references for a variable (e.g. active or reactive power references), the methods here send references for a parameter. This has the advantage that the primary controllers act in a distributed way, as in their standard configuration. Then, the secondary controller only modifies the parameter values. This means that any delays only have effects through the parameter update and not through the control loops. Hence, a low update rate can be used without jeopardizing the stability of the system.

The second research question is related to how virtual impedances can be used to improve the performance of the microgrid. Although considering different aspects, both papers II and III address this question as they study outer virtual impedance implementations. In paper II, it is found that a quasi-stationary virtual impedance implementation gives larger system stability margins compared to transient virtual impedances. Meanwhile, paper III addresses how the harmonic current sharing between DGs can be obtained by proper selection of the harmonic virtual impedances. A difference between the papers is that paper III uses a virtual impedance for each harmonic of the output current, while paper II uses a virtual impedance for the entire output current. Paper I does not consider virtual impedances, but it could be of interest to devise a controller that adaptively changes the virtual impedances of the DGs instead of the droop gains.

Chapter 4

Conclusions and Recommendations for Further Work

4.1 Conclusions

The objective of this work was to develop models and control strategies to facilitate a larger deployment of microgrids and DGs. This has been addressed from different points of view for both stability and power quality. Three main contributions have been presented in the thesis. First, a centralized controller was proposed, which adapted the controllers of the DGs according to predefined stability margins. Initially, the system eigenvalues were estimated. Then, depending on the location of these eigenvalues, the controller adapted the droop gains of the DGs. The results demonstrated that the eigenvalue identification was accurate, although the model order needed to be carefully chosen. It was shown that the proposed controller enabled restoring of the desired stability margins within a few control steps. Moreover, the performance of the system did not depend on fast communications and did not adversely impact the advantageous features of the conventional droop control.

Second, a reduced-order DG model considering internal dynamics and virtual impedances were developed. These were modeled by approximating their transfer functions at low frequencies, to obtain an accurate representation of the low-frequency modes of the DG. In addition, a method for deciding the model order was proposed, which was based on analyzing the assumptions used in obtaining the reduced-order model. This provided a straightforward criterion for selecting the model order in studies of larger systems. The model clearly showed the importance of accounting for the internal dynamics, as failing to do so could lead to optimistic estimates of the damping of the dominant modes. Moreover, the model also showed that quasi-stationary virtual impedances led to larger system stability regions than transient virtual impedances.

Finally, an optimization algorithm for setting the harmonic virtual impedances for improving the power quality of multibus microgrids was proposed. The objective function minimized the harmonic voltages at the microgrid nodes, while a degree of current harmonic sharing between the DGs represented one of the constraints. In this way, the method was able to reflect the trade-off between power quality and current harmonic sharing. While the main developments were validated in simulation and experimental work, the experimental validation also showed appreciable differences. In particular, it was noticed that unmodeled sources of harmonics could lead to significant modifications of the expected results.

The three main contributions aimed at improving the stability and power quality of microgrids with droop-controlled DGs. These topics are highly relevant for future microgrids consisting of a large number of DGs, as such microgrids are prone to variable stability margins. In addition, a large amount of DGs also call for a coordinated control strategy for efficient use of the DGs for ancillary service provision. The results of this work contribute to achieving these future microgrids. Specifically, the proposed controller that adaptively ensures the stability margins of a system facilitates plug-and-play functionality of DGs by taking the variable stability margins into account. The proposed reduced-order model also contributes to this end by pointing to the essential elements that may cause low-frequency instability of droop-controlled DGs. In addition, the proposed optimization algorithm enables power quality improvements for microgrids with more complex network topologies. Both of the proposed control strategies adapt according to changing operating conditions, thereby providing the necessary flexibility to the rapidly changing operating points of future microgrids.

4.2 Further work

Several research topics can be pursued as an extension of the research in this thesis. Suggestions for possible directions are included in the list below:

1. While the apparent impedance method has been successfully applied in finding the eigenvalues of smaller systems, it is clear that it can have limited observability of some states for larger systems. Therefore, it would be of interest to investigate how large a system can be while still identifying the system modes. If limited observability occurs, it could also be of interest

if the method could be effectively extended by having several converters identifying the system dynamics.

2. A drawback of the proposed controller is the need for a dedicated converter to identify the apparent impedance. Hence, it would be of interest to incorporate the identification in one of the other DGs. However, in this case, the dynamics of that DG would not be included in the obtained apparent impedance, such that the identification would need to be modified.

3. Although several decentralized control strategies have been proposed for control of DGs, a thorough comparison between these have not been undertaken. Reduced-order models can be valuable to this end, as differences and similarities between the models can more easily be analyzed analytically.

4. In the experimental verification of the proposed optimization algorithm, important differences were observed compared to the analytical results. It would therefore be of interest to investigate more in depth what is contributing to these discrepancies and whether these effects can be incorporated into the optimization algorithm.

5. It could also be of interest to extend the optimization algorithm to include reactive power and unbalance compensation. The necessary measurements would already be in place so that only the algorithm would have to be extended to deal with these cases.

Bibliography

[1] A. Hirsch, Y. Parag, and J. Guerrero, “Microgrids: A review of technologies, key drivers, and outstanding issues,” *Renewable and Sustainable Energy Reviews*, vol. 90, no. April, pp. 402–411, 2018. [Online]. Available: https://doi.org/10.1016/j.rser.2018.03.040

[2] M. Taylor, P. Ralon, H. Anuta, and S. Al-Zoghoul, “Renewable Power Generaztion Costs,” International Renewable Energy Agency, Tech. Rep., 2019.

[3] F. Milano, F. Dörfler, G. Hug, D. J. Hill, and G. Verbič, “Foundations and challenges of low-inertia systems (Invited Paper),” *2018 Power Systems Computation Conference, PSCC*, pp. 1–25, 2018.

[4] D. E. Olivares, A. Mehrizi-Sani, A. H. Etemadi, C. A. Cañizares, R. Iravani, M. Kazerani, A. H. Hajimiragha, O. Gomis-Bellmunt, M. Saeedifard, R. Palma-Behnke, G. A. Jiménez-Estévez, and N. D. Hatziargyriou, “Trends in microgrid control,” *IEEE Transactions on Smart Grid*, vol. 5, no. 4, pp. 1905–1919, 2014.

[5] R. H. Lasseter, “MicroGrids,” *2002 IEEE Power Engineering Society Winter Meeting. Conference Proceedings (Cat. No.02CH37309)*, vol. 1, pp. 305–308, 2002. [Online]. Available: http://ieeexplore.ieee.org/lpdocs/epic03/wrapper.htm?arnumber=985003

[6] D. T. Ton and M. A. Smith, “The U.S. Department of Energy’s Microgrid Initiative,” *Electricity Journal*, vol. 25, no. 8, pp. 84–94, 2012.

[7] “Ensure access to affordable, reliable, sustainable and modern energy for all.” https://unstats.un.org/sdgs/report/2019/goal-07/, accessed: 2021-03-01.

[8] M. Farrokhabadi, D. Lagos, R. W. Wies, M. Paolone, M. Liserre, L. Meegahapola, M. Kabalan, A. H. Hajimiragha, D. Peralta, M. A. Elizondo,

K. P. Schneider, C. A. Canizares, F. K. Tuffner, J. Reilly, J. W. Simpson-Porco, E. Nasr, L. Fan, P. A. Mendoza-Araya, R. Tonkoski, U. Tamrakar, and N. Hatziargyriou, "Microgrid Stability Definitions, Analysis, and Examples," *IEEE Transactions on Power Systems*, vol. 35, no. 1, pp. 13–29, 2020.

[9] B. Adineh, R. Keypour, P. Davari, and F. Blaabjerg, "Review of Harmonic Mitigation Methods in Microgrid: From a Hierarchical Control Perspective," *IEEE Journal of Emerging and Selected Topics in Power Electronics*, vol. 6777, no. c, pp. 1–1, 2020.

[10] P. Vorobev, P. H. Huang, M. A. Hosani, J. L. Kirtley, and K. Turitsyn, "High-Fidelity Model Order Reduction for Microgrids Stability Assessment," *IEEE Transactions on Power Systems*, vol. 33, no. 1, pp. 874–887, 2018.

[11] A. Rygg, "Impedance-based methods for small-signal analysis of systems dominated by power electronics," Ph.D. dissertation, Norwegian University of Science and Technology, 2018.

[12] Y. Gu, N. Bottrell, and T. C. Green, "Reduced-Order Models for Representing Converters in Power System Studies," *IEEE Transactions on Power Electronics*, vol. 33, no. 4, pp. 3644–3654, 2018.

[13] K. Strunz *et al.*, "Benchmark Systems for Network Integration of Renewable and Distributed Energy Resources," Task Force C6, CIGRE, Tech. Rep., 2014.

[14] X. Wang, Y. W. Li, F. Blaabjerg, and P. C. Loh, "Virtual-Impedance-Based Control for Voltage-Source and Current-Source Converters," *IEEE Transactions on Power Electronics*, vol. 30, no. 12, pp. 7019–7037, 2015.

[15] J. Rocabert, A. Luna, F. Blaabjerg, and P. Rodríguez, "Control of Power Converters in AC Microgrids," *IEEE Transactions on Power Electronics*, vol. 27, no. 11, pp. 4734–4749, 2012.

[16] J. M. Guerrero, M. Chandorkar, T. L. Lee, and P. C. Loh, "Advanced control architectures for intelligent microgridspart i: Decentralized and hierarchical control," *IEEE Transactions on Industrial Electronics*, vol. 60, no. 4, pp. 1254–1262, 2013.

[17] E. Espina, J. Llanos, C. Burgos-Mellado, R. Cardenas-Dobson, M. Martinez-Gomez, and D. Saez, "Distributed Control Strategies for Microgrids: An Overview," *IEEE Access*, vol. 8, pp. 193 412–193 448, 2020.

[18] J. M. Guerrero, J. C. Vasquez, J. Matas, L. G. De Vicuña, and M. Castilla, "Hierarchical control of droop-controlled AC and DC microgrids - A general approach toward standardization," *IEEE Transactions on Industrial Electronics*, vol. 58, no. 1, pp. 158–172, 2011.

[19] T. Caldognetto, S. Buso, P. Tenti, and D. I. Brandao, "Power-based control of low-voltage microgrids," *IEEE Journal of Emerging and Selected Topics in Power Electronics*, vol. 3, no. 4, pp. 1056–1066, 2015.

[20] D. I. Brandao, T. Caldognetto, F. P. Marafão, M. G. Simões, J. A. Pomilio, and P. Tenti, "Centralized Control of Distributed Single-Phase Inverters Arbitrarily Connected to Three-Phase Four-Wire Microgrids," *IEEE Transactions on Smart Grid*, vol. 8, no. 1, pp. 437–446, 2017.

[21] M. C. Chandorkar, D. M. Divan, and R. Adapa, "Control of Parallel Connected Inverters in Standalone ac Supply Systems," *IEEE Transactions on Industry Applications*, vol. 29, no. 1, pp. 136–143, 1993.

[22] H. P. Beck and R. Hesse, "Virtual synchronous machine," *2007 9th International Conference on Electrical Power Quality and Utilisation, EPQU*, 2007.

[23] P. Kundur, *Power system stability and control.* New York: McGraw-hill, 1994.

[24] H. Mahmood, D. Michaelson, and J. Jiang, "Accurate reactive power sharing in an islanded microgrid using adaptive virtual impedances," *IEEE Transactions on Power Electronics*, vol. 30, no. 3, pp. 1605–1617, 2015.

[25] Y. Han, H. Li, P. Shen, E. A. A. Coelho, and J. M. Guerrero, "Review of Active and Reactive Power Sharing Strategies in Hierarchical Controlled Microgrids," *IEEE Transactions on Power Electronics*, vol. 32, no. 3, pp. 2427–2451, 2017.

[26] J. M. Guerrero, J. Matas, L. G. Vicuña, M. Castilla, and J. Miret, "Decentralized control for parallel operation of distributed generation inverters using resistive output impedance," *IEEE Transactions on Industrial Electronics*, vol. 54, no. 2, pp. 994–1004, 2007.

[27] K. De Brabandere, B. Bolsens, J. Van Den Keybus, A. Woyte, J. Driesen, and R. Belmans, "A voltage and frequency droop control method for parallel inverters," *IEEE Transactions on Power Electronics*, vol. 4, pp. 1107–1115, 2007.

[28] W. Yao, M. Chen, J. Matas, J. M. Guerrero, and Z. M. Qian, "Design and analysis of the droop control method for parallel inverters considering the

impact of the complex impedance on the power sharing," *IEEE Transactions on Industrial Electronics*, vol. 58, no. 2, pp. 576–588, 2011.

[29] J. Guerrero, J. Matas, L. Garcia de Vicuna, M. Castilla, and J. Miret, "Wireless-Control Strategy for Parallel Operation of Distributed-Generation Inverters," *IEEE Transactions on Industrial Electronics*, vol. 53, no. 5, pp. 1461–1470, 2006.

[30] Y. Mohamed and E. F. El-Saadany, "Adaptive Decentralized Droop Controller to Preserve Power Sharing Stability of Paralleled Inverters in Distributed Generation Microgrids," *IEEE Transactions on Power Electronics*, vol. 23, no. 6, pp. 2806–2816, 2008.

[31] Y. Sun, X. Hou, J. Yang, H. Han, M. Su, and J. M. Guerrero, "New Perspectives on Droop Control in AC Microgrid," *IEEE Transactions on Industrial Electronics*, vol. 64, no. 7, pp. 5741–5745, 2017.

[32] Y. W. Li and C. Kao, "An accurate power control strategy for power-electronics-interfaced distributed generation units operating in a low-voltage multibus microgrid," *IEEE Transactions on Power Electronics*, vol. 24, no. 12, pp. 2977–2988, 2009.

[33] P. Piagi and R. H. Lasseter, "Autonomous control of microgrids," *2006 IEEE Power Engineering Society General Meeting, PES*, 2006.

[34] S. D'Arco, J. A. Suul, and O. B. Fosso, "Control System Tuning and Stability Analysis of Virtual Synchronous Machines," *2013 IEEE Energy Conversion Congress and Exposition, ECCE 2013*, pp. 2664–2671, 2013.

[35] N. Pogaku, M. Prodanović, and T. C. Green, "Modeling, analysis and testing of autonomous operation of an inverter-based microgrid," *IEEE Transactions on Power Electronics*, vol. 22, no. 2, pp. 613–625, 2007.

[36] Y. W. Li, "Control and resonance damping of voltage-source and current-source converters with LC filters," *IEEE Transactions on Industrial Electronics*, vol. 56, no. 5, pp. 1511–1521, 2009.

[37] D. De and V. Ramanarayanan, "Decentralized parallel operation of inverters sharing unbalanced and nonlinear loads," *IEEE Transactions on Power Electronics*, vol. 25, no. 12, pp. 3015–3025, 2010.

[38] R. Teodorescu, F. Blaabjerg, M. Liserre, and P. C. Loh, "Proportional-resonant controllers and filters for grid-connected voltage-source converters," *IEE Proceedings - Electric Power Applications*, vol. 153, no. 5, pp. 750–762, 2006.

[39] J. M. Guerrero, L. G. Vicuña, J. Matas, M. Castilla, and J. Miret, “Output impedance design of parallel-connected UPS inverters with wireless load sharing control,” *IEEE Transactions on Industrial Electronics*, vol. 52, no. 4, pp. 1126–1135, 2005.

[40] J. He and Y. W. Li, “Analysis, Design, and Implementation of Virtual Impedance for Power Electronics Interfaced Distributed Generation,” *IEEE Transactions on Industry Applications*, vol. 47, no. 6, pp. 2525–2538, 11 2011.

[41] P. H. Huang, P. Vorobev, M. Al Hosani, J. L. Kirtley, and K. Turitsyn, “Plug-and-Play Compliant Control for Inverter-Based Microgrids,” *IEEE Transactions on Power Systems*, vol. 34, no. 4, pp. 2901–2913, 2019.

[42] U. Borup, F. Blaabjerg, and P. N. Enjeti, “Sharing of nonlinear load in parallel-connected three-phase converters,” *IEEE Transactions on Industry Applications*, vol. 37, no. 6, pp. 1817–1823, 2001.

[43] X. Wang, F. Blaabjerg, and Z. Chen, “Autonomous Control of Inverter - Interfaced Distributed Generation Units for Harmonic Current Filtering and Resonance Damping in an Islanded Microgrid,” *IEEE Transactions on Industry Applications*, vol. 50, no. 1, pp. 452–461, 2014.

[44] J. He, Y. W. Li, and F. Blaabjerg, “An Enhanced Islanding Microgrid Reactive Power, Imbalance Power, and Harmonic Power Sharing Scheme,” *IEEE Transactions on Power Electronics*, vol. 30, no. 6, pp. 3389–3401, 2015.

[45] E. A. A. Coelho, P. C. Cortizo, and P. F. D. Garcia, “Small-Signal Stability for Parallel-Connected Inverters in Stand-Alone ac Supply Systems,” *IEEE Transactions on Industry Applications*, vol. 38, no. 2, pp. 533–542, 2002.

[46] J. M. Guerrero, L. G. de Vicuna, J. Matas, M. Castilla, and J. Miret, “A wireless controller to enhance dynamic performance of parallel inverters in distributed generation systems,” *IEEE Transactions on Power Electronics*, vol. 19, no. 5, pp. 1205–1213, 2004.

[47] S. V. Iyer, M. N. Belur, and M. C. Chandorkar, “A Generalized Computational Method to Determine Stability of a Multi-inverter Microgrid,” *IEEE Transactions on Power Electronics*, vol. 25, no. 9, pp. 2420–2432, 2010.

[48] X. Guo, Z. Lu, B. Wang, X. Sun, L. Wang, and J. M. Guerrero, “Dynamic Phasors-Based Modeling and Stability Analysis of Droop-Controlled Inverters for Microgrid Applications,” *IEEE Transactions on Smart Grid*, vol. 5, no. 6, pp. 2980–2987, 2014.

[49] L. Luo and S. V. Dhople, “Spatiotemporal model reduction of inverter-based islanded microgrids,” *IEEE Transactions on Energy Conversion*, vol. 29, no. 4, pp. 823–832, 2014.

[50] V. Mariani, F. Vasca, J. C. Vásquez, and J. M. Guerrero, “Model Order Reductions for Stability Analysis of Islanded Microgrids With Droop Control,” *IEEE Transactions on Industrial Electronics*, vol. 62, no. 7, pp. 4344–4354, 2015.

[51] G. Raman and J. C. H. Peng, “Mitigating Stability Issues Due to Line Dynamics in Droop-Controlled Multi-Inverter Systems,” *IEEE Transactions on Power Systems*, vol. 35, no. 3, pp. 2082–2092, 2020.

[52] H. Yu, J. Su, Y. Wang, H. Wang, and Y. Shi, “Modeling Method and Applicability Analysis of Inverter’s Reduced-Order Model for Microgrid Applications,” *IET Power Electronics*, 2020.

[53] S. Leitner, M. Yazdanian, A. Mehrizi-Sani, and A. Muetze, “Small-Signal Stability Analysis of an Inverter-Based Microgrid with Internal Model-Based Controllers,” *IEEE Transactions on Smart Grid*, vol. 9, no. 5, pp. 5393–5402, 2018.

[54] R. D. Middlebrook, “Input filter considerations in design and application of switching regulators,” *IEEE Industry Applications Society Annual Meeting*, 1976.

[55] M. Belkhayat, “Stability criteria for AC power systems with regulated loads,” Ph.D. dissertation, Purdue University, 1997.

[56] L. Harnefors, M. Bongiorno, and S. Lundberg, “Input-admittance calculation and shaping for controlled voltage-source converters,” *IEEE Transactions on Industrial Electronics*, vol. 54, no. 6, pp. 3323–3334, 2007.

[57] B. Wen, D. Boroyevich, R. Burgos, P. Mattavelli, and Z. Shen, “Analysis of D-Q Small-Signal Impedance of Grid-Tied Inverters,” *IEEE Transactions on Power Electronics*, vol. 31, no. 1, pp. 675–687, 2016.

[58] M. Cespedes and J. Sun, “Adaptive control of grid-connected inverters based on online grid impedance measurements,” *IEEE Transactions on Sustainable Energy*, vol. 5, no. 2, pp. 516–523, 2014.

[59] M. Amin and M. Molinas, “Small-Signal Stability Assessment of Power Electronics Based Power Systems : A Discussion of Impedance- And Eigenvalue-Based Methods,” *IEEE Transactions on Industry Applications*, vol. 53, no. 5, pp. 5014–5030, 2017.

[60] J. Sun, "Small-signal methods for AC distributed power systems-A review," *IEEE Transactions on Power Electronics*, vol. 24, no. 11, pp. 2545–2554, 2009.

[61] A. Rygg, M. Molinas, Z. Chen, and X. Cai, "A Modified Sequence Domain Impedance Definition and Its Equivalence to the dq-Domain Impedance Definition for the Stability Snalysis of AC Power Electronic Systems," *IEEE Journal of Emerging and Selected Topics in Power Electronics*, vol. 4, no. 4, pp. 1383–1396, 2016. [Online]. Available: http://arxiv.org/abs/1605.00526

[62] Y. A. Familiant, J. Huang, K. A. Corzine, and M. Belkhayat, "New Techniques for Measuring Impedance Characteristics of Three-Phase AC Power Systems," *IEEE Transactions on Power Electronics*, vol. 24, no. 7, pp. 1802–1810, 2009.

[63] G. Francis, R. Burgos, D. Boroyevich, F. Wang, and K. Karimi, "An algorithm and implementation system for measuring impedance in the D-Q domain," *IEEE Energy Conversion Congress and Exposition: Energy Conversion Innovation for a Clean Energy Future, ECCE 2011, Proceedings*, pp. 3221–3228, 2011.

[64] T. Roinila, M. Vilkko, and J. Sun, "Broadband methods for online grid impedance measurement," *2013 IEEE Energy Conversion Congress and Exposition, ECCE 2013*, pp. 3003–3010, 2013.

[65] ——, "Online grid impedance measurement using discrete-interval binary sequence injection," *IEEE Journal of Emerging and Selected Topics in Power Electronics*, vol. 2, no. 4, pp. 985–993, 2014.

[66] A. Riccobono, M. Mirz, and A. Monti, "Noninvasive Online Parametric Identification of Three-Phase AC Power Impedances to Assess the Stability of Grid-Tied Power Electronic Inverters in LV Networks," *IEEE Journal of Emerging and Selected Topics in Power Electronics*, vol. 6, no. 2, pp. 629–647, 2018.

[67] J. Sun, "Impedance-based stability criterion for grid-connected inverters," *IEEE Transactions on Power Electronics*, vol. 26, no. 11, pp. 3075–3078, 2011.

[68] A. Rygg, M. Amin, M. Molinas, and B. Gustavsen, "Apparent impedance analysis: A new method for power system stability analysis," *2016 IEEE 17th Workshop on Control and Modeling for Power Electronics, COMPEL 2016*, 2016.

[69] A. Rygg and M. Molinas, “Apparent Impedance Analysis: A Small-Signal Method for Stability Analysis of Power Electronic-Based Systems,” *IEEE Journal of Emerging and Selected Topics in Power Electronics*, vol. 5, no. 4, pp. 1474–1486, 2017.

[70] B. Gustavsen and A. Semlyen, “Rational Approximation of Frequency Domain Responses By Vector Fitting,” *IEEE Transactions on Power Delivery*, vol. 14, no. 3, pp. 1052–1061, 1999.

[71] B. Gustavsen, “Improving the pole relocating properties of vector fitting,” *2006 IEEE Power Engineering Society General Meeting, PES*, vol. 21, no. 3, pp. 1587–1592, 2006.

[72] D. Deschrijver, M. Mrozowski, T. Dhaene, and D. De Zutter, “Macromodeling of Multiport Systems Using a Fast Implementation of the Vector Fitting Method,” *IEEE Microwave and Wireless Components Letters*, vol. 18, no. 6, pp. 383–385, 2008.

[73] “The Vector Fitting.” https://www.sintef.no/projectweb/vectorfitting/, accessed: 2021-02-22.

[74] *Voltage Characteristics of Electricity Supplied by Public Electricity Networks.* CENELC Standard EN 50160:2010, 2010.

[75] *IEEE Recommended Practice and Requirements for Harmonic Control in Electric Power Systems.* IEEE Std. 519-2014, 2014.

[76] H. Akagi, “New Trends in Active Filters for Power Conditioning,” *IEEE Transactions on Industry Applications*, vol. 32, no. 6, pp. 1312–1322, 1996.

[77] P. Sreekumar and V. Khadkikar, “A New Virtual Harmonic Impedance Scheme for Harmonic Power Sharing in an Islanded Microgrid,” *IEEE Transactions on Power Delivery*, vol. 31, no. 3, pp. 936–945, 2016.

[78] T. L. Lee and P. T. Cheng, “Design of a New Cooperative Harmonic Filtering Strategy for Distributed Generation Interface Converters in an Islanding Network,” *IEEE Transactions on Power Electronics*, vol. 22, no. 5, pp. 1919–1927, 2007.

[79] E. H. Watanabe, R. M. Stephan, and M. Aredes, “New Concepts of Instantaneous Active and Reactive Powers in Electrical Systems With Generic Loads,” *IEEE Transactions on Power Delivery*, vol. 8, no. 2, 1993.

[80] H. Moussa, A. Shahin, J. P. Martin, B. Nahid-Mobarakeh, S. Pierfederici, and N. Moubayed, “Harmonic Power Sharing with Voltage Distortion Compensation of Droop Controlled Islanded Microgrids,” *IEEE Transactions on Smart Grid*, vol. 9, no. 5, pp. 5335–5347, 2018.

[81] M. Savaghebi, A. Jalilian, J. C. Vasquez, and J. M. Guerrero, “Secondary Control for Voltage Quality Enhancement in Microgrids,” *IEEE Transactions on Smart Grid*, vol. 3, no. 4, p. 4799, 2012.

[82] L. Meng, F. Tang, M. Savaghebi, J. C. Vasquez, and J. M. Guerrero, “Tertiary control of voltage unbalance compensation for optimal power quality in islanded microgrids,” *IEEE Transactions on Energy Conversion*, vol. 29, no. 4, pp. 802–815, 2014.

[83] X. Zhao, L. Meng, C. Xie, J. M. Guerrero, and X. Wu, “A Unified Voltage Harmonic Control Strategy for Coordinated Compensation with VCM and CCM Converters,” *IEEE Transactions on Power Electronics*, vol. 33, no. 8, pp. 7132–7147, 2018.

[84] T. Vandoorn, B. Meersman, J. De Kooning, and L. Vandevelde, “Controllable harmonic current sharing in islanded microgrids: DG units with programmable resistive behavior toward harmonics,” *IEEE Transactions on Power Delivery*, vol. 27, no. 2, pp. 831–841, 2012.

[85] A. Micallef, M. Apap, C. Spiteri-Staines, J. M. Guerrero, and J. C. Vasquez, “Reactive power sharing and voltage harmonic distortion compensation of droop controlled single phase islanded microgrids,” *IEEE Transactions on Smart Grid*, vol. 5, no. 3, pp. 1149–1158, 2014.

[86] A. Micallef, M. Apap, C. Spiteri-Staines, and J. M. Guerrero, “Mitigation of Harmonics in Grid-Connected and Islanded Microgrids Via Virtual Admittances and Impedances,” *IEEE Transactions on Smart Grid*, vol. 8, no. 2, pp. 651–661, 2017.

[87] C. Blanco, D. Reigosa, J. C. Vasquez, J. M. Guerrero, and F. Briz, “Virtual Admittance Loop for Voltage Harmonic Compensation in Microgrids,” *IEEE Transactions on Industry Applications*, vol. 52, no. 4, pp. 3348–3356, 2016.

[88] C. Blanco, F. Tardelli, D. Reigosa, P. Zanchetta, and F. Briz, “Design of a cooperative voltage harmonic compensation strategy for islanded microgrids combining virtual admittance and repetitive controller,” *IEEE Transactions on Industry Applications*, vol. 55, no. 1, pp. 680–688, 2019.

[89] L. Meng and J. M. Guerrero, “Optimization for Customized Power Quality Service in Multibus Microgrids,” *IEEE Transactions on Industrial Electronics*, vol. 64, no. 11, pp. 8767–8777, 2017.

[90] R. Keypour, B. Adineh, M. H. Khooban, and F. Blaabjerg, “A New Population-Based Optimization Method for Online Minimization of Voltage Harmonics in Islanded Microgrids,” *IEEE Transactions on Circuits and Systems II: Express Briefs*, vol. 67, no. 6, pp. 1084–1088, 2020.

[91] M. M. Hashempour, T. L. Lee, M. Savaghebi, and J. M. Guerrero, “Real-time supervisory control for power quality improvement of multi-area microgrids,” *IEEE Systems Journal*, vol. 13, no. 1, pp. 864–874, 2019.

[92] S. Han, D. Kodaira, S. Han, B. Kwon, Y. Hasegawa, and H. Aki, “An Automated Impedance Estimation Method in Low-Voltage Distribution Network for Coordinated Voltage Regulation,” *IEEE Transactions on Smart Grid*, vol. 7, no. 2, pp. 1012–1020, 2016.

[93] F. Huerta, J. K. Gruber, M. Prodanovic, and P. Matatagui, “A power-HIL microgrid testbed: Smart Energy Integration Lab (SEIL),” *2014 IEEE Energy Conversion Congress and Exposition, ECCE 2014*, pp. 3998–4003, 2014.

Publications

Paper I

The paper ”Apparent Impedance-Based Adaptive Controller for Improved Stability of Droop-Controlled Microgrid” is published in *IEEE Transactions on Power Electronics.*

© 2021 IEEE. Reprinted, with permission, from F. Göthner, R. E. Torres-Olguin, J. Roldán-Pérez, A. Rygg and O. -M. Midtgård, ”Apparent Impedance-Based Adaptive Controller for Improved Stability of a Droop-Controlled Microgrid,” in *IEEE Transactions on Power Electronics*, vol. 36, no. 8, pp. 9465-9476, Aug. 2021, doi: 10.1109/TPEL.2021.3050615.

Apparent Impedance-Based Adaptive Controller for Improved Stability of Droop-Controlled Microgrid

Fredrik Göthner, Raymundo E. Torres-Olguin, Javier Roldán-Pérez, *Member, IEEE*,
Atle Rygg, and Ole-Morten Midtgård, *Member, IEEE*.

***Abstract*—Droop control is the most common approach for controlling microgrids (MGs) and interfacing distributed generators (DGs) due to its inherent power-sharing characteristics and low dependence on communication systems. However, the stability of MGs operated with this control paradigm is sensitive to the droop parameter values and system topology. This situation will be even more challenging in future grid scenarios, where system reconfiguration and parameter uncertainty will become more relevant. In this paper, a centralized controller for improving the stability margins of a MG is proposed. Firstly, the apparent impedance of the MG is periodically identified by injecting a multi-tone current perturbation. Then, the matrix fitting technique is applied to calculate the system eigenvalues based on the estimated apparent impedance. Depending on the location of the dominant eigenvalues, the droop gains are modified by using a control law to ensure sufficient stability margins. No previous information of the system topology or parameter values is required. It is shown that this method can greatly improve stability margins without compromising the inherent power sharing, transient performance and low dependence on communication systems of the droop control. Simulation and experimental results for a MG based on DGs rated at 60 kVA are included to validate the proposed control scheme.**

***Index Terms*—Microgrid Control, Impedance Estimation, Adaptive Control, Apparent Impedance Analysis.**

I. INTRODUCTION

MICROGRIDS (MGs) have gained attention in recent years since they facilitate the integration of renewable energy sources in electrical distribution systems [1]. Several philosophies have been adopted for controlling MGs, including centralized and decentralized approaches. Centralized approaches such as master-slave schemes rely on communication between a master controller and local controllers [2]. Although such schemes perform well, the reliability has been questioned due to the dependence on communication. Moreover, failures in the master controller can cause a complete system shutdown. Meanwhile, decentralized approaches such as power-frequency droops [3] and virtual synchronous machines [4] are by far more common in the literature. The advantage of decentralized schemes lies in their low dependence on communications systems, which is paving the way for plug-and-play capability. However, the stability of decentrally-controlled MGs is known to be sensitive to the droop control parameters, especially when the MG is working isolated from the main grid. This is particularly challenging for MG configurations in which line impedances are small and predominantly resistive, which is common in low-voltage networks [5, 6].

Several control modifications have been proposed to address this stability issue. One popular approach is to emulate an additional impedance at the output terminal of the DG by using virtual impedances [7–9]. This technique virtually increases the electrical distance between DGs, thereby improving the stability margins. However, voltage regulation is worsened, and this can have a negative impact when large loads are suddenly connected to the MG. Another common approach for improving stability margins is to modify the droop control law. Firstly, depending on the R/X ratio of the electrical connection, the active power-voltage and reactive power-frequency relations are altered [7]. For inductive grids, the classical active power-frequency and reactive power-voltage relations can be applied. However, for dominantly resistive grids, there is a strong coupling between voltage and active power, and frequency and reactive power. Under these circumstances, opposite droops should be used [10]. For R/X ratios around unity, both voltage and frequency are coupled with active and reactive power. In this case, a mixed droop approach should be applied [11]. Another control technique that can be applied under these circumstances is called virtual power [12]. For this technique, the actual active and reactive powers are transformed by using a rotation angle. The result is “virtual powers”, to which traditional droop control can be applied. In addition to the modified droops and their alternatives mentioned before, derivative terms have also been proposed to improve voltage and frequency regulation [10, 13]. This approach can effectively reduce the coupling between voltage and frequency control loops, similarly to the virtual impedance approach [14].

Hierarchical control approaches have also been extensively used to improve the performance of decentralized control schemes [15]. In these approaches, the primary control is decentralized, while the secondary and tertiary layers typically use communication systems. The secondary control has been used to restore the system operating point (e.g. removing steady state frequency and voltage deviations) [16–18] or to handle unbalance compensation [19]. The mismatch in reactive power sharing between DG units have also been addressed by using a secondary controller [20, 21]. Moreover,

This work has been funded by CINELDI - Centre for intelligent electricity distribution, an 8-year Research Centre under the FME-scheme (Centre for Environment-friendly Energy Research, 257626/E20). The authors gratefully acknowledge the financial support from the Research Council of Norway and the CINELDI partners. The work of IMDEA Energy Institute received financial through the research programme S2018/EMT-4366 PROMIT-CAM of Madrid Government, with 50% support of the European Social Fund.

Fredrik Göthner and Ole-Morten Midtgård are with the Norwegian University of Science and Technology 7034, Trondheim, Norway (e-mail: fredrik.gothner@ntnu.no; ole-morten.midtgard@ntnu.no).

Raymundo E. Torres-Olguin is with SINTEF Energy Research, 7034 Trondheim, Norway (e-mail: raymundo.torres-olguin@sintef.no).

Javier Roldán-Pérez is with IMDEA Energy Institute, Madrid, 28935 Spain (e-mail: javier.roldan@imdea.org).

Atle Rygg is with the Department of Engineering Cybernetics, Norwegian University of Science and Technology, 7034 Trondheim, Norway (atle.rygg@ntnu.no).

the hierarchical control structure has been used to update control parameters online [22, 23]. However, in these works, it is assumed that the system configuration and parameters are known in order to update the controller.

The massive integration of DGs in future power networks will inevitably reduce the electrical distance (and thereby the impedance value) between DGs [6, 24]. Other factors such as ambient temperature and loading conditions also affect line impedance values [25]. This makes the MG stability margins highly dependent on the actual operating conditions. Therefore, to achieve plug-and-play capability, the MG control system must be able to adapt itself according to these variable (and many times unpredictable) scenarios. A solution is proposed by Huang *et al.* [26]. In that work, virtual impedance values are set large enough so that MG stability is guaranteed for a given set of droop parameters. This solution is robust and provides adequate stability margins for any working condition. However, the resulting virtual impedances are large, and this restricts the transient performance of the MG.

State-space methods have traditionally been used for analyzing power systems dynamics. These methods require detailed information of each network component. For traditional power systems based on large rotating electric machines, this problem can be adequately addressed including all the details of generators and their control loops. However, in electrical systems dominated by a large number of DGs, the problem becomes intractable. In this case, system identification techniques are a solution to analyze power system dynamics without detailed system information [27]. These methods only use time-domain measurements as inputs. The output can be the dominant modes or low-order linear models of the system. Several types of identification methods have been used in the literature, such as ringdown and mode-meter algorithms [28]. However, in order to obtain accurate results, reliable real-time synchronized measurement systems are typically needed.

As an alternative, impedance-based techniques have been increasingly applied to ac power systems over the last decades decades [29, 30]. In this case, the system is split into source and load subsystems, and stability is guaranteed if the ratio between the subsystem impedances satisfies the Nyquist stability criterion (provided that each subsystem is stable by itself) [31]. The main advantage of this method is that stability is determined by using the impedance measured at the interconnection point. This removes the need for detailed information of internal state variables and system parameters. On the other hand, limited observability of certain states might occur depending on where the system is partitioned [32]. A related version of traditional impedance methods is the apparent impedance analysis [33]. Instead of using the source and load impedances individually, this method estimates the equivalent impedance seen from the point of injection. This *apparent impedance* can be readily estimated by using frequency sweeps and system identification techniques such as matrix fitting [33, 34]. The main advantage of using the apparent impedance is that it represents a closed-loop transfer function in the system. Hence, the system eigenvalues can be estimated without previous knowledge of the grid configuration or parameter values. Impedance-based methods have also been used for adaptive control of DGs based on the estimated grid impedance seen from the converter [35, 36]. This can improve the performance and stability margins under varying grid conditions. However, the power quality of the grid might significantly worsen if many DGs actively estimate the grid impedance simultaneously. Moreover, the adaptive control in these methods only guarantee the stability of individual DGs.

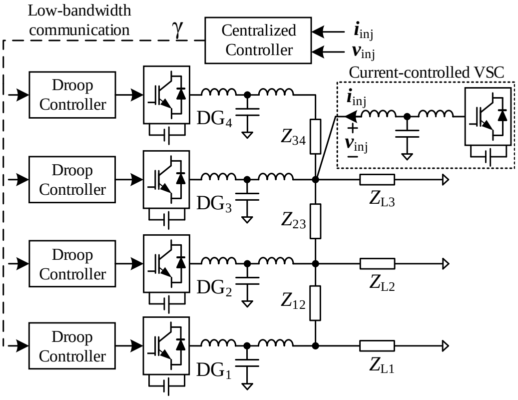

Fig. 1. MG topology, including internal loops and the proposed controller.

In this paper, a controller that adapts the droop coefficients of an MG to safeguard its stability is presented. The adaptation process is based on estimated system eigenvalues, which are calculated by using apparent impedance analysis and matrix fitting. The apparent impedance is obtained by perturbing the system with a single dedicated converter, thereby minimizing adverse power quality effects. Subsequently, the active power droop gain is updated for all DGs depending on the location of the system eigenvalues. By using this approach, all DGs cooperate to ensure sufficient stability margins and adequate performance. Conditions to guarantee the stable operation of this control law are derived. Also, the performance of the control system will be explored by using analytical derivations and simulations. Finally, experimental results are presented to validate the main contributions.

The rest of the paper is organized as follows. In Section II, the application is described, including a short overview of DG controllers and the proposed control technique. In Section III, the proposed controller is derived, while the apparent impedance analysis is explained in Section IV. Simulation and experimental results are presented in Sections V and VI. Section VII provides a discussion of the method, while the conclusions are drawn in Section VIII.

II. APPLICATION OVERVIEW

A. Microgrid Description

Fig. 1 shows the islanded MG considered in this work. It consists of four DGs connected via LCL filters, three loads, three lines, and an additional current-controlled voltage source converter (CC-VSC). The DGs regulate the MG voltage and frequency cooperatively by using conventional Pf and QV droop controllers. The line impedances are denoted by Z_{ij}, where i and j are the nodes interconnected by the line.

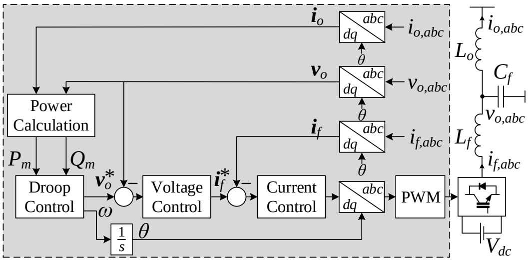

Fig. 2. Hardware and control diagram of a droop-controlled DG.

The loads are denoted by Z_{Li}. Both loads and lines are modelled as RL equivalent circuits. The CC-VSC is in charge of identifying the system dynamics. The injected current of the CC-VSC ($\boldsymbol{i}_{inj}$) and resulting voltage ($\boldsymbol{v}_{inj}$) serve as input to the proposed adaptive controller. This controller regularly outputs the variable γ through a low-bandwidth communication channel. Bold variables are referred to a synchronous reference frame (SRF) (e.g. $\boldsymbol{x} = x_d + jx_q$).

B. DG Control Overview

Fig. 2 presents the droop-controlled DG considered in this work. The inner current controller regulates the current through the converter-side inductance (L_f), while the outer voltage loop regulates the voltage across the filter capacitor (C_f). The inner loops are devised in an SRF and they include PI controllers with appropriate feedforward and decoupling terms [5]. The outer Pf and QV droop controllers enable parallel operation of DGs. For the conventional droop controllers, active power is drooped against frequency and reactive power is drooped against voltage [3]:

$$\omega = \omega^* - m_p P, \quad E = E^* - n_q Q, \tag{1}$$

where ω and ω^* are the DG frequency and its reference value, E and E^* are the DG voltage magnitude and its reference value, while m_p and n_q are the active and reactive power droop gains. The terms P and Q are filtered values of the DG output active and reactive powers:

$$P = \frac{1}{1+T_f s} P_m, \quad Q = \frac{1}{1+T_f s} Q_m, \tag{2}$$

where s is the Laplace variable, T_f is the low-pass filter time constant, while P_m and Q_m denote the measured active and reactive power of the DG. The angle for Park transformations is obtained by integrating the frequency (ω), in (1).

C. Proposed Control System Overview

Fig. 3 (a) shows a flowchart summarizing the proposed controller. In the first step, two regions of the complex plane are defined. These are denoted allowed and damped regions. The main objective of the control system is to place the dominant (low-frequency) poles of the MG inside the allowed region. This region is defined by a minimum allowed damping ratio (ζ_-), as shown in Fig. 3 (b). The damped region is a subset of the allowed region. This region is defined by the minimum damping ratio (ζ_+). Also, as only the dominant poles will be addressed with the controller, an upper bound for their natural frequency is defined (ω_{lim}). By limiting the frequency of the poles of interest, the high-frequency poles related to electromagnetic phenomena (e.g. fast-inner controllers) can be discerned from the low-frequency ones that dominate the power flow dynamics.

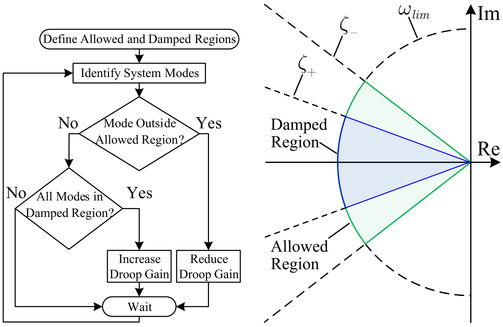

(a) (b)

Fig. 3. (a) Flowchart of the proposed control and (b) allowed and damped regions for the system eigenvalues.

In the second step, the dominant low-frequency modes are identified by using apparent impedance analysis. The data required to identify the model is obtained from a dedicated converter (see Fig. 1). A low-magnitude multi-tone current is used to estimate the apparent impedance without threatening the MG power quality. Subsequently, the matrix fitting technique is used to estimate the system state-space model. The application of the apparent impedance analysis and matrix fitting is explained in detail in Section IV. If any mode is outside the allowed region, the centralized controller reduces the active power droop gains (by reducing γ) to increase the system stability margins. If instead all the modes are inside the allowed region, the method checks if all of them are in the damped region. If so, the MG is unnecessarily damped and the controller increases the active power droop gains (by increasing γ). If all modes are in the allowed region, but not all are in the damped region, no change in the control system occurs. Finally, the system waits before the process repeats. This is further explained in Section III. The development and analysis of this control method is the main contribution of this work.

D. Small-Signal Model of the MG

In order to verify whether the identified eigenvalues are correctly estimated, an analytical small-signal model of the MG in Fig. 1 is developed. This model is found by calculating a linearized state-space representation of each DG, line and load, independently. Afterwards, the submodels are aggregated in a single state-space representation [5]. The models of each subsystem should be referred to a common reference frame (DQ), which is aligned with the reference frame of DG1. Lines and loads are directly modelled in the common reference frame, while DG units are modelled in their own reference

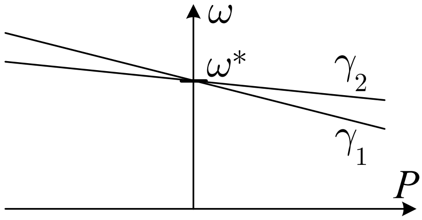

Fig. 4. Effect that the central controller gain (γ) has on the droop control law. Here, $\gamma_1 > \gamma_2$.

frame. To aggregate the models, the following reference frame transformation should be performed:

$$\begin{bmatrix} x_D \\ x_Q \end{bmatrix} = \begin{bmatrix} \cos\delta_i & -\sin\delta_i \\ \sin\delta_i & \cos\delta_i \end{bmatrix} \begin{bmatrix} x_d \\ x_q \end{bmatrix}, \tag{3}$$

where δ_i is the angle difference between the reference frame of a DG (dq_i) and the common reference frame (DQ). For details regarding state-space modelling of MGs with DGs, lines and loads, see [5].

III. PROPOSED CONTROL METHOD

In this section, the proposed control for droop-controlled MGs is presented. Also, conditions to guarantee stability are derived.

A. Proposed Control

Many droop-controlled MG topologies have already been analyzed by using participation factor analysis. In these works, it was found that low-frequency modes are mainly associated with the states of the droop controller [5, 13]. This suggests that the low-pass filter time constant or droop gains could be used for relocating the low-frequency modes. More specifically, the active power and angle states have the most relevant impact [5]. These findings are supported by the reduced-order models in [6], where it is shown that the active power droop gain is typically limiting stability for practical tuning of droop controllers. This means that altering m_p is the most direct method for shifting the low-frequency modes. However, altering n_q or T_f might also be of interest depending on the MG application.

The following modified active power droop control is proposed in order to adjust the position of the low-frequency modes:

$$\omega = \omega^* - \gamma m_p P, \quad \gamma \in (0, 1], \tag{4}$$

where γ is calculated by the centralized controller. Its value is specified recursively, depending on the location of the identified modes:

$$\gamma[k] = \begin{cases} \alpha_i \gamma[k-1], \text{ if } \zeta_i \geq \zeta_+ \vee |\lambda_i| \geq \omega_{lim} \; \forall i \\ \quad \gamma[k-1], \text{ if } \zeta_i \geq \zeta_- \vee |\lambda_i| \geq \omega_{lim} \; \forall i \\ \alpha_r \gamma[k-1], \text{ otherwise} \end{cases} \tag{5}$$

where α_i and α_r are constants, λ_i and ζ_i denote the ith eigenvalue and its corresponding damping ratio, and $\gamma[1] = 1$.

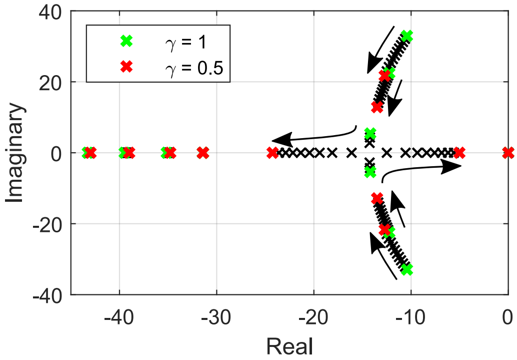

Fig. 5. Eigenvalues of the MG, when γ is reduced. The arrows indicate the direction of decreasing γ. (green) $\gamma = 1$ and (red) $\gamma = 0.5$.

The constants α_i and α_r are respectively larger than and less than unity. Hence, if any mode is located outside the allowed region, γ is reduced by α_r. On the other hand, if all modes are in the damped region, γ is increased by α_i. Otherwise, γ retains its previous value. It should also be noted that γ is bounded according to (4). The upper bound is included to limit the maximum droop, while the lower bound is implicitly ensured in (5).

The effect of the proposed controller on the droop characteristic and system eigenvalues can be seen in Fig. 4 and Fig. 5, respectively. The MG parameters can be found in Section V. Fig. 4 shows that the slope of the droop reduces for smaller values of γ. Thus, for a given value of active power, smaller values of γ lead to smaller steady-state frequency deviations. Secondly, the effect of reducing γ on the small-signal stability can be seen in the root locus diagram in Fig. 5. Only the dominant low-frequency modes are shown here, as these modes are more affected by changes in the droop gains, while high-frequency ones rely more on the parameters of internal controllers. For $\gamma = 1$, there are three pairs of complex conjugate eigenvalues and another six real eigenvalues, including one in the origin. When γ is reduced, the modes placed on the real axis are almost unaffected, while the damping ratios of the complex conjugate eigenvalues significantly increase. Hence, low damping factors result for large values of γ. Therefore, α_i should not be much larger than unity so that the dominant modes are not placed outside the allowed region.

The proposed control displayed in Fig. 3 is performed repeatedly, to ensure that the system is operating with sufficient stability margins. From a stability point of view, the droop gains should be updated as fast as possible so that the MG maintains satisfactory stability margins. However, the multitone current injection needed for the system identification increases the harmonic distortion of the MG. In this regard, the proposed control should be performed seldom to limit the adverse power quality effects. Naturally, the dynamics of the proposed controller should also be significantly slower than that of primary control loops to ensure sufficient time-scale separation. Based on this, γ is updated every 10 s in this work.

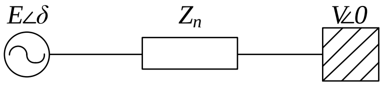

Fig. 6. DG modelled as a voltage source connected to an infinite bus.

Note that the effective droop gain is modified by the same factor (γ) for all DGs. The droop gain of a DG is normally set inversely proportional to the rating of the DG. This ensures proportional power sharing between the DGs according to their rating [3]. Since γ is the same for all DGs, the ratio between the effective droop gains of different DGs are unaffected by the proposed control. Hence, the proposed method does not affect the power sharing between DG units, even if the original droop gains differ between DGs.

B. Stability Analysis of the Proposed Controller

In order to analyze the stability properties of the proposed control technique, consider a single DG unit connected to a stiff grid via a line impedance $Z_n = R_n + jX_n$ as shown in Fig. 6. The DG unit is modelled as an ideal voltage source. The dynamics of internal current and voltage control loops are neglected. Therefore, the reference voltage is taken directly from the droop controller. The active and reactive power injected to the grid can be calculated as follows [37]:

$$P_m = (V/|Z_n|^2)\left[R_n(E\cos\delta - V) + X_n E\sin\delta\right] \tag{6}$$

$$Q_m = (V/|Z_n|^2)\left[X_n(E\cos\delta - V) - R_n E\sin\delta\right]. \tag{7}$$

In order to obtain the dynamic equation that governs the power flow, the power flow equations (6)-(7), the voltage droop equations (1)-(2) and the proposed frequency droop equation (4) are merged. Since the angle difference between the voltage sources is small, it will be assumed that $\delta \approx 0$. Then, $\sin\delta \approx 0$ and $\cos\delta \approx 1$. Derivations can also be done for $\sin\delta \approx \delta$ instead of $\sin\delta \approx 0$, with similar conclusions. However, the results will be presented for $\sin\delta \approx 0$ since this gives more compact expressions. The operating point of the DG voltage will be denoted E_0. Taking into account all the considerations above, the characteristic polynomial is:

$$s^3 + a_2 s^2 + a_1 s + a_0 = 0, \tag{8}$$

where

$$a_2 = \frac{2}{T_f} + \frac{n_q V X_n}{T_f |Z_n|^2} \tag{9}$$

$$a_1 = \frac{1}{T_f^2} + \frac{n_q V X_n}{T_f^2 |Z_n|^2} + \gamma\frac{m_p V E_0 X_n}{T_f |Z_n|^2} \tag{10}$$

$$a_0 = \gamma\frac{m_p V E_0}{T_f^2 |Z_n|^2}\left(X_n + n_q V\right). \tag{11}$$

To analyze the stability of the proposed control, the system can be assumed to be initially stable with $\gamma = \gamma_0$. According to Routh-Hurwitz criterion, $a_2 > 0$, $a_0 > 0$ and $a_2 a_1 > a_0$ are sufficient and necessary conditions to guarantee the system stability. Hence, these inequalities hold by assumption for the initial operating point. Thus, to verify that the proposed control is viable, the effect of reducing and increasing γ must be considered. Clearly, since a_2 is independent of γ, $a_2 > 0$ for any value of γ. Moreover, $a_0 > 0$ is always fulfilled for $\gamma > 0$. Finally, the effect of changing γ must be considered for the condition $a_2 a_1 > a_0$.

Consider first the effect of reducing γ. Equations (9)-(11) can be rewritten as follows:

$$a_2 = c_{21}, \;\; a_1 = c_{11} + \gamma c_{12}, \;\; a_0 = \gamma c_{01}, \tag{12}$$

where the constants c_{21}, c_{11}, c_{12} and c_{01} can be identified from the original expressions. Clearly, these coefficients are positive. After these considerations, the expression $a_2 a_1 > a_0$ can be divided by γ such that it can rewritten as follows:

$$(c_{21}c_{11})/\gamma + c_{21}c_{12} > c_{01}. \tag{13}$$

As reducing γ increases the left-hand side of (13), it is evident that the condition is fulfilled for $0 < \gamma < \gamma_0$. Hence, by Routh-Hurwitz criterion, the new operating point is stable for any reduction as long as $\gamma > 0$.

Meanwhile, increasing γ reduces the left-hand side of (13). By re-arranging (13), the stability condition for increasing γ is given by:

$$\gamma < c_{21}c_{11}/(c_{01} - c_{21}c_{12}), \tag{14}$$

where $c_{01} - c_{21}c_{12} > 0$ has been assumed in the derivation. Hence, γ is limited to the range $0 < \gamma < c_{21}c_{11}/(c_{01} - c_{21}c_{12})$ to ensure system stability. If the denominator in (14) is negative, γ is lower bounded by this value. In this case, the model predicts that the system is stable for arbitrarily large values of γ. This is clearly wrong. The reason why the model fails in estimating the exact stability limit is extensively discussed in [6]. However, the same authors point out that the model has adequate accuracy when the system is not close to the stability limit. Since the proposed method aims at operating the MG far from the stability limit, this model is considered sufficient in this work.

A more accurate limit for γ can be found by using the high-fidelity model proposed in [6]. There, an estimate of the upper bound on the active power droop gain is given in p.u. by:

$$k_p < S_n \frac{(R^2 + X^2)^2}{2RX^2}, \tag{15}$$

where k_p is the p.u. droop gain, S_n is the inverter rating with respect to its base power, while R and X are the p.u. resistance and reactance. For simplicity, S_n can be set to 1 here. In deriving (15), the voltage magnitudes are assumed to be close to unity [6]. In this work, the active power droop gain is given by γm_p. By using the nominal frequency as the base value, an estimate of the upper bound on γ is thus given by:

$$\gamma < \frac{\omega_0 (R^2 + X^2)^2}{2 m_p R X^2}. \tag{16}$$

Thus, an upper limit on γ is given by the lowest value of (14) and (16).

IV. MODE IDENTIFICATION

In this section, an outline of the apparent impedance analysis and matrix fitting are presented. These techniques will be used for identifying the system modes.

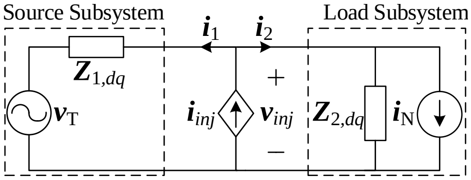

Fig. 7. Generic three phase power system with shunt current injection.

A. Apparent Impedance Analysis

The apparent impedance analysis is a small-signal method derived from impedance estimation techniques. The method was first proposed in [33]. Fig. 7 shows an electrical diagram that will be used to explain it, in which a generic three-phase power system is divided into two subsystems. The subsystems are represented by their Thevenin and Norton equivalents in an SRF. In the following, the Thevenin and Norton sources are disregarded due to the small-signal assumption. By injecting a shunt current disturbance $\boldsymbol{i}_{inj}$ at the interconnection point of the subsystems, the entire system is perturbed. At this point, the conventional impedance estimation technique can be used to estimate the subsystem small-signal impedances ($\boldsymbol{Z}_{1,dq}$ and $\boldsymbol{Z}_{2,dq}$), which are defined as follows:

$$\begin{aligned}\boldsymbol{V}_{inj} &= \boldsymbol{Z}_{1,dq}\boldsymbol{I}_1 \\ \boldsymbol{V}_{inj} &= \boldsymbol{Z}_{2,dq}\boldsymbol{I}_2.\end{aligned} \tag{17}$$

In (17), uppercase variables denote that voltages and currents are in the Laplace domain, while the subscript dq emphasizes that the impedances represent 2×2 impedance matrices, in an SRF. Based on the resulting equivalent impedances, the Generalized Nyquist Criterion can be applied to analyze the stability of the entire system [29].

Contrary to the conventional impedance estimation, the apparent impedance analysis is directly estimating the small-signal impedance $\boldsymbol{Z}_{a,dq}$ seen from the point of injection:

$$\boldsymbol{V}_{inj} = \boldsymbol{Z}_{a,dq}\boldsymbol{I}_{inj}, \tag{18}$$

where $\boldsymbol{Z}_{a,dq}$ is the parallel connection of $\boldsymbol{Z}_{1,dq}$ and $\boldsymbol{Z}_{2,dq}$. The advantage of the apparent impedance is that it represents a closed-loop transfer function of the system.

The relation between the poles of the impedance transfer function and the state-space representation of the full system can be obtained by writing a state-space representation of the system in the following way [33]:

$$sx = Ax + B\boldsymbol{i}_{\text{inj}} \tag{19}$$

$$\boldsymbol{v}_{\text{inj}} = Cx + D\boldsymbol{i}_{\text{inj}} + Es\boldsymbol{i}_{\text{inj}}, \tag{20}$$

where the input and output are $\boldsymbol{i}_{\text{inj}} = [i_{inj,d},\ i_{inj,q}]^T$ and $\boldsymbol{v}_{\text{inj}} = [v_{inj,d},\ v_{inj,q}]^T$, respectively. The state matrix A has dimension $n \times n$, the input matrix B has dimension $n \times 2$, the output matrix C has dimension $2 \times n$, while the matrices D and E have dimensions 2×2. By combining (19) and (20), and comparing to (18), the apparent impedance is given by:

$$\boldsymbol{Z}_{a,dq} = C(sI - A)^{-1}B + D + sE. \tag{21}$$

Therefore, it is clear that the poles of the apparent impedance match with the eigenvalues of the full system. This means that the apparent impedance contains all the information regarding observable modes seen from the point of injection [33].

A non-parametric estimate of the apparent impedance can be found by performing a frequency sweep, in which two linearly independent injections are performed [34]. For each frequency in the frequency sweep, the apparent impedance is then calculated by:

$$\boldsymbol{Z}_{a,dq} = \begin{bmatrix} V_{inj1,d} & V_{inj2,d} \\ V_{inj1,q} & V_{inj2,q} \end{bmatrix} \begin{bmatrix} I_{inj1,d} & I_{inj2,d} \\ I_{inj1,q} & I_{inj2,q}. \end{bmatrix}^{-1}, \tag{22}$$

where the subscripts $inj1$ and $inj2$ refer to the first and second injections, respectively. Note that it is important to perform the frequency sweep in the frequency range where the low-frequency modes reside. This is because the accuracy of the matrix fitting technique is only guaranteed in the frequency range of the measured response [38].

The apparent impedance is a small-signal relation between voltages and currents. Therefore, it must be estimated by using a consistent steady-state operating point. However, in practical applications, variations in the operating point occur frequently. In this work, a multi-tone current injection is chosen to perturb the system so that all the desired frequencies are disturbed simultaneously. This allows the identification process to be carried out rapidly and variations in the operating point will become insignificant.

B. Mode Identification Using Matrix Fitting

Once the non-parametric apparent impedance is obtained, the system modes can be obtained by using system identification methods. In this work, the system modes are obtained using a mathematical technique called matrix fitting, which is the multi-input multi-output version of vector fitting [33, 38–40]. It enables fitting frequency responses to rational function approximations, using poles and residues. The method is briefly described here.

First, the rational function approximation of the matrix transfer function $\boldsymbol{Z}_{a,dq}$ is given by:

$$\boldsymbol{Z}_{a,dq} \approx \sum_{i=1}^{n} \frac{\boldsymbol{R}_i}{s - \lambda_i} + \boldsymbol{D} + s\boldsymbol{E} \tag{23}$$

where $\boldsymbol{R}_i$ are the ith residue matrix corresponding to the eigenvalue λ_i. The poles, residues and matrices $\boldsymbol{D}$ and $\boldsymbol{E}$ need to be estimated. To this end, the set of frequency response points identified from the apparent impedance in (22) are used. First, the poles of a simplified version of the system are identified. This gives an overdetermined linear problem that can be solved by using the method of least squares [38]:

$$\hat{A}\hat{x} = \hat{B}, \tag{24}$$

where $\hat{x}$ includes the estimated parameters, while $\hat{A}$ and $\hat{B}$ are matrices that can be derived from the model structure and the measurements. After this first identification, a second step is carried out, in which the approximation is improved. This step is controlled by the magnitude of the residues, which play an important role in the accuracy of the identification (this will be discussed later). For more details, see [38].

In addition to the data input, only the order of the identified model has to be specified. Since mode identification using apparent impedance analysis is a black box technique, the actual order of the system is generally unknown. Three elements should be considered for choosing the system order:

1) The order must be less than the number of frequency injections. Hence, this also gives a lower bound for the number of frequency injections.
2) The system eigenvalues should be estimated with an adequate level of accuracy.
3) The order should be selected small enough, such that all eigenvalues are significant.

The first point can be easily addressed by selecting the number of tones in the injected signal. The second point requires a validation by using simulation and experimental results, which will be given in Sections V-1) and VI-B1). Finally, the third point requires an adequate method to discern whether the identified modes are significant. This can be ensured by reducing the model order until the 2-norm of the residue divided by the eigenvalue is larger than a constant [33, 38]. In particular, the following criterion has been used in this work:

$$\|\boldsymbol{R}_i\|_2/|\lambda_i| \geq 10^{-4}, \tag{25}$$

where $\boldsymbol{R}_i$ and λ_i denote the ith residue-matrix and eigenvalue, respectively. For further details regarding the matrix fitting technique applied to power electronics converters, see [33].

In most practical applications, not all system eigenvalues will be identified since the order of the identified system is limited by the number of frequency injections and the criterion in (25). However, as long as the modes are observable from the point of injection, the matrix fitting technique will be able to identify the least damped modes. This occurs because the technique finds a least squares approximation of the response and minimizes the rms error. Since complex conjugate poles will give a well-observable resonance peak in the measured frequency response, the technique will estimate these poles with high accuracy. Otherwise, the rms error would become substantial. On the other hand, real poles might not be estimated with the same degree of accuracy since the contribution from such poles can be less visible in the response. In other words, a smooth response can be fitted quite accurately with alternative choices of real poles.

V. SIMULATION RESULTS

In this section, the theoretical results are validated by using a detailed simulation model of the system depicted in Fig. 1. The model was developed by using Simulink and SimPowerSystems, and it includes all the details of power electronics converters. The initial network configuration is given in Table I. The simulation time step was set to 1 µs.

1) Validation of the Matrix Fitting Technique: For the matrix identification, 20 logarithmically-spaced tones were used in the range $[2, 200]$ Hz. The length of the interval for performing the fast Fourier transform (FFT) was 2 s. The tones and the FFT interval were rounded based on the actual MG frequency so that the spectral leakage was minimized [41]. The amplitude of each tone was 10^{-3} p.u.

TABLE I
SIMULATION PARAMETERS FOR THE SYSTEM UNDER STUDY

Parameter	Value	Parameter	Value
V_{dc}	800 V	L_f	1.4 mH
V_{LL}	400 V	R_f	0.1 Ω
f_0	50 Hz	C_f	50 µF
f_{sw}	8 kHz	L_o	0.35 mH
m_p	1e-4 rad/s/W	R_o	0.03 Ω
n_q	1e-4 V/VAr	Z_{12}	0.45 + j0.25 Ω
T_f	0.0318 s	Z_{23}	0.27 + j0.15 Ω
k_{pv}, k_{iv}	0.05, 390	Z_{34}	0.36 + j0.2 Ω
k_{pi}, k_{ii}	10.5, 16000	Z_{L1}	25 + j1 Ω
k_{ffi}	0	Z_{L2}	25.7 + j4.3 Ω
k_{ffv}	0.75	Z_{L3}	25.7 + j4.3 Ω
ζ_-, ζ_+	0.35, 0.9	ω_{lim}	100 rad/s

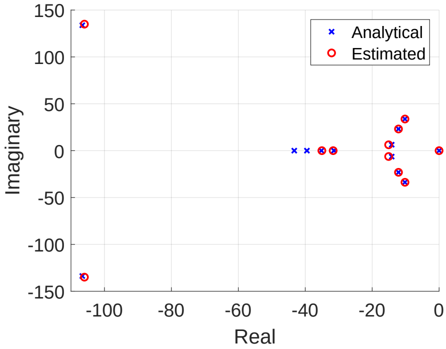

Fig. 8. System eigenvalues calculated analytically (x-marks) and estimated (circles) by using apparent impedance and matrix fitting, in simulation.

Fig. 8 shows a comparison between the analytical and estimated eigenvalues for the initial operating point. The mode in the origin and the three dominant complex pairs of eigenvalues are estimated accurately. However, there is a small mismatch in the real value for the pair of eigenvalues that have the smallest real value. This is consistent with the discussion in Section IV-B, where it is explained that the least damped modes are estimated with the highest accuracy. Clearly, two of the real eigenvalues have not been identified. This occurs due to the limited frequency injections (that limit the order of the system), as well as the criteria for the significance of the eigenvalues presented in (25).

2) Effect of Reduced Line Impedances: In this test, the effect of changes in line impedances will be studied. In this case, only DGs 1, 3 and 4 remain connected. The dominant identified eigenvalues for this operating point are shown as dark blue circles in Fig. 9 (top), while x-marks correspond to analytical eigenvalues. Clearly, all eigenvalues are within the allowed region. Moreover, the match between the analytical and identified results is adequate for the pair of complex conjugate eigenvalues with the largest real value, whereas there is a small mismatch in the real value of the second most dominant pair of complex eigenvalues.

Now, the line impedances Z_{12}, Z_{23} and Z_{34} are reduced by a factor of 0.8. This variation tries to replicate the effect of ambient temperature and light load conditions. The corresponding identified eigenvalues are presented as light blue circles in

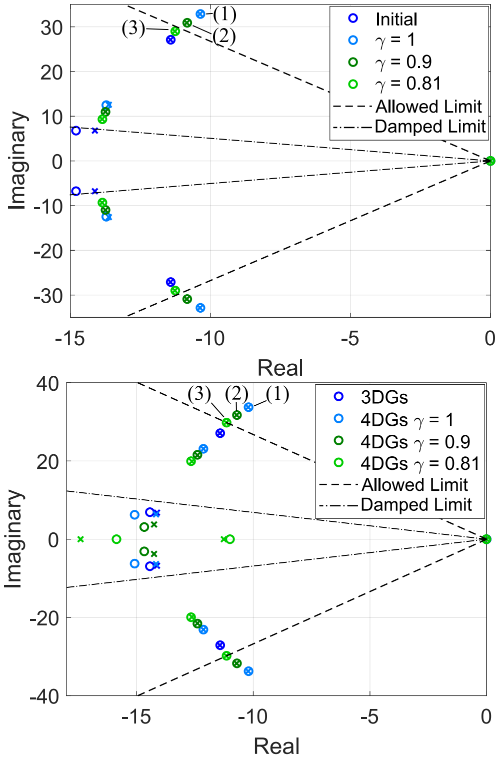

Fig. 9. Position of the dominant eigenvalues as a result of (top) reducing the line impedances and (bottom) connecting an additional DG unit, with the proposed controller. The (circles) are estimated eigenvalues and the (x-marks) are analytical eigenvalues.

Fig. 9 (top). One complex pair of eigenvalues (1) now lie outside the allowed region. Therefore, the proposed controller should be enabled. It can be seen that the match between the identified and analytical pairs of eigenvalues is adequate. When the controller is enabled, the active power droop gain is effectively reduced by a factor of $\alpha_r = 0.9$. Now, γ is reduced until the system modes are inside the allowed region. The resulting identified eigenvalues are shown by the dark and bright green circles in Fig. 9 (top). Reducing γ to 0.9 improved the damping ratio of the eigenvalues, but the complex pair of eigenvalues represented by (2) was still outside the allowed region. It was observed that reducing γ to 0.81 resulted in the desired damping ratio, as the most dominant complex pair of eigenvalues (3) is inside the allowed region. Also, it can be seen that analytical and simulation results matched.

3) Effect of Connecting an Additional DG: This case study considers the effects of adding an additional DG unit. This represents a realistic scenario in future MGs, where DGs might be connected or disconnected depending on the availability of renewable energy sources. The initial operating point is given by the dark blue circles in Fig. 9 (bottom), whereas the x-marks represent the corresponding analytical eigenvalues. The dominant eigenvalues are all inside the allowed region.

Now, DG2 is connected to the system. The corresponding identified eigenvalues are displayed as light blue circles in Fig. 9 (bottom). As expected, the inclusion of DG2 leads to an additional pair of complex conjugate eigenvalues. The two pairs of complex conjugate eigenvalues with largest real value are estimated accurately, whereas the third pair has a slight mismatch in the real value. Since the damping ratio of the pair of complex eigenvalues with the largest real value (1) is less than the allowed limit, the centralized controller reduces γ. The new identified eigenvalues corresponding to reduced droop gain can be seen in Fig. 9 (bottom) as dark green circles. Clearly, the dominant complex eigenvalues (2) are still outside the allowed region, leading to another reduction of γ to 0.81. In this operating point, also the complex pair of eigenvalues with the smallest damping ratio (3) are within the allowed region, leading to no further reduction in γ. For the last two operating points, the two dominant complex pairs of eigenvalues are identified accurately. The two remaining eigenvalues are also estimated accurately, although there is a slight mismatch. This happens in the final operating point since the effective reduction in the active power droop gain eliminated the imaginary part of these eigenvalues.

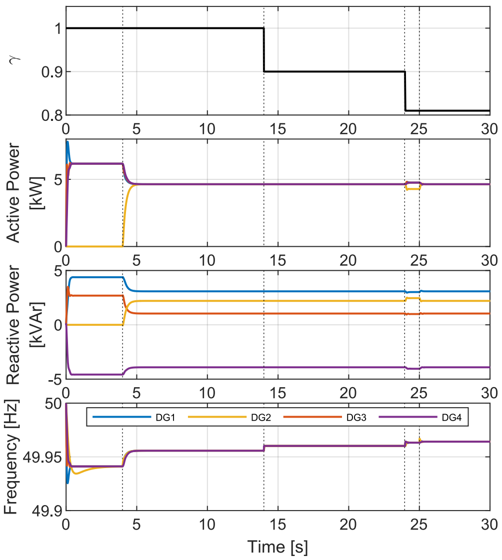

Fig. 10. Value of γ, active and reactive power, and frequency, for (blue) DG1, (yellow) DG2, (orange) DG3 and (purple) DG4, when DG2 is connected.

4) Effect of Time Delay in Updating γ: In order to evaluate the impact of delays in the communication link, a simulation with additional communication delays was conducted. Fig. 10 displays γ, as well as the DGs frequencies, active and reactive powers. The identified dominant modes for the different steps in this case is shown in Fig. 9. Up until $t = 4$ s, only three DGs were connected to the MG, and the active power was equally shared between them. Meanwhile, the reactive power delivered by each DG is different, due to the different line impedance values [42]. This problem can be addressed by sending reactive power commands to each DG. However, this issue will not be explained here for the sake of conciseness. Then, DG2 is connected to the MG and the active power is redistributed

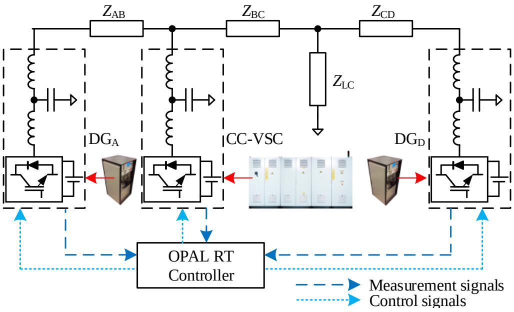

Fig. 11. Electrical diagram of the experimental set-up, including hardware elements and the control platform.

equally between the DGs. At $t = 14$ s, γ is reduced for all DGs at the same time. Both the active and reactive power sharing remain unaffected. Meanwhile, the system frequency increases due to the reduction in the effective droop gain. For the reduction in γ at $t = 24$ s, a delay of one second in updating γ was added for DG2. This results in a transient mismatch between the power delivered by DG2 and the other DGs. This happens because the effective droop gain of DG2 is larger during the transient. Once γ is updated for all the DGs, the active power is again shared equally. Due to the coupling of active and reactive powers, a small transient can be observed in the reactive power of the DGs. Meanwhile, the system frequency increases as a result of increasing γ, and it increases further when γ is the same for all DGs.

VI. EXPERIMENTAL VALIDATION

A. Description of Laboratory Setup

Fig. 11 shows a single line diagram of the experimental setup. The nominal phase-to-phase grid voltage was 350 V and the nominal frequency was 50 Hz. Two DGs were implemented with two 60 kVA converters. The switching and sampling frequencies were 10 kHz. The CC-VSC was implemented in an EGSTON 200 kVA COMPISIO system unit. Electrical lines were emulated by using external impedances, while banks of resistances were used as loads. The main controllers of the DGs and the CC-VSC were implemented in Simulink and executed on an OP5600 real-time simulator by OPAL-RT. All converters were operated from the same computer, where the centralized controller was executed. Electrical measurements were captured with a Tektronix MSO3014.

B. Experimental Results

1) Validation of Analytical Model: The accuracy of the analytical small-signal model is analyzed in this section. To this end, a power step of 5.3 kW was applied to the load Z_{LC}. Fig. 12 shows the output powers and the dq-components of the DGs output voltages when the load was connected. The d-axis voltages of the DGs experienced an initial dip before returning to the new steady state voltage levels. Also, the q-axis component of the voltages returns to zero in steady state, since each DG is synchronized with its own reference frame. It can be seen that the model is able to capture the low-frequency dynamics of the system. However, the model is not able to capture the high-frequency ripple generated by the switching devices since these effects were not included in the model.

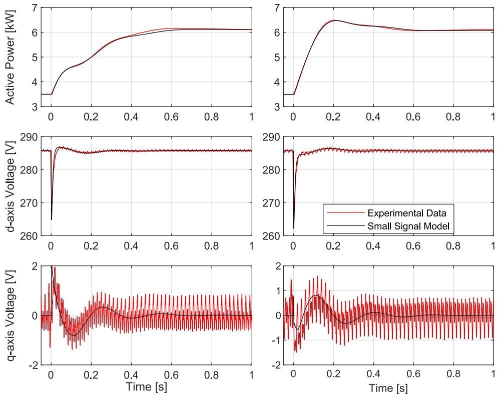

Fig. 12. Response of $\mathrm{DG_A}$ and $\mathrm{DG_D}$ to a step in the load. (left) $\mathrm{DG_A}$ and (right) $\mathrm{DG_D}$. (top) Active power, (middle) d-axis DG output voltage and (bottom) q-axis DG output voltage. (black) Small-signal and (red) experimental data.

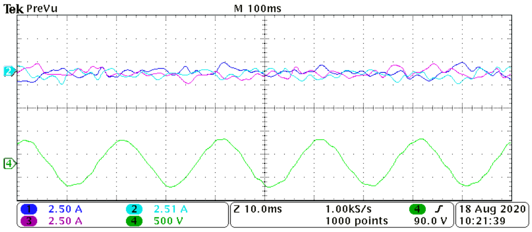

Fig. 13. Oscilloscope capture of (top) current injected by the CC-VSC and (bottom) MG voltage (phase-to-phase), during the multi-tone current injection.

2) Identification of Dominant Eigenvalues: A multi-tone current injection with ten tones in the range $[2, 200]$ Hz was used for estimating the apparent impedance. The phase of each tone was precalculated so that their amplitude was not excessive. Fig. 13 shows a snapshot of the multi-tone current injection and the resulting voltage at the point of injection. The total harmonic distortion (THD) of the MG voltage before the current injection was 0.8 %, while it was 0.96 % when the MG was being disturbed. Clearly, the level of accuracy of the identification depends on the amplitude of the disturbance. The voltage disturbance required to identify the model of the MG under study is within common limits established in power quality standards (e.g. IEEE 519 [43]), where the typical limit for the voltage THD is 5 %.

The identified and analytical eigenvalues are shown in Fig. 14. The two complex pairs of eigenvalues are estimated with adequate accuracy. Meanwhile, the eigenvalues on the real axis are not identified by the method. This can partly be explained by the order of the identified system, which was set to 6 in order to comply with (25).

3) Performance of the Centralized Controller: Fig. 15 shows the transients of frequencies and powers when the proposed adaptive controller is enabled. After detecting system

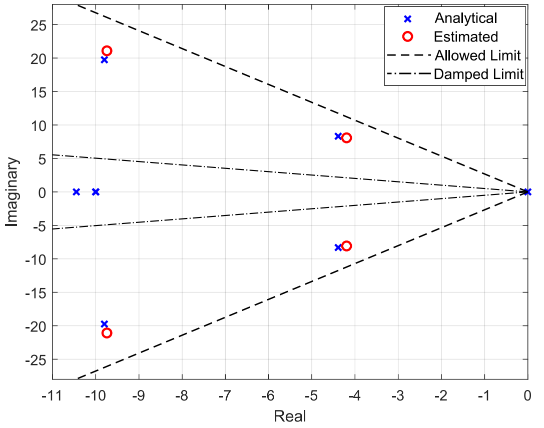

Fig. 14. Identification of the system eigenvalues by using experimental results. (x-marks) Analytical and (circles) identified eigenvalues.

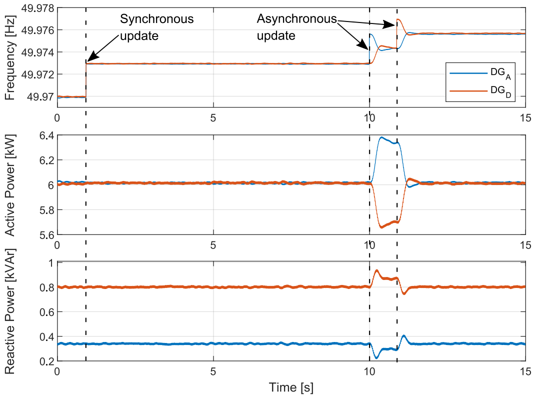

Fig. 15. Transient responses when the proposed controller is enabled, for (blue) $\mathrm{DG_A}$ and (red) $\mathrm{DG_D}$. (top) DGs frequencies, (middle) active and (bottom) reactive power.

eigenvalues outside the allowed region, γ is reduced at instants $t = 1$ s and $t = 10$ s. At $t = 1$ s, γ is reduced simultaneously for both DGs. This results in a step change in the frequency for both DGs. The system is stable and the transient effects in active and reactive power are almost undetectable. To illustrate the effect of updating γ at different times for the two DGs, γ is only reduced for $\mathrm{DG_A}$ at $t = 10$ s. This gives the same initial step-like response for $\mathrm{DG_A}$, before a new steady state frequency is obtained. Meanwhile, a transient is observed for the active and reactive powers. Now, the active power is not shared equally between the two DGs due to the different effective active power droop gains. The mismatch in reactive power slightly increased. At $t = 11$ s, γ is also updated for $\mathrm{DG_D}$. This gives a step change in the frequency for $\mathrm{DG_D}$ before a new steady state frequency is reached. It can also be seen that the active power sharing is restored. In practical applications, ramp rates over the updated droop coefficients could be applied in order to limit undesired transients resulting from asynchronous update of γ. However, this was not included here for simplicity.

VII. DISCUSSION

Since the proposed method depends on low-bandwidth communication, it is in place to discuss the effect of communication breakdown. Clearly, the proposed method will not work as intended if the communication breaks down, since γ is not updated. In this case, all DGs will retain their previous value of γ. However, it should be noted that the proposed method can be considered a supplement to the conventional droop control. Hence, the MG will maintain the basic functionalities, but the proposed method cannot improve the performance or stability margins. If the communication is restored, the proposed method will function properly again.

The proposed method also depends on the identification of the apparent impedance. Thus, if the CC-VSC is disconnected, γ will not be updated in the DGs. Again, the MG will still work as the proposed method is a supplement to the conventional droop control. However, the system stability margins cannot be adjusted. Another DG could perform the multitone injection needed to find the apparent impedance, given that it has sufficient control bandwidth. If this DG unit is performing any other function during the identification, it would affect stability. Meanwhile, the developments of this paper assume that the CC-VSC (that now is one of the DGs) does not affect stability. Therefore, the method proposed in this paper can be improved if this issue is taken into consideration in the problem formulation. This is of interest for further research.

VIII. CONCLUSION

In this paper, a centralized controller that improves the stability of an MG consisting of several DGs has been proposed. This controller recursively modifies the droop coefficient of DGs and guarantees that the system eigenvalues lie inside an allowed region. System eigenvalues are estimated each time step by using apparent impedance analysis and the matrix fitting technique. Therefore, no previous information of the system topology or parameter values is required. A small-signal representation of the system was used as a benchmark for the system identification. The performance of the controller was analyzed theoretically, and by using simulation and experimental results.

The results have shown that the system eigenvalues were accurately identified by using the matrix fitting technique. It was shown that an adequate selection of the number of frequency injections in the perturbing signal and a criterion for discerning significant eigenvalues are of paramount importance for practical applications. Theoretical results have shown that the proposed controller is stable provided that 1) the value of the adaptive gain is adequately selected and 2) the sampling period of the controller is slow enough. The disconnection of one line and the addition of one DG were used as test cases. Even though the sampling period of the controller was slow, the controller was able to move back the system eigenvalues to the allowed region in a few control steps. Moreover, as the performance of the system did not rely on fast communication systems the benefits of droop control were retained.

REFERENCES

[1] D. E. Olivares, A. Mehrizi-Sani, A. H. Etemadi, C. A. Cañizares, R. Iravani, M. Kazerani, A. H. Hajimiragha, O. Gomis-Bellmunt, M. Saeedifard, R. Palma-Behnke, G. A. Jiménez-Estévez, and N. D. Hatziargyriou, "Trends in microgrid control," *IEEE Transactions on Smart Grid*, vol. 5, no. 4, pp. 1905–1919, 2014.

[2] T. Caldognetto, S. Buso, P. Tenti, and D. I. Brandao, "Power-based control of low-voltage microgrids," *IEEE Journal of Emerging and Selected Topics in Power Electronics*, vol. 3, no. 4, pp. 1056–1066, 2015.

[3] M. C. Chandorkar, D. M. Divan, and R. Adapa, "Control of parallel connected inverters in standalone ac supply systems," *IEEE Transactions on Industry Applications*, vol. 29, no. 1, pp. 136–143, 1993.

[4] H. P. Beck and R. Hesse, "Virtual synchronous machine," *2007 9th International Conference on Electrical Power Quality and Utilisation, EPQU*, 2007.

[5] N. Pogaku, M. Prodanović, and T. C. Green, "Modeling, analysis and testing of autonomous operation of an inverter-based microgrid," *IEEE Transactions on Power Electronics*, vol. 22, no. 2, pp. 613–625, 2007.

[6] P. Vorobev, P. H. Huang, M. A. Hosani, J. L. Kirtley, and K. Turitsyn, "High-fidelity model order reduction for microgrids stability assessment," *IEEE Transactions on Power Systems*, vol. 33, no. 1, pp. 874–887, 2018.

[7] J. M. Guerrero, L. G. Vicuña, J. Matas, M. Castilla, and J. Miret, "Output impedance design of parallel-connected UPS inverters with wireless load sharing control," *IEEE Transactions on Industrial Electronics*, vol. 52, no. 4, pp. 1126–1135, 2005.

[8] J. He, Y. W. Li, J. M. Guerrero, F. Blaabjerg, and J. C. Vasquez, "An Islanding Microgrid Power Sharing Approach Using Enhanced Virtual Impedance Control Scheme," *IEEE Transactions on Power Electronics*, vol. 28, no. 11, pp. 5272–5282, 2013.

[9] J. He, Y. W. Li, and F. Blaabjerg, "An Enhanced Islanding Microgrid Reactive Power, Imbalance Power, and Harmonic Power Sharing Scheme," *IEEE Transactions on Power Electronics*, vol. 30, no. 6, pp. 3389–3401, 2015.

[10] J. M. Guerrero, J. Matas, L. G. Vicuña, M. Castilla, and J. Miret, "Decentralized control for parallel operation of distributed generation inverters using resistive output impedance," *IEEE Transactions on Industrial Electronics*, vol. 54, no. 2, pp. 994–1004, 2007.

[11] K. De Brabandere, B. Bolsens, J. Van Den Keybus, A. Woyte, J. Driesen, and R. Belmans, "A voltage and frequency droop control method for parallel inverters," *IEEE Transactions on Power Electronics*, vol. 4, pp. 1107–1115, 2007.

[12] T. Wu, Z. Liu, J. Liu, S. Wang, and Z. You, "A Unified Virtual Power Decoupling Method for Droop-Controlled Parallel Inverters in Microgrids," *IEEE Transactions on Power Electronics*, vol. 31, no. 8, pp. 5587–5603, 2016.

[13] Y. Mohamed and E. F. El-Saadany, "Adaptive Decentralized Droop Controller to Preserve Power Sharing Stability of Paralleled Inverters in Distributed Generation Microgrids," *IEEE Transactions on Power Electronics*, vol. 23, no. 6, pp. 2806–2816, 2008.

[14] Y. Sun, X. Hou, J. Yang, H. Han, M. Su, and J. M. Guerrero, "New Perspectives on Droop Control in AC Microgrid," *IEEE Transactions on Industrial Electronics*, vol. 64, no. 7, pp. 5741–5745, 2017.

[15] J. M. Guerrero, J. C. Vasquez, J. Matas, L. G. De Vicuña, and M. Castilla, "Hierarchical control of droop-controlled AC and DC microgrids - A general approach toward standardization," *IEEE Transactions on Industrial Electronics*, vol. 58, no. 1, pp. 158–172, 2011.

[16] J. A. Lopes, C. L. Moreira, and A. G. Madureira, "Defining Control Strategies for Analysing MicroGrids Islanded Operation," *IEEE Transactions on Power Systems*, vol. 21, no. 2, pp. 916–924, 2006.

[17] J. M. Guerrero, M. Chandorkar, T. L. Lee, and P. C. Loh, "Advanced control architectures for intelligent microgridspart i: Decentralized and hierarchical control," *IEEE Transactions on Industrial Electronics*, vol. 60, no. 4, pp. 1254–1262, 2013.

[18] C. Ahumada, R. Cárdenas, D. Sáez, and J. M. Guerrero, "Secondary Control Strategies for Frequency Restoration in Islanded Microgrids With Consideration of Communication Delays," *IEEE Transactions on Smart Grid*, vol. 7, no. 3, pp. 1430–1441, 2016.

[19] M. Savaghebi, A. Jalilian, J. C. Vasquez, and J. M. Guerrero, "Secondary Control Scheme for Voltage Unbalance Compensation in an Islanded Droop-Controlled Microgrid," *IEEE Transactions on Smart Grid*, vol. 3, no. 2, pp. 1–12, 2012.

[20] A. Micallef, M. Apap, C. Spiteri-Staines, J. M. Guerrero, and J. C. Vasquez, "Reactive power sharing and voltage harmonic distortion compensation of droop controlled single phase islanded microgrids," *IEEE Transactions on Smart Grid*, vol. 5, no. 3, pp. 1149–1158, 2014.

[21] Q. Shafiee, J. M. Guerrero, and J. C. Vasquez, "Distributed secondary control for islanded microgrids-a novel approach," *IEEE Transactions on Power Electronics*, vol. 29, no. 2, pp. 1018–1031, 2014.

[22] Y. Zhang, L. Xie, and Q. Ding, "Interactive Control of Coupled Microgrids for Guaranteed System-Wide Small Signal Stability," *IEEE Transactions on Smart Grid*, vol. 7, no. 2, pp. 1088–1096, 2016.

[23] G. Agundis-Tinajero, N. L. D. Aldana, A. C. Luna, J. Segundo-Ramirez, N. Visairo-Cruz, J. M. Guerrero, and J. C. Vazquez, "Extended-Optimal-Power-Flow-Based Hierarchical Control for Islanded AC Microgrids," *IEEE Transactions on Power Electronics*, vol. 34, no. 1, pp. 840–848, 2019.

[24] Q. C. Zhong, "Power-Electronics-Enabled Autonomous Power Systems: Architecture and Technical Routes," *IEEE Transactions on Industrial Electronics*, vol. 64, no. 7, pp. 5907–5918, 2017.

[25] *Overhead electrical conductors - Calculation methods for stranded bare conductors*. IEC TR 61597:1995, 1995.

[26] P. H. Huang, P. Vorobev, M. Al Hosani, J. L. Kirtley, and K. Turitsyn, "Plug-and-Play Compliant Control for Inverter-Based Microgrids," *IEEE Transactions on Power Systems*, vol. 34, no. 4, pp. 2901–2913, 2019.

[27] Task Force on Identification of Electromechanical Modes, *Identification of Electromechanical Modes in Power Systems*. IEEE, 2012.

[28] D. J. Trudnowski and J. W. Pierre, "Overview of algorithms for estimating swing modes from measured responses," *2009 IEEE Power and Energy Society General Meeting, PES '09*, pp. 1–8, 2009.

[29] M. Belkhayat, "Stability criteria for AC power systems with regulated loads," Ph.D. dissertation, Purdue University, 1997.

[30] J. Sun, "Small-signal methods for AC distributed power systems-A review," *IEEE Transactions on Power Electronics*, vol. 24, no. 11, pp. 2545–2554, 2009.

[31] ——, "Impedance-based stability criterion for grid-connected inverters," *IEEE Transactions on Power Electronics*, vol. 26, no. 11, pp. 3075–3078, 2011.

[32] M. Amin and M. Molinas, "Small-Signal Stability Assessment of Power Electronics Based Power Systems : A Discussion of Impedance- And Eigenvalue-Based Methods," *IEEE Transactions on Industry Applications*, vol. 53, no. 5, pp. 5014–5030, 2017.

[33] A. Rygg and M. Molinas, "Apparent Impedance Analysis: A Small-Signal Method for Stability Analysis of Power Electronic-Based Systems," *IEEE Journal of Emerging and Selected Topics in Power Electronics*, vol. 5, no. 4, pp. 1474–1486, 2017.

[34] G. Francis, R. Burgos, D. Boroyevich, F. Wang, and K. Karimi, "An algorithm and implementation system for measuring impedance in the D-Q domain," *IEEE Energy Conversion Congress and Exposition: Energy Conversion Innovation for a Clean Energy Future, ECCE 2011, Proceedings*, pp. 3221–3228, 2011.

[35] M. Cespedes and J. Sun, "Adaptive control of grid-connected inverters based on online grid impedance measurements," *IEEE Transactions on Sustainable Energy*, vol. 5, no. 2, pp. 516–523, 2014.

[36] X. Chen, C. Gong, J. Chen, Y. Zhang, and S. Wang, "Impedance-Phased Dynamic Control Method for Grid-Connected Inverters in a Weak Grid," *IEEE Transactions on Power Electronics*, vol. 32, no. 1, pp. 274–283, 2017.

[37] P. Kundur, *Power system stability and control*. New York: McGraw-hill, 1994.

[38] B. Gustavsen and A. Semlyen, "Rational Approximation of Frequency Domain Responses By Vector Fitting," *IEEE Transactions on Power Delivery*, vol. 14, no. 3, pp. 1052–1061, 1999.

[39] B. Gustavsen, "Improving the pole relocating properties of vector fitting," *2006 IEEE Power Engineering Society General Meeting, PES*, vol. 21, no. 3, pp. 1587–1592, 2006.

[40] D. Deschrijver, M. Mrozowski, T. Dhaene, and D. De Zutter, "Macromodeling of Multiport Systems Using a Fast Implementation of the Vector Fitting Method," *IEEE Microwave and Wireless Components Letters*, vol. 18, no. 6, pp. 383–385, 2008.

[41] A. Rygg, "Impedance-based methods for small-signal analysis of systems dominated by power electronics," Ph.D. dissertation, Norwegian University of Science and Technology, 2018.

[42] Y. Han, H. Li, P. Shen, E. A. A. Coelho, and J. M. Guerrero, "Review of Active and Reactive Power Sharing Strategies in Hierarchical Controlled Microgrids," *IEEE Transactions on Power Electronics*, vol. 32, no. 3, pp. 2427–2451, 2017.

[43] *IEEE Recommended Practice and Requirements for Harmonic Control in Electric Power Systems*. IEEE Std. 519-2014, 2014.

Fredrik Göthner was born in Oslo, Norway, in 1992. He received the M.Sc. degree in electrical power engineering in 2017 from the Norwegian University of Science and Technology (NTNU), Trondheim, Norway, where he is currently working toward the Ph.D. degree on the control of converters in microgrids. His main research interests include control of power electronics and issues related to stability and power quality in microgrids.

Raymundo E. Torres-Olguin received the B.Sc. degree in electromechanical engineering from the University of San Luis Potosí, Mexico, in 2004, M.Sc. degree in control and dynamical systems from the Applied Mathematics Department, Research Institute of Science and Technology of San Luis Potosí (IPICYT), Mexico, in 2006, and Ph.D. degree in electric power engineering from the Norwegian University of Science and Technology (NTNU), Norway, in 2013. From 2012, he has worked as a research scientist in SINTEF Energy Research located in Trondheim, Norway. His main research interest includes control of power electronics for the integration of renewable resources, dc transmission and microgrids.

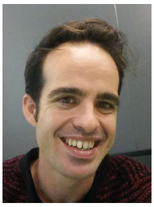

Javier Roldán-Pérez (S'12-M'14) received a B.S. degree in industrial engineering, a M.S. degree in electronics and control systems, a M.S. degree in system modeling, and a Ph.D. degree in power electronics, all from Comillas Pontifical University, Madrid, in 2009, 2010, 2011, and 2015, respectively. From 2010 to 2015, he was with the Institute for Research in Technology (IIT), Comillas University. In 2014, he was a visiting Ph.D. student at the Department of Energy Technology, Aalborg University, Denmark. From 2015 to 2016 he was with the Electric and Control Systems Department at Norvento Energía Distribuida. In September 2016 he joined the Electrical Systems Unit at IMDEA Energy Institute. In 2018, he did a research stay at SINTEF Energy Research, Trondheim. His research topics are the integration of renewable energies, microgrids, and power electronics applications.

Atle Rygg took his MSc in electrical engineering at Norwegian University of Science and Technology (NTNU) in 2011, and his PhD in engineering cybernetics at NTNU in 2018. He was employed at SINTEF Energy Research from 2011 to 2018, focusing on power electronics and power system dynamics. His PhD work was centered on stability analysis of power systems dominated by power electronics. From 2018 he is employed at Siemens Energy - Offshore Marine Center in Trondheim.

Ole-Morten Midtgård (M'03) was born in Tromsø, Norway, in 1967. He received the M.Sc. and Ph.D. degrees in Electric Power Engineering from the Norwegian University of Science and Technology (NTNU), Trondheim, Norway, in 1992 and 1997, respectively. He is currently Head of Department at NTNU's Department of Electric Power Engineering, where he has been a Professor since 2012. Previous employments include 5 years at ABB and 8 years tenure at the University of Agder, Grimstad, Norway. Prof. Midtgård is an elected member of the Norwegian Academy of Technological Sciences (NTVA) and of Agder Academy of Sciences and Letters. He has broad research interests, which in addition to power electronics include electromagnetic computations, and applications such as microgrids, integration of PV in smart grids, and electric aviation.

Paper II

The paper ”Reduced-Order Model of Distributed Generators with Internal Loops and Virtual Impedance” was accepted for publication in a future issue of *IEEE Transactions on Smart Grid* in October 2021.

Reduced-Order Model of Distributed Generators with Internal Loops and Virtual Impedance

Fredrik Göthner, Javier Roldán-Pérez, *Member, IEEE*, Raymundo E. Torres-Olguin, and Ole-Morten Midtgård, *Member, IEEE*

***Abstract*—Reduced-order converter models have attracted attention in microgrid applications for being less computationally expensive and simpler to analyze. However, most of the models already developed in the literature only include basic control loops, while control additions such as virtual impedances and the effect of internal control loops are typically neglected. Also, the frequency range in which these models are applicable has not been thoroughly studied. In this paper, a low-order reduced-order model of a droop-controlled converter that includes internal control loops and virtual impedances is derived. The validity of the assumptions used to reduce the model is analyzed and a criterion for deciding the frequency range in which the model can be used is proposed. Differences between transient and quasi-stationary virtual impedances are highlighted by using the proposed modelling method. In particular, it is analytically shown that quasi-stationary virtual impedances have a larger stability region compared to transient virtual impedances. Simulation and experimental results based on a 60 kVA converter are used to validate the main contributions of this work.**

***Index Terms*—AC/DC Converter Control, Reduced Order Model, Virtual Impedance, Droop Control.**

I. INTRODUCTION

THE massive deployment of distributed generators (DGs) and electrical storage devices has led to an increased interest in microgrids [1, 2]. When operating in grid-connected mode, DGs have traditionally been controlled to extract the maximum power [3]. However, with an increasing share of DGs, it is anticipated that these devices will participate in the regulation of the grid voltage and frequency. This is particularly the case for operation in island mode. As a consequence, a variety of control schemes for voltage-controlled DGs have been proposed, of which droop control is one of the most commonly used in the literature [4]. This method enables load sharing between units operating in parallel without using communication. However, it has been shown that the basic control scheme suffers from poor stability margins, particularly for large droop gains or small interconnecting lines [5, 6].

To address this issue and evaluate appropriate modifications to the original droop control, small-signal analysis of microgrids has been extensively used over the last two decades. A complete small-signal model of an MG was developed by Pogaku *et al.* [5], which has served as a benchmark for MG stability studies. This model accounts for droop-controlled DGs with internal cascaded voltage and current controllers, in addition to the dynamics of the network and loads. Although it accurately models the MG dynamics, the complexity of this model makes theoretical derivations inconvenient and limits computational speed for analyzing MGs consisting of several DGs. This has motivated the development of reduced-order models that aim at capturing the dominant low-frequency dynamics.

Inspired by small-signal modelling in power systems, the first works in this field neglected the network and inner controller dynamics [7, 8]. This was justified by the significantly larger bandwidth of the internal controllers and small timescales of the network dynamics. However, it was later realized that a dynamic network model was imperative to model the MG dynamics accurately, as their dynamics can significantly affect the low-frequency modes [5, 6]. Several reduced-order models have included the effect of the network dynamics [9–13]. These models have been obtained using different approaches, including phasor-based modelling [10, 13] and singular perturbation methods [11, 12]. This substantially improves the accuracy of the reduced-order models; however, these models still neglect the dynamics of the inner controllers. While this may be accurate in certain situations, the inner dynamics can significantly affect the low-frequency modes [14, 15]. In [14], the fast dynamics are approximated by using the frequency response of the DG. This method captures the interaction between the internal controllers, the low-frequency modes and the network dynamics. Even though the results are promising, the form of the model is not convenient for analytical derivations. In [15], the controller dynamics were similarly approximated in the frequency domain, resulting in a 5th-order DG model that produces accurate results. However, this model is not further reduced so its size is still large for analytical derivations.

In practical MG applications, additional control loops such as virtual impedances are commonly applied to guarantee an adequate system damping and transient performance [16–18]. This has led to a variety of virtual impedance implementations, among other things depending on the R/X ratio of the grid [19, 20]. The dynamic response of physical impedances has also been included in virtual impedance schemes to various degrees [18]. In this regard, quasi-stationary virtual impedances replicate the effect of an impedance in steady state, while transient virtual impedances additionally include a dynamic term. While virtual impedances are commonly applied in DG controllers, they have not commonly been included in reduced-order models. Notable exceptions from this are [13], which included an inductive virtual impedance with transient terms, [21], which designed virtual impedances to guarantee small-signal stability using a reduced-order model,

---

This work has been funded by CINELDI - Centre for intelligent electricity distribution, an 8-year Research Centre under the FME-scheme (Centre for Environment-friendly Energy Research, 257626/E20). The authors gratefully acknowledge the financial support from the Research Council of Norway and the CINELDI partners. The work of J. Roldán-Pérez received funds from the Spanish Government through Juan de la Cierva Incorporación program (IJC2019-042342-I).

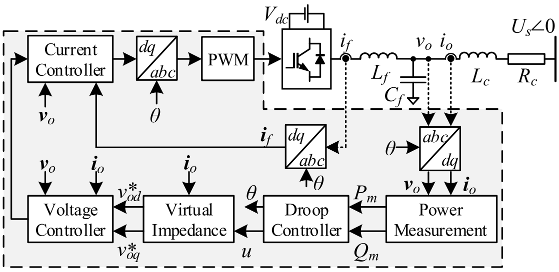

Fig. 1. The system under study with complete DG control structure.

and [22], which compares reduced-order models including virtual impedances. However, these models did not consider how virtual impedances are affected by the dynamics of inner control loops. Moreover, the differences between dynamic stability properties of different virtual impedance implementations were not studied.

In this paper, an accurate reduced-order DG model including the effects of converter internal dynamics and virtual impedances is developed. The main contributions can be summarized as follows:

1) An accurate reduced-order DG model including the effects of converter internal control loops and virtual impedances is developed.
2) The frequency range in which this model can be reduced to a 3rd-order one is studied, and a criterion for selecting an adequate model order is presented.
3) The differences between two different virtual impedance implementations are shown analytically. In particular, it is shown that including transient virtual impedances reduces the stability margin of the low-frequency modes.
4) The theoretical developments are verified in a 60 kVA droop-controlled converter connected to a grid emulator.

The rest of this paper is organized as follows. In Section II, an overview of the DG control and a simplification of the internal loops are given. The reduced-order model is presented in Section III, while a condition to select the order of the reduced-order model is presented in Section IV. Simulation and experimental results are presented in Sections V and VI. Conclusions are drawn in Section VIII.

II. SYSTEM AND MODELLING OVERVIEW

A. Overview of Droop Controlled DG

Fig. 1 shows the system under study. It consists of a droop-controlled DG connected to an ideal grid. An overview of a typical implementation of a DG control system in a synchronous reference frame (SRF) (dq) is also shown. The outer power loop uses conventional Pf and QV droops to enable parallel operation of DGs [4]:

$$\omega = \omega^* - m_p \frac{1}{1+\tau s} P_m, \quad u = U^* - n_q \frac{1}{1+\tau s} Q_m, \tag{1}$$

where ω is the DG frequency and u is the droop controller magnitude, superscript "*" stands for "reference", m_p and n_q are the active and reactive droop gains, τ is the low-pass filter time constant, s is the Laplace variable, while P_m and Q_m are the measured active and reactive powers. The inverter angle is obtained as $\theta = \int \omega dt$. The voltage reference calculated by the QV-droop controller is the input to the virtual impedance block, which modifies the voltage reference according to:

$$\begin{bmatrix} v_{od}^* \\ v_{oq}^* \end{bmatrix} = \begin{bmatrix} u \\ 0 \end{bmatrix} - \begin{bmatrix} R_v & -\omega^* L_v \\ \omega^* L_v & R_v \end{bmatrix} \begin{bmatrix} i_{od} \\ i_{oq} \end{bmatrix} - \frac{sL_v}{1+\tau_v s} \boldsymbol{I} \begin{bmatrix} i_{od} \\ i_{oq} \end{bmatrix}, \tag{2}$$

where R_v and L_v are the virtual resistance and inductance, respectively, τ_v is the time constant of the low-pass filter and $\boldsymbol{I}$ is the identity matrix. Electrical variables are marked in the figure and subscripts d and q refer to variables in the SRF. A low-pass filter is included in the transient term of the virtual impedance to limit amplification of high-frequency noise [18]. If this term is neglected, a quasi-stationary implementation of the virtual impedance is obtained. The voltage reference in (2) is tracked by the inner voltage controller while the inner current controller regulates the inverter-side current. These controllers are devised in the SRF and consist of PI regulators with feedforward and decoupling terms [5].

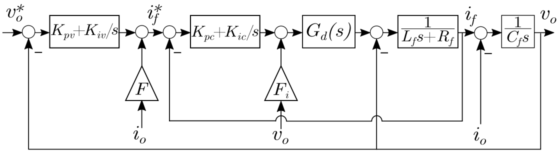

Fig. 2. Block diagram representing the dynamics of the dq axes of the output filter and the internal control loops.

B. Simplification of Internal Loops

Even though inner controllers are commonly designed to be faster than outer control loops, they can significantly affect the stability margins of the system. Hence, the inner dynamics should be properly accounted for in reduced-order models [14, 15].

If decoupling terms are used in inner controllers, it is common to assume that the dq axes dynamics are decoupled in the low-frequency range [23]. Then, the inner dynamics of both axes can be represented by the block diagram depicted in Fig. 2. The effectiveness of the decoupling terms in the frequency range of interest will be confirmed in the following paragraph. The outer voltage controller is represented as a PI regulator together with a feedforward of the output current i_o multiplied by the gain F. Similarly, the inner current controller is represented by a PI regulator and feedforward of the capacitor voltage v_o through the gain F_i. The voltage v_o can then be expressed by:

$$\begin{bmatrix} v_{od} \\ v_{oq} \end{bmatrix} = T_v(s) \boldsymbol{I} \begin{bmatrix} v_{od}^* \\ v_{oq}^* \end{bmatrix} - Z_o(s) \boldsymbol{I} \begin{bmatrix} i_{od} \\ i_{oq} \end{bmatrix}, \tag{3}$$

where T_v is the complementary sensitivity function and Z_o is the inner DG impedance. As the inner current loop is designed to have a significantly larger bandwidth than the outer voltage controller, it is reasonable to assume that $i_f \approx i_f^*$ at low frequencies [24]. The validity of this assumption can be studied by considering the bode plots in Fig. 3. The dashed lines show

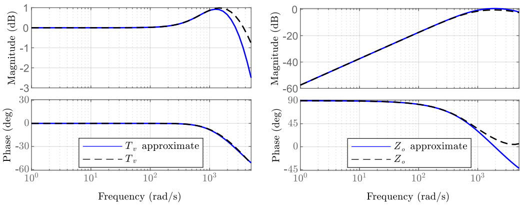

(a) (b)

Fig. 3. Frequency responses of T_v and Z_o with (blue) approximated and (black) complete current dynamics.

T_v and Z_o when the internal loops are included, while the solid lines display the same transfer functions when the internal loops are neglected. It can be seen that neglecting the inner current dynamics is an appropriate assumption for frequencies lower than about 1000 rad/s (approximately, 150 Hz). Hence, this assumption is justified in the low-frequency range. In this case, the transfer functions in (3) are given by:

$$T_v(s) = \frac{K_{pv}s + K_{iv}}{C_f s^2 + K_{pv}s + K_{iv}}, \tag{4a}$$

$$Z_o(s) = (1-F)\frac{s}{C_f s^2 + K_{pv}s + K_{iv}}. \tag{4b}$$

Here, T_v describes the voltage tracking capability of the converter and Z_o is its equivalent output impedance. If the feedforward gain is chosen as $F = 1$, the effect of the inner DG impedance is cancelled. However, in practical applications, F is chosen to be less than one in order to avoid stability problems.

In general, the bandwidth of the voltage controller is significantly larger than that of droop controllers. Hence, the transfer functions in (4) can be approximated at low frequencies as:

$$T_v \approx 1 \text{ and } Z_o \approx sL_o, \tag{5}$$

where $L_o = (1-F)K_{iv}^{-1}$.

Clearly, the inner DG impedance acts as an inductance at low frequencies. By further approximating the transient term in (2) as sL_v at low frequencies, the DG output voltage can be calculated by combining (2), (3) and (5):

$$\begin{bmatrix} v_{od} \\ v_{oq} \end{bmatrix} = \begin{bmatrix} u \\ 0 \end{bmatrix} - \begin{bmatrix} R_v & -\omega^* L_v \\ \omega^* L_v & R_v \end{bmatrix} \begin{bmatrix} i_{od} \\ i_{oq} \end{bmatrix} - s(L_o + L_v)\boldsymbol{I} \begin{bmatrix} i_{od} \\ i_{oq} \end{bmatrix}. \tag{6}$$

III. REDUCED-ORDER MODEL OF A DG

In this section, the method proposed in [13] is applied to reduce the model order of droop-controlled DGs. The effect of internal control loops and different virtual impedance implementations are added to the model in order to improve its accuracy.

A. Derivation of the Reduced-Order Model

By modelling the DG as a droop-controlled ideal voltage source in series with an impedance, it is possible to establish an accurate 5th-order model of the DG. Three states are then related to the DG, while two states represent the dynamics of the current phasor [10, 13]. According to (6), the effect of the virtual impedance, the internal controllers and the LC filter can be modelled by a controllable voltage source in series with an impedance. Thus, the DG terminal voltage can be modelled as $U\angle\delta$, while the impedance can be incorporated into the current dynamics. Taking the ideal grid as a reference, a 5th-order model can then be used to accurately model the low-frequency dynamics of the DG [13]:

$$\frac{d\delta}{dt} = \omega - \omega_0, \tag{7a}$$

$$\tau\frac{d\omega}{dt} = \omega^* - \omega - m_p P_m, \tag{7b}$$

$$\tau\frac{dU}{dt} = U^* - U - n_q Q_m, \tag{7c}$$

$$L_t\frac{dI_d}{dt} = U\cos\delta - U_s - R_{eq}I_d + X_{eq}I_q, \tag{7d}$$

$$L_t\frac{dI_q}{dt} = U\sin\delta - X_{eq}I_d - R_{eq}I_q, \tag{7e}$$

where an uppercase variable refers to the dynamic phasor of the signal (e.g., I_d is the dynamic phasor of i_{od}). The effect of real and virtual impedances, as well as the effect of internal loops, is considered in the values of $R_{eq} = R_c + R_v$, $X_{eq} = \omega_0 L_c + \omega^* L_v$ and $L_t = L_c + L_o + L_v$.

The conventional 3rd-order model is obtained by neglecting the network dynamics in (7), which corresponds to setting the derivatives of I_d and I_q to zero. Then, the currents are readily obtained from (7d) and (7e), which can be used to calculate P_m and Q_m. However, a significantly more accurate model can be obtained by using dynamic phasors. To this end, the current phasor can be written in the Laplace domain as:

$$I = \frac{Ue^{j\delta} - U_s}{R_{eq} + jX_{eq} + sL_t} = \frac{Ue^{j\delta} - U_s}{R_{eq} + jX_{eq}} \frac{1}{1 + \dfrac{sL_t}{R_{eq} + jX_{eq}}}. \tag{8}$$

As the goal here is to represent the low-frequency dynamics, it can be assumed that [13]:

$$\left| \frac{sL_t}{(R_{eq} + jX_{eq})} \right| \ll 1, \tag{9}$$

in order to simplify (8). In this case, (8) can be approximated by using its first-order Maclaurin series:

$$I \approx \frac{Ue^{j\delta} - U_s}{R_{eq} + jX_{eq}} \left(1 - \frac{sL_t}{R_{eq} + jX_{eq}} \right). \tag{10}$$

It can be noticed that a higher-order approximation of (8) is also possible. Very high-order approximations might result in a model order higher than the original one in (7), and therefore they are not recommended. However, it is possible to show that a second-order approximation can give additional terms to the model without increasing the model order. This is beyond the scope of this paper, but it is of interest for future research.

After returning to the time-domain, the complex power can be calculated as $S_m = (3/2)Ue^{j\delta}I^*$, giving:

$$S_m = \frac{3}{2}\left(\frac{U^2 - U_s U e^{j\delta}}{R_{eq} - jX_{eq}} - L_t \frac{U\dot{U} - j\dot{\delta}U^2}{(R_{eq} - jX_{eq})^2} \right). \tag{11}$$

Upon linearizing about a steady-state operating point (denoted by subscript 0) and assuming $\delta_0 \approx 0$ and $U_{s0} \approx U_0$, the

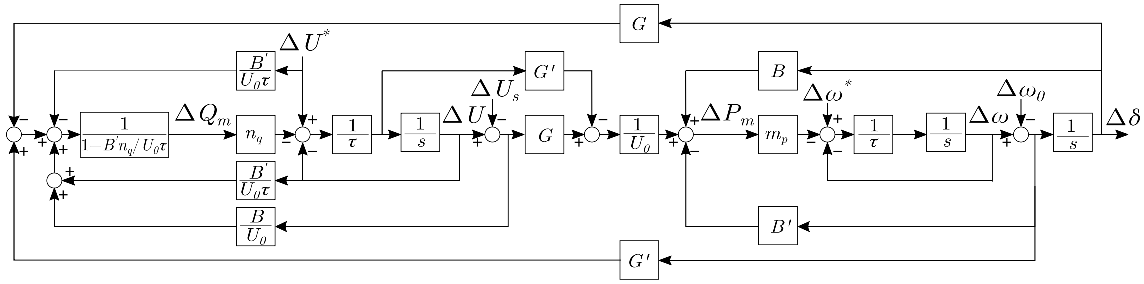

Fig. 4. Equivalent block diagram of the reduced-order model in (14).

measured small-signal active and reactive powers are given by:

$$\Delta P_m = B\Delta\delta - B'\Delta\omega + \frac{G}{U_0}\Delta U - \frac{G'}{U_0}\Delta\dot{U} - \frac{G}{U_0}\Delta U_s + B'\Delta\omega_0, \tag{12a}$$

$$\Delta Q_m = -G\Delta\delta + G'\Delta\omega + \frac{B}{U_0}\Delta U - \frac{B'}{U_0}\Delta\dot{U} - \frac{B}{U_0}\Delta U_s - G'\Delta\omega_0, \tag{12b}$$

where

$$B = \frac{3X_{eq}U_0^2}{2(R_{eq}^2 + X_{eq}^2)}, \quad G = \frac{3R_{eq}U_0^2}{2(R^2 + X_{eq}^2)}, \tag{13a}$$

$$B' = \frac{3L_t R_{eq} X_{eq} U_0^2}{(R_{eq}^2 + X_{eq}^2)^2}, \; G' = \frac{3L_t(R_{eq}^2 - X_{eq}^2)U_0^2}{2(R_{eq}^2 + X_{eq}^2)^2}. \tag{13b}$$

Note from (13b) that increasing the inner DG impedance or transient virtual impedance increases G' and B'. Meanwhile, increasing the quasi-stationary virtual impedances (R_{eq} or X_{eq}) reduces these terms.

The reduced-order model is obtained by linearizing (7a)-(7c), and combining these with (12). A block diagram of the resulting reduced-order model is shown in Fig. 4. The model can also be written in the following compact form (omitting the external inputs to the model):

$$\frac{\tau}{m_p}\Delta\ddot{\delta} + \left(\frac{1}{m_p} - B'\right)\Delta\dot{\delta} + B\Delta\delta + \frac{G}{U_0}\Delta\dot{U} - \frac{G'}{U_0}\Delta U = 0 \tag{14a}$$

$$\left(\frac{\tau}{n_q} - \frac{B'}{U_0}\right)\Delta\dot{U} + \left(\frac{1}{n_q} + \frac{B'}{U_0}\right)\Delta U - G\Delta\dot{\delta} + G'\Delta\delta = 0 \tag{14b}$$

B. Approximate Stability Boundaries

A simple estimate of the small-signal stability boundary is found by requiring positive coefficients in front of $\Delta\dot{\delta}$ and $\Delta\dot{U}$ in (14) [13]. In terms of the droop coefficients, this stability boundary is thus given by:

$$m_p < \frac{(R_{eq}^2 + X_{eq}^2)^2}{3L_t R_{eq} X_{eq} U_0^2}, \quad n_q < \frac{\tau(R_{eq}^2 + X_{eq}^2)^2}{3L_t R_{eq} X_{eq} U_0}. \tag{15}$$

Recall that increasing the inner DG impedance or transient virtual impedance increases L_t. Clearly, this will reduce the maximum allowable droop gains. This result suggests that the stability margins for the low-frequency modes are reduced when the transient virtual impedance is used. On the other hand, increasing the quasi-stationary virtual impedance increases R_{eq} and/or X_{eq}. In this case, the maximum allowable values for the droop gains will also increase. Therefore, the effect of the transient and the quasi-stationary virtual impedance is different from this point of view.

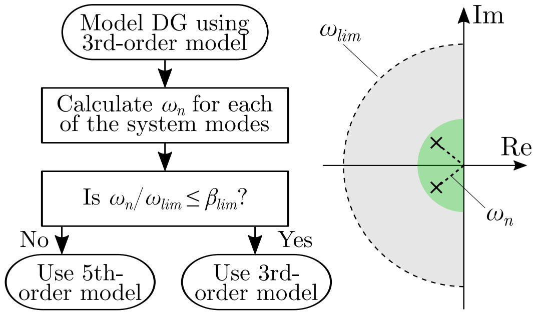

Fig. 5. Flow diagram for selecting whether to use 3rd- or 5th-order model.

IV. APPLICABILITY OF REDUCED-ORDER MODELLING

As noted in Section III, the first order Maclaurin series expansion in (10) is only valid for $|sL_t/(R_{eq} + jX_{eq})| \ll 1$. Hence, it is valid for frequencies given by:

$$\omega \ll \frac{\sqrt{R_{eq}^2 + X_{eq}^2}}{L_t} = \omega_{lim}. \tag{16}$$

In other words, the reduced order model is valid for modes with a natural frequency much less than ω_{lim}. Note that increasing the inner DG impedance and transient virtual impedance reduces ω_{lim}, while increasing the quasi-stationary virtual impedances increases the limit. Based on this, the flow diagram in Fig. 5 is proposed to determine whether the 3rd- or 5th-order model should be used to model a DG. The first step consists of modelling the DG using a 3rd-order model. Then, the natural frequency (ω_n) is calculated for each of the resulting modes. Next, ω_n/ω_{lim} is evaluated in order to test whether the first order Maclaurin series expansion is accurate. If this value is less than a number β_{lim}, the assumption is considered valid and the 3rd-order model can be used. The value β_{lim} can be selected depending on the accuracy needed

TABLE I
MAIN SIMULATION PARAMETERS

Par.	Value	Par.	Value	Par.	Value
m_p	1e-4 rad/(Ws)	L_f	0.5 mH	L_c	1.3 mH
n_q	1.3e-4 V/VAr	R_f	5 mΩ	R_c	0.13 Ω
τ	33.3 ms	C_f	50 µF	L_v	0.64 mH
K_{iv}	187.5	F	0.75	R_v	0.2 Ω

for the specific application. Small values of β_{lim} ensure that the 3rd-order model is only used when its modes closely correspond to the modes of the 5th-order model. If the ratio ω_n/ω_{lim} is larger than β_{lim}, the 5th-order model should be used.

In practical applications with droop-controlled DGs, the low-frequency modes typically have frequencies in the range $1-10$ Hz [25, 26]. Hence, this gives an indication of typical values for ω in (16). In the general case, however, this largely depends on the droop gains and low-pass filter time constant, in addition to the line impedance between DG units. To discuss typical values of ω_{lim}, it should first be observed that its minimum value is obtained for low R/X ratios. Then, the applicability of the third-order model increases if either the R/X ratio or the resistance increases. In cases where the R/X ratio is low, $\omega_{lim} \approx (\omega_0 L_c + \omega^* L_v)/L_t$. By assuming that L_c, L_v and L_o have comparable magnitudes, and that $\omega_0 \approx \omega^*$ the following lower bounds are then obtained:

$$\omega_{lim} \approx \begin{cases} 2\omega^*/3, & \text{for transient virtual impedance,} \\ \omega^*, & \text{for quasi-stationary virtual impedance.} \end{cases}$$

It can be seen that, under these considerations, the range of applicability of the reduced order model is larger for the quasi-stationary version of the virtual impedance.

V. ANALYTICAL RESULTS

A detailed averaged DG model based on [5] was used as a benchmark model to validate the reduced order models in (7) and (14). Table I summarizes the main parameters used in the numerical simulations and experiments. The nominal phase-to-phase voltage was 400 V and the nominal frequency was 50 Hz.

A. Model Validation Against Ideal Grid

Fig. 6 (a) displays the time-domain response of the frequency to a step change in the grid voltage for the detailed, 5th-order and 3rd-order models. Since the model developed in this work only considers small-signal dynamics, a step change of 1 % was applied to the input. Larger step changes can also be performed. However, this will give increasingly inaccurate results due to the non-linearity of the original model. For this test, $m_p =$ 6e-4 so that the DG operates close to the stability limits and therefore differences can be better studied. For the 5th- and 3rd-order models, both the effect of including and excluding internal dynamics are shown. It can be seen that the 5th-order model including internal dynamics accurately represents the detailed model. Meanwhile, the 3rd-order model with internal dynamics shows a slightly more damped response. The 5th-order model neglecting internal dynamics is slightly more accurate than the 3rd-order model with internal dynamics for the initial peak, but it is less accurate for the subsequent peaks. The reason for this is that the 5th-order model describes the current dynamics more accurately. However, the damping of the low-frequency modes is inaccurate when neglecting the internal dynamics. Also, the 3rd-order model without inner dynamics is the least accurate. These findings are supported by the root locus diagram in Fig. 6 (b), which shows the low-frequency eigenvalues when m_p is increased. For the models including internal dynamics, the eigenvalues of the 5th-order model closely match those of the detailed model, while the eigenvalues of the 3rd-order model are slightly more damped. The 5th-order and 3rd-order models neglecting internal dynamics deviate significantly from the detailed model, particularly for large values of m_p.

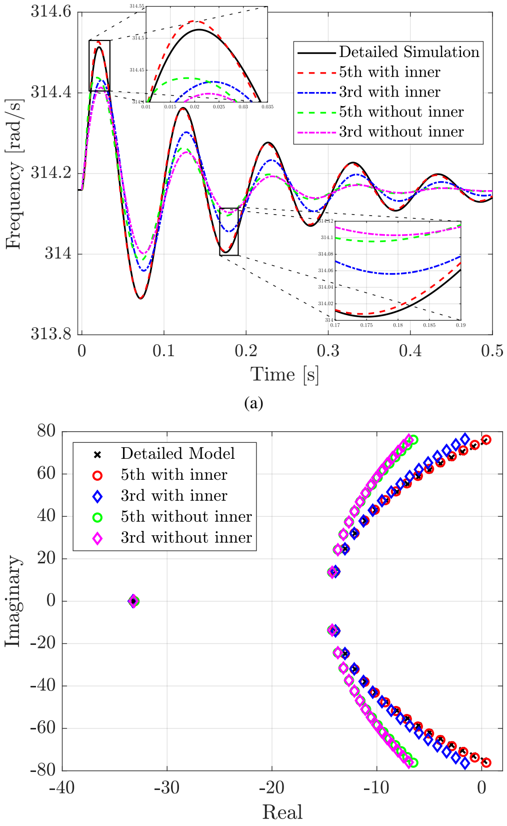

(a)

(b)

Fig. 6. (a) Dynamic response to a step change and (b) root locus diagram for the detailed model, and 5th-order and 3rd-order models with and without including internal dynamics.

B. Model Validation for a Small Microgrid

To test the accuracy of the reduced-order model in multi-converter systems, the MG presented in Fig. 7 was studied. It consists of two DGs, one electrical line and a load. The DGs have the same parameters as before. The line is modelled

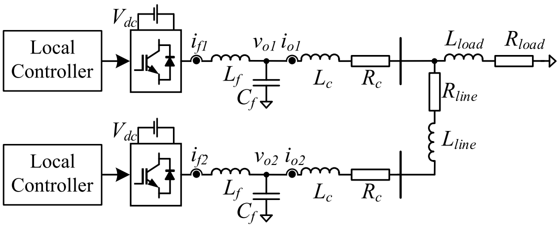

Fig. 7. MG configuration for testing the applicability of reduced-order models with more than one DG.

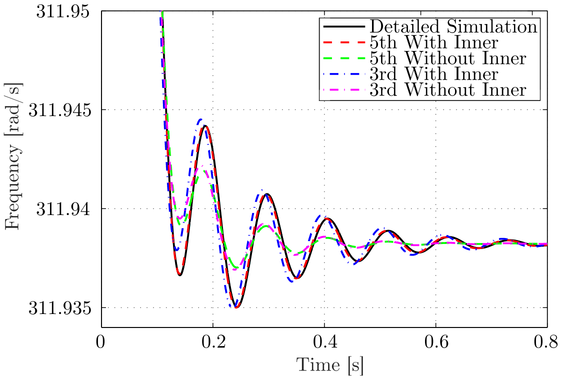

Fig. 8. Transient response of the frequency of DG1, when there is an increase of 1 kW in the load.

with an RL equivalent, where $R_{line} = 0.12\ \Omega$ and $L_{line} = 0.32$ mH. The load is modelled as another RL equivalent, with values $R_{load} = 26\ \Omega$ and $L_{load} = 3.2$ mH.

Initially, the load absorbs 3kW. Then, a load increase of 1 kW occurs. The resulting variation in the system frequency (taken as the frequency of DG1) is shown in Fig 8. This simulation is performed for the relatively large value of $m_p = 6.3\text{e-}4$, in order to highlight the differences between the models. It can be seen that the 5th-order model with inner dynamics accurately describes the detailed simulation. The 3rd-order model with inner dynamics also represents the detailed simulation adequately, although the response is slightly less damped. Meanwhile, the models neglecting the internal dynamics present significantly more damped behaviour compared to the detailed model.

C. Stability Regions for Different Virtual Impedances

Fig. 9 displays the parametric stability regions predicted by the model in (14) with (green) and without (red) transient virtual impedance. The stable region is below and to the left of the curves. The estimates of the stability boundaries in (15) are also given for the case with (blue) and without (black) transient virtual impedance. It can be seen that the estimates in (15) are accurate for the limit on n_q, while they are for the most part restrictive for the limit on m_p. It should be noted that this is not a general conclusion but applies for this operating point. Clearly, the stability region is smaller when employing the transient virtual impedance. Hence, employing transient virtual impedance reduces the stability margins.

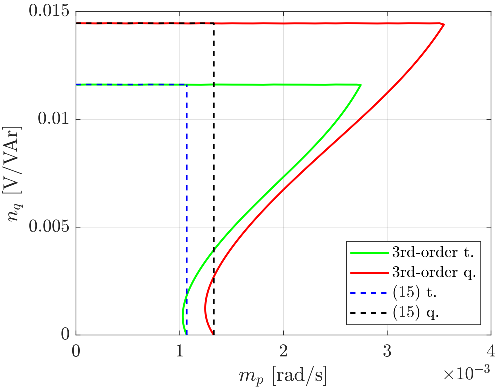

Fig. 9. Parametric stability limits predicted by the 3rd-order model with transient (t.) and quasi-stationary (q.) virtual impedance.

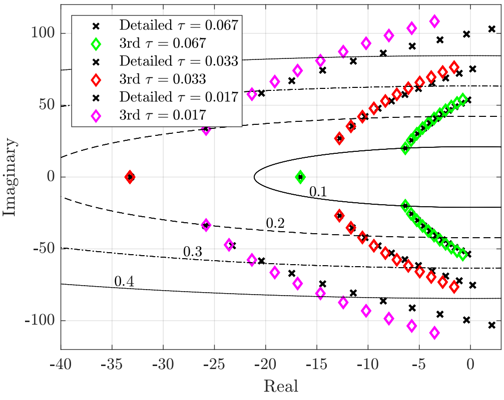

Fig. 10. Root locus diagram when increasing m_p for the detailed and 3rd-order models. The lines show constant values of ω_n/ω_{lim}.

D. Model Order Selection

Fig. 10 shows a root locus diagram of the detailed and 3rd-order models for three different values of τ. The lines mark constant values of ω_n/ω_{lim}. As a general trend, it can be seen that the match between the eigenvalues obtained from the reduced-order and analytical models gets worse as the frequency of the eigenvalues increases. There is a close match between eigenvalues located inside the lines marked by 0.1 and 0.2. Meanwhile, the eigenvalues located in the area where the ratio is between 0.2 and 0.3 display appreciable differences, particularly for the damping ratios. The difference between the damping ratios of the detailed and third-order models is further increased for larger ratios of ω_n/ω_{lim}. The relative error of the eigenvalues obtained by the 3rd-order model as a function of ω_n is plotted in Fig. 11. Clearly, the error increases with ω_n. The errors of the different cases are similar for the same frequency. Although the percentage error in Fig.

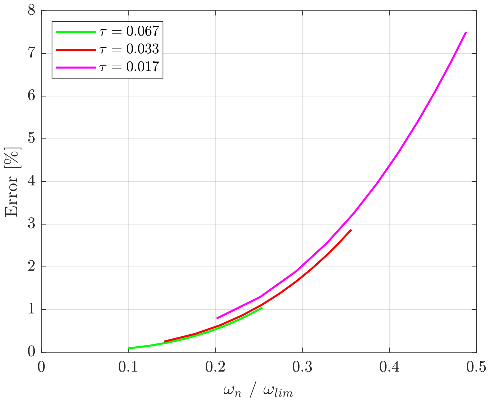

Fig. 11. Relative error of 3rd-order model with respect to the detailed model.

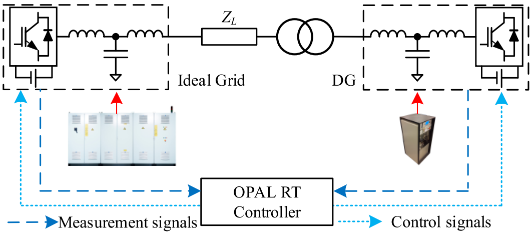

Fig. 12. Single-line diagram of the experimental setup.

11 is relatively small, it should be noted from Fig. 10 that the error is mainly associated with the real parts. Thus, it is particularly important to model the DG as a 5th-order model when ω_n/ω_{lim} is large and the system is operating close to the imaginary axis.

VI. Experimental Validation

A. Description of Laboratory Setup

Fig. 12 shows a single line diagram of the experimental setup. A 60 kVA VSC was used as the switching device. The switching and sampling frequencies were 10 kHz. Electrical lines were emulated by using external impedances, while the ideal grid was implemented in an EGSTON 200 kVA COMPISIO system unit. Uncertainties in the electrical parameters are implicit due to tolerances in the filter and impedance values. The main controllers of the DG and the ideal grid reference were implemented in Simulink and executed on an OP5600 real-time simulator by OPAL-RT.

B. Validation of Analytical Model

In this section, the accuracy of the detailed simulation model is analyzed. To this end, a step of 5 V is applied to the ideal grid voltage. As the accuracy of the reduced-order models has already been studied in relation to the detailed one (in Section V), the laboratory tests are aimed at validating the detailed model. Fig. 13 displays the response of the active and reactive powers, as well as voltages and currents of the DG for the experimental data (red) and analytical model (black). The active power shows a significant transient, before returning to zero since the grid imposes the nominal frequency. The reactive power displays a slight overshoot before settling at a negative value due to the increase of the grid voltage. The d-axis and q-axis voltages respectively increased and reduced because of the increased grid voltage (this happens because of the cross-coupling terms of the virtual impedance). The analytical model predicts a slightly larger overshoot than the experimental data for the d-axis voltage. The effect of the internal controllers in the initial part of the electrical transients can be easily distinguished in Figs. 13 (b,c,e,f). Clearly, the proposed reduced-order model analyzed in Fig. 6 is not able to capture these fast events, even though it accurately accounts for the effect of the fast dynamics on the low-frequency modes. The d-axis and q-axis currents respectively remained close to zero and increased significantly after an initial transient. For all variables, it is evident that the low-frequency dynamics are adequately represented by the detailed analytical model. The high-frequency dynamics are not captured by the model since switching effects are not included in the model.

C. Comparison of Virtual Impedance Implementations

To further validate the claim that the transient virtual impedance reduces the stability margins compared with the quasi-stationary virtual impedance, both alternative methods were implemented in the laboratory. Since the differences between these implementations are more evident when the DG is working close to its stability limits, the value of m_p was increased to 4.4e-4, while L_c was reduced to 0.3 mH. Fig. 14 shows the active and reactive powers injected by the DG after applying a step of 5 V to the grid voltage value. It can be seen that including transient virtual impedance results in larger overshoot and oscillations, thus indicating a smaller damping compared to the quasi-stationary case.

VII. Discussion

A. Parameter Selection of Droop-Controlled DGs

Based on the analysis in this paper, it is clear that the parameter L_t should be minimized to enlarge the system stability margins of droop-controlled DGs. As discussed, one measure for achieving that is to use the quasi-stationary instead of the transient virtual impedance. In addition, reducing the internal impedance of the DG would contribute to the reduction of L_t. This can be achieved by increasing F, as $L_o = (1-F)/K_{iv}$. Setting $F = 1$ would cancel the effect of the internal dynamics in the low-frequency range completely. However, setting $F = 1$ could lead to a negative value of the output impedance (Z_o), which, depending on the dynamics of the output current, could lead to a positive feedback. For this reason, the value of F is typically set below 1. Increasing the voltage controller integral gain also reduces the internal impedance. Therefore, this is another option for increasing the stability margins. However, this parameter should not be too large, as this would reduce the phase margin of the voltage controller.

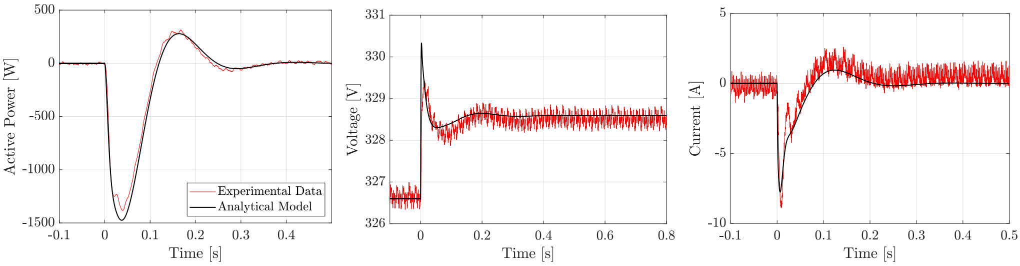

(a) Active power (b) d-axis voltage (c) d-axis current

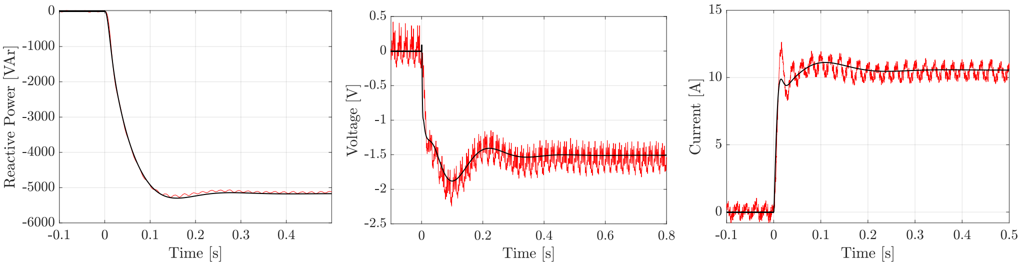

(d) Reactive power (e) q-axis voltage (f) q-axis current

Fig. 13. Comparison between experimental data (red) and analytical model (black) to a step change in the grid voltage.

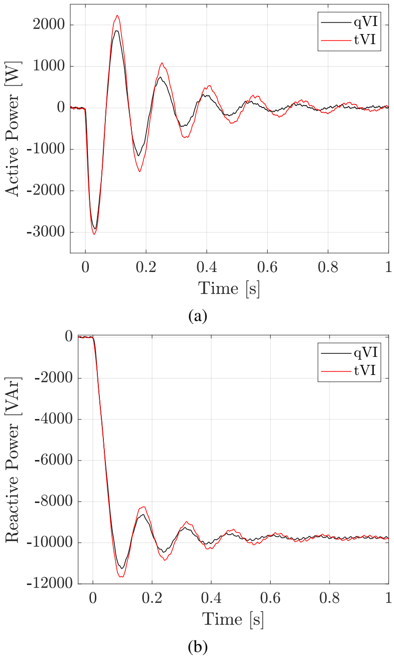

Fig. 14. Dynamic response to a step change for (a) active power and (b) reactive power with quasi-stationary (black) and transient (red) virtual impedance implementations.

VIII. CONCLUSION

In this paper, a reduced-order model of a DG that takes into account the effect of virtual impedances, internal control loops and the connection filter has been developed. The model included the droop controllers, the angle dynamics and an approximation based on dynamic phasors for the electrical interconnection. The dynamics of the internal control loops and the DG output impedance were modelled by approximating the low-frequency responses of the transfer functions representing the tracking capability and equivalent output impedance of the DG. The accuracy of the model was analyzed, and a methodology for deciding when 5th-order models can be reduced to 3rd-order ones was proposed. The proposed model was used to study the stability limits of the transient and the quasi-stationary implementation of virtual impedances. Finally, the main contributions were validated in a 60 kVA DG connected to a grid emulator.

The model shows that the DG internal control loops represent an additional transient impedance that tends to reduce the stability margins. It is also shown that including quasi-stationary virtual impedances increase the stability margins. However, the transient part of the virtual impedance reduced the stability margins. The methodology for checking the applicability of 3rd-order models provided a simple test for evaluating the validity of the results obtained with the 3rd-order model. This methodology provides a straightforward criterion for selecting the model-order of DGs in studies of larger systems. Finally, it was shown that theoretical and experimental results were in good agreement.

REFERENCES

[1] R. H. Lasseter, "MicroGrids," *2002 IEEE Power Engineering Society Winter Meeting. Conference Proceedings (Cat. No.02CH37309)*, vol. 1, pp. 305–308, 2002. [Online]. Available: http://ieeexplore.ieee.org/lpdocs/epic03/wrapper.htm?arnumber=985003

[2] D. E. Olivares, A. Mehrizi-Sani, A. H. Etemadi, C. A. Cañizares, R. Iravani, M. Kazerani, A. H. Hajimiragha, O. Gomis-Bellmunt, M. Saeedifard, R. Palma-Behnke, G. A. Jiménez-Estévez, and N. D. Hatziargyriou, "Trends in microgrid control," *IEEE Transactions on Smart Grid*, vol. 5, no. 4, pp. 1905–1919, 2014.

[3] F. Blaabjerg, R. Teodorescu, M. Liserre, and A. V. Timbus, "Overview of control and grid synchronization for distributed power generation systems," *IEEE Transactions on Industrial Electronics*, vol. 53, no. 5, pp. 1398–1409, 2006.

[4] M. C. Chandorkar, D. M. Divan, and R. Adapa, "Control of Parallel Connected Inverters in Standalone ac Supply Systems," *IEEE Transactions on Industry Applications*, vol. 29, no. 1, pp. 136–143, 1993.

[5] N. Pogaku, M. Prodanović, and T. C. Green, "Modeling, analysis and testing of autonomous operation of an inverter-based microgrid," *IEEE Transactions on Power Electronics*, vol. 22, no. 2, pp. 613–625, 2007.

[6] I. P. Nikolakakos, H. H. Zeineldin, M. S. El-Moursi, and N. D. Hatziargyriou, "Stability Evaluation of Interconnected Multi-Inverter Microgrids Through Critical Clusters," *IEEE Transactions on Power Systems*, vol. 31, no. 4, pp. 3060–3072, 2016.

[7] E. A. A. Coelho, P. C. Cortizo, and P. F. D. Garcia, "Small-Signal Stability for Parallel-Connected Inverters in Stand-Alone ac Supply Systems," *IEEE Transactions on Industry Applications*, vol. 38, no. 2, pp. 533–542, 2002.

[8] J. M. Guerrero, L. G. de Vicuna, J. Matas, M. Castilla, and J. Miret, "A wireless controller to enhance dynamic performance of parallel inverters in distributed generation systems," *IEEE Transactions on Power Electronics*, vol. 19, no. 5, pp. 1205–1213, 2004.

[9] S. V. Iyer, M. N. Belur, and M. C. Chandorkar, "A Generalized Computational Method to Determine Stability of a Multi-inverter Microgrid," *IEEE Transactions on Power Electronics*, vol. 25, no. 9, pp. 2420–2432, 2010.

[10] X. Guo, Z. Lu, B. Wang, X. Sun, L. Wang, and J. M. Guerrero, "Dynamic Phasors-Based Modeling and Stability Analysis of Droop-Controlled Inverters for Microgrid Applications," *IEEE Transactions on Smart Grid*, vol. 5, no. 6, pp. 2980–2987, 2014.

[11] L. Luo and S. V. Dhople, "Spatiotemporal model reduction of inverter-based islanded microgrids," *IEEE Transactions on Energy Conversion*, vol. 29, no. 4, pp. 823–832, 2014.

[12] V. Mariani, F. Vasca, J. C. Vásquez, and J. M. Guerrero, "Model Order Reductions for Stability Analysis of Islanded Microgrids With Droop Control," *IEEE Transactions on Industrial Electronics*, vol. 62, no. 7, pp. 4344–4354, 2015.

[13] P. Vorobev, P. H. Huang, M. A. Hosani, J. L. Kirtley, and K. Turitsyn, "High-Fidelity Model Order Reduction for Microgrids Stability Assessment," *IEEE Transactions on Power Systems*, vol. 33, no. 1, pp. 874–887, 2018.

[14] Y. Gu, N. Bottrell, and T. C. Green, "Reduced-Order Models for Representing Converters in Power System Studies," *IEEE Transactions on Power Electronics*, vol. 33, no. 4, pp. 3644–3654, 2018.

[15] H. Yu, J. Su, Y. Wang, H. Wang, and Y. Shi, "Modeling Method and Applicability Analysis of Inverter's Reduced-Order Model for Microgrid Applications," *IET Power Electronics*, 2020.

[16] J. M. Guerrero, L. G. Vicuña, J. Matas, M. Castilla, and J. Miret, "Output impedance design of parallel-connected UPS inverters with wireless load sharing control," *IEEE Transactions on Industrial Electronics*, vol. 52, no. 4, pp. 1126–1135, 2005.

[17] J. He and Y. W. Li, "Analysis, Design, and Implementation of Virtual Impedance for Power Electronics Interfaced Distributed Generation," *IEEE Transactions on Industry Applications*, vol. 47, no. 6, pp. 2525–2538, 11 2011.

[18] X. Wang, Y. W. Li, F. Blaabjerg, and P. C. Loh, "Virtual-Impedance-Based Control for Voltage-Source and Current-Source Converters," *IEEE Transactions on Power Electronics*, vol. 30, no. 12, pp. 7019–7037, 2015.

[19] J. M. Guerrero, J. Matas, L. G. Vicuña, M. Castilla, and J. Miret, "Decentralized control for parallel operation of distributed generation inverters using resistive output impedance," *IEEE Transactions on Industrial Electronics*, vol. 54, no. 2, pp. 994–1004, 2007.

[20] W. Yao, M. Chen, J. Matas, J. M. Guerrero, and Z. M. Qian, "Design and analysis of the droop control method for parallel inverters considering the impact of the complex impedance on the power sharing," *IEEE Transactions on Industrial Electronics*, vol. 58, no. 2, pp. 576–588, 2011.

[21] P. H. Huang, P. Vorobev, M. Al Hosani, J. L. Kirtley, and K. Turitsyn, "Plug-and-Play Compliant Control for Inverter-Based Microgrids," *IEEE Transactions on Power Systems*, vol. 34, no. 4, pp. 2901–2913, 2019.

[22] S. d. J. M. Machado, S. A. O. d. Silva, J. R. B. d. A. Monteiro, and A. A. de Oliveira, "Network Modeling Influence on Small-Signal Reduced-Order Models of Inverter-Based AC Microgrids Considering Virtual Impedance," *IEEE Transactions on Smart Grid*, vol. 3053, no. c, pp. 1–1, 2020.

[23] A. Yazdani and R. Iravani, *Voltage-Sourced Converter in Power Systems: Modelling Control and Application*. New York: Wiley, 2010.

[24] S. Eberlein and K. Rudion, "Small-signal stability modelling, sensitivity analysis and optimization of droop controlled inverters in LV microgrids," *International Journal of Electrical Power and Energy Systems*, vol. 125, no. July 2020, 2021. [Online]. Available: https://doi.org/10.1016/j.ijepes.2020.106404

[25] Y. Mohamed and E. F. El-Saadany, "Adaptive Decentralized Droop Controller to Preserve Power Sharing Stability of Paralleled Inverters in Distributed Generation Microgrids," *IEEE Transactions on Power Electronics*, vol. 23, no. 6, pp. 2806–2816, 2008.

[26] N. Hatziargyriou, J. Milanović, C. Rahmann, V. Ajjarapu, C. Cañizares, I. Erlich, D. Hill, I. Hiskens, I. Kamwa, B. Pal, P. Pourbeik, J. Sanchez-Gasca, A. Stanković, T. Van Cutsem, V. Vittal, and C. Vournas, "Stability definitions and characterization of dynamic behavior in systems with high penetration of power electronic interfaced technologies," IEEE Power and Energy Society, Tech. Rep. PES-TR77, 2020.

Fredrik Göthner was born in Oslo, Norway, in 1992. He received the M.Sc. degree in electrical power engineering in 2017 from the Norwegian University of Science and Technology (NTNU), Trondheim, Norway, where he is currently working toward the Ph.D. degree on the control of converters in microgrids. His main research interests include control of power electronics and issues related to stability and power quality in microgrids.

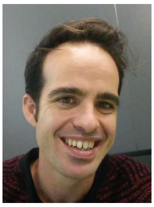

Javier Roldán-Pérez (S'12-M'14) received a B.S. degree in industrial engineering, a M.S. degree in electronics and control systems, a M.S. degree in system modeling, and a Ph.D. degree in power electronics, all from Comillas Pontifical University, Madrid, in 2009, 2010, 2011, and 2015, respectively. From 2010 to 2015, he was with the Institute for Research in Technology (IIT), Comillas University. In 2014, he was a visiting Ph.D. student at the Department of Energy Technology, Aalborg University, Denmark. From 2015 to 2016 he was with the Electric and Control Systems Department at Norvento Energía Distribuida. In September 2016 he joined the Electrical Systems Unit at IMDEA Energy Institute. In 2018, he did a research stay at SINTEF Energy Research, Trondheim. His research topics are the integration of renewable energies, microgrids, and power electronics applications.

Raymundo E. Torres-Olguin received the B.Sc. degree in electromechanical engineering from the University of San Luis Potosí, Mexico, in 2004, M.Sc. degree in control and dynamical systems from the Applied Mathematics Department, Research Institute of Science and Technology of San Luis Potosí (IPICYT), Mexico, in 2006, and Ph.D. degree in electric power engineering from the Norwegian University of Science and Technology (NTNU), Norway, in 2013. From 2012, he has worked as a research scientist in SINTEF Energy Research located in Trondheim, Norway. His main research interest includes control of power electronics for the integration of renewable resources, dc transmission and microgrids.

Ole-Morten Midtgård (M’03) was born in Tromsø, Norway, in 1967. He received the M.Sc. and Ph.D. degrees in Electric Power Engineering from the Norwegian University of Science and Technology (NTNU), Trondheim, Norway, in 1992 and 1997, respectively. He is currently Head of Department at NTNU’s Department of Electric Power Engineering, where he has been a Professor since 2012. Previous employments include 5 years at ABB and 8 years tenure at the University of Agder, Grimstad, Norway. Prof. Midtgård is an elected member of the Norwegian Academy of Technological Sciences (NTVA) and of Agder Academy of Sciences and Letters. He has broad research interests, which in addition to power electronics include electromagnetic computations, and applications such as microgrids, integration of PV in smart grids, and electric aviation.

Paper III

The paper "Harmonic Virtual Impedance Design for Optimal Management of Power Quality in Microgrids" is published in *IEEE Transactions on Power Electronics.*

Harmonic Virtual Impedance Design for Optimal Management of Power Quality in Microgrids

Fredrik Göthner, Javier Roldán-Pérez, *Member, IEEE*, Raymundo E. Torres-Olguin, and
Ole-Morten Midtgård, *Member, IEEE*

***Abstract*—Power quality is an important concern for practical microgrid (MG) applications due to the widespread use of non-linear loads, and it is characterized by the implicit trade-off between voltage quality in the MG nodes and harmonic current sharing between distributed generators (DGs). Active and passive filters can be used to address this problem. Nevertheless, modification of the control system of the DGs represents a cheaper and more practical solution. To this end, virtual impedances (VIs) can be included in the controller. However, the power quality trade-off is difficult to adjust, especially in the presence of electrical distribution lines. In this paper, an optimization algorithm for setting the harmonic VIs of the DGs in a multibus MG is presented. This optimization algorithm can be easily configured for any degree of harmonic current sharing between the DGs, while improving the voltage quality is set as the main objective. Compared to other works presented in the literature, power quality can be managed without relying on time-critical communications since only the values of the harmonic VIs are modified in the optimization problem. The optimization is executed periodically so that the VIs are adapted to changes in the grid. Theoretical developments were validated by simulation in a benchmark model, and in a laboratory environment.**

***Index Terms*—Microgrid Control, Power Quality, Current Harmonic Sharing, Virtual Impedance.**

I. INTRODUCTION

A. Motivation

POWER quality standards have traditionally established limits for current harmonics generated by loads, as well as limits for the harmonic voltage components and total harmonic distortion (THD) at the system nodes [1, 2]. For microgrids (MGs), it is expected that new regulations will add power quality requirements for DGs to guarantee their safe integration into power networks, both in the grid-connected and islanded modes, similarly to DG interconnection standards [3]. Moreover, due to the rapid deployment and great versatility of power electronics interfaced DGs [4], these elements will have an active role in improving the power quality. However, current and voltage harmonics in DGs should not exceed certain limits, since they have a relevant impact on the reliability and lifetime of the DGs. Typically, the main task of a DG is to deliver power to the grid, or to regulate the MG frequency and voltage. Hence, the spare capacity (i.e. capacity available for improving the voltage quality) is the rated capacity minus the capacity used by the primary function, and this is greatly restricted by operational constraints. Therefore, a coordinated control strategy is needed for an efficient utilization of the resources.

B. Literature Review

For MGs operating in island mode, the conventional $P\omega - QV$ droop control enables DGs to share the load with very low dependence on communication systems [5]. However, the conventional droop control has important limitations in dealing with current and voltage harmonics. Consequently, several strategies have been proposed in the literature to address this issue [6–26]. These strategies can be classified as droop-based, centralized and virtual impedance-based approaches. One of the earliest droop-based strategies was proposed by Lee *et al.* [6]. Here, a harmonic conductance is drooped against harmonic power [27]. This control solution can be easily added to the fundamental droop control loop and it does not require the use of communication systems. However, the approach may give rise to undamped oscillations in the voltage at the point of common coupling (PCC), especially when DGs are interfaced via LCL filters and electrical lines are long [7]. Another droop-based approach is proposed by Moussa *et al.* [7]. In that work, a harmonic droop controller is used to guarantee an accurate sharing of harmonic currents consumed by the MG loads. However, this method requires relatively fast communication systems to assess the harmonic content at the PCC in real-time, and a single bus of the MG is used for calculating the control action. Therefore, this method would need to be modified for application in more complex MG topologies.

A different strategy for improving voltage quality in MGs using a centralized approach is proposed by Savaghebi *et al.* [9]. In that work, a hierarchical control structure regulates the magnitude of each voltage harmonic at the node where a sensitive load is connected. This control goal is achieved by modifying the voltage reference of each DG. The scheme can effectively improve the grid voltage quality, but it is limited to simple topologies as it only considers one load bus. Hence, the expansion of this solution might be challenging for more complex MG configurations. This issue is addressed for voltage unbalance compensation in [10], where the tertiary controller includes an optimization algorithm that guarantees acceptable voltage quality in each of the selected buses. Another centralized approach was proposed in [11]. This

This work has been funded by CINELDI - Centre for intelligent electricity distribution, an 8-year Research Centre under the FME-scheme (Centre for Environment-friendly Energy Research, 257626/E20). The authors gratefully acknowledge the financial support from the Research Council of Norway and the CINELDI partners. The work of IMDEA Energy Institute received financial through the research programme S2018/EMT-4366 PROMINT-CAM of Madrid Government, with 50% support of the European Social Fund.

Fredrik Göthner and Ole-Morten Midtgård are with the Norwegian University of Science and Technology 7034, Trondheim, Norway (e-mail: fredrik.gothner@ntnu.no; ole-morten.midtgard@ntnu.no).

Javier Roldán-Pérez is with IMDEA Energy Institute, Madrid, 28935 Spain (e-mail: javier.roldan@imdea.org).

Raymundo E. Torres-Olguin is with SINTEF Energy Research, 7034 Trondheim, Norway (e-mail: raymundo.torres-olguin@sintef.no).

controller is applicable to MGs consisting of both current- and voltage-controlled DGs, and it enables harmonic current sharing between parallel-connected DGs. However, its application to a more general MG topology would require additional research efforts.

Another category for improving harmonic sharing and reducing the PCC voltage THD is by applying outer virtual impedances (VIs) [12–17]. The fundamental principle is to use the output current of the inverter and multiply it by an impedance value chosen by the designer. The designed VI can either be the same for all current harmonics [13], or applied to a specific harmonic [14–17]. One of the main drawbacks of the virtual impedance approach is the inherent trade-off between harmonic current sharing between the DGs and voltage distortion [16]. While accurate harmonic sharing can be guaranteed if the VIs are set large enough, this might lead to a relatively large voltage distortion [16]. In [17], this problem is addressed by applying negative virtual inductances in order to compensate for large physical feeders. However, negative VIs have an adverse impact on closed-loop stability. Therefore, this method should be applied carefully as it requires a priori knowledge of the line feeders or a need for setting a relatively large safety margin during the design process. This problem is addressed in [18], in which the feeder impedance of each DG is first estimated and then used as an input for an optimization algorithm. The solution provides an optimal value of the harmonic VIs. In [19], this problem is addressed similarly by adapting the VIs in two stages: the VI is first tuned to achieve current sharing, before the second stage reduces the VIs to ensure improved PCC voltage quality. This method provides adequate results. However, it requires relatively fast communications in order to guarantee the system stability. Another approach is given in [20], where the VIs are tuned adaptively based on the magnitudes of the harmonics at one node of the MG. Blanco *et al.* [21] proposed virtual admittances for harmonic compensation, which are applicable for both current- and voltage-controlled DGs. Virtual admittances and harmonic current references are provided by a central controller based on the measured voltage harmonics at the PCC. It is shown that distribution losses can be reduced if the same virtual admittance is used for all DGs. In [22], an autonomous approach for voltage harmonic compensation using virtual impedance and admittance design that also considers the available capacity of the DGs is given. However, equal harmonic current sharing is not possible with the proposed scheme in the general case. Baghaee *et al.* [23] proposed a hierarchical control that is able to improve the voltage quality by using VIs and a harmonic compensation scheme. The voltage of one the MG buses is used for the compensation.

Although there has been a significant amount of research on power quality issues in islanded MGs, this has been mainly limited to grid topologies with several DGs operating in parallel to feed a common load. This might not be the case for several types of MGs, e.g. residential MGs. However, there has recently been an increased interest in power quality improvements for more general MG topologies [24–26]. In [24], an optimization algorithm is presented for improving the voltage unbalance for a more general radial MG. The scheme is enabling improved voltage quality, but it requires to continuously send voltage references to the DGs from a central controller. A real-time supervisory control for power quality improvement in multi-area MGs is proposed in [25]. However, the main aim of the control is to allocate the least number of DGs or active power filters, which is the opposite of sharing the harmonic compensation. In [26], an optimization method is formulated for improving the voltage quality in an MG. While this method improves the voltage quality, it does not consider harmonic current sharing between DGs.

C. *Contribution and Paper Organization*

In this paper, an optimization algorithm that calculates the harmonic VIs of DGs is proposed. The main contributions of this work are:

1) The algorithm minimizes the voltage THD while ensuring a degree of current harmonic sharing. Hence, the algorithm reflects the trade-off between DG harmonic current sharing and voltage distortion in the MG nodes. It will be shown that the trade-off can be easily adjusted by selecting a parameter of the optimization problem.
2) The proposed optimization algorithm is applicable for any MG topology.
3) The method does not rely on time-critical communications.

The optimization algorithm includes constraints such that electrical variables are within their operational limits, as specified by standards. It will be shown that the VIs can be periodically updated in the DGs, so that the controller adapts to changes in the operating conditions. Simulation results of a benchmark MG are used to demonstrate the benefits of the proposed solution. Also, experimental results are included to validate the basic features of the proposed algorithm.

The rest of this article is organized as follows. Section II presents an overview of the proposed algorithm, along with an overview of the droop-controlled DG that will be used in this paper. In Section III, the proposed optimization algorithm is explained. In Section IV, the proposed algorithm is applied to the benchmark MG, while experimental results are given in Section V. Finally, Section VI discusses the main results, before the conclusions are drawn in Section VII.

II. APPLICATION AND CONTROL SYSTEM OVERVIEW

A. *Overview of the Application and the Proposed Solution*

Fig. 1 shows the MG considered in this work, which is based on a low-voltage benchmark model for European distribution networks [28]. This system is representative of traditional electrical distribution systems that have been upgraded with a large share of renewable energy sources. Also, it has been reinforced to work either connected to the grid or in island mode. In the proposed solution, the harmonic content of the load currents is used as inputs for an optimization algorithm that is executed in the MG central controller (MGCC). The output of the algorithm are the VI values, which are sent via low-bandwidth communications to the DGs.

The main objective of the proposed algorithm is to optimize the voltage quality of the MG while simultaneously ensuring a

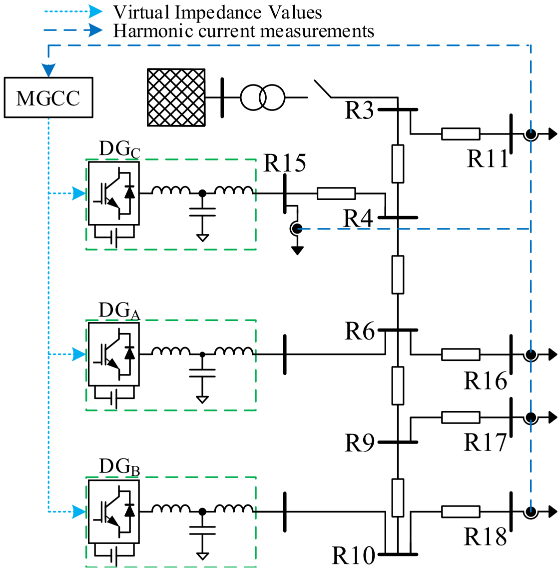

Fig. 1. Electrical and control diagram for the application. The system is based on a benchmark MG for electrical distribution systems with high penetration of renewable energies [28].

certain degree of harmonic current sharing between the DGs. Fig. 2 displays the main steps of the algorithm. First, the load currents are measured, and their harmonic content is extracted. Thus, there is a need for having a dedicated current sensor for each load. Then, the extracted harmonic content is sent to the MGCC, where the proposed optimization algorithm is executed for all the harmonics addressed by the VIs. Finally, the VIs are sent to the DGs where they are updated. The optimization is done using a global synchronous reference frame (SRF). This means that the measurements of the DGs should be sent together with a global time stamp so that they can be translated to this reference frame. The objective function minimizes the harmonic voltages of the MG nodes. Hence, the decision variables are the voltage harmonics at each node and the virtual admittances of each DG at each harmonic frequency. In addition, the following constraints complete the optimization algorithm:

1) Kirchhoff's Current Law applied to all system nodes.
2) DG equivalent harmonic impedances should be greater than a minimum.
3) Node harmonic voltages should comply with standards.
4) A certain degree of DG current harmonic sharing should be maintained.

The first constraint represents a physical limitation. The second constraint is included to avoid excessive use of negative VIs so that the MG stability is preserved. The third constraint is included to ensure that the harmonic content complies with standards (e.g. EN 50160 [2]). Finally, the fourth constraint ensures that the DGs share the harmonic currents to a certain degree. The output from the proposed optimization algorithm

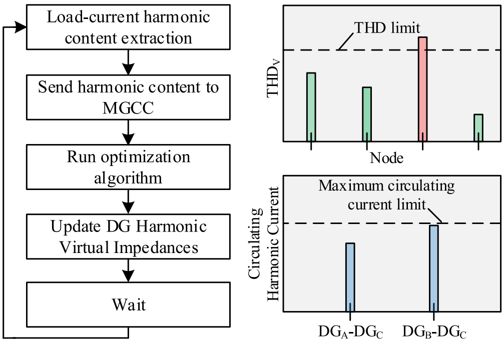

Fig. 2. Sequence showing the application of the proposed optimization. The optimization reduces node harmonic voltages, while ensuring a degree of DG current harmonic sharing.

are the values for the harmonic VIs of the DGs that will be updated via a communication channel. Finally, the entire procedure is repeated after a certain time.

B. Distributed Generator Control System

Fig. 3 shows the conventional solution for controlling grid-supporting DGs in MGs that is used in this paper [29]. The DG is connected to the grid via an LCL filter. An internal current controller is used to control the current through the converter-side inductor (i_c), while an external voltage controller is used to control the voltage across the filter capacitor (v_c). These controllers are implemented in an SRF that is internally generated by the DG. Variables in the SRF will be written in bold and are organized as column vectors (e.g. $\boldsymbol{x} = [x_d \; x_q]^T$, where T denotes the transpose). The current controller includes two PI regulators (one for each axis) to track the current references ($\boldsymbol{i}_c^*$) and appropriate decoupling and feedforward terms. The voltage controller also consists of two PI regulators with conventional voltage decoupling terms and feedforward of the output current (i_o). A plug-in resonant controller is used in the voltage controller so that harmonic voltages can be addressed adequately [30]. Also, a virtual impedance loop is included. This loop and its features will be explained in the following subsection.

Standard $P\omega$ and QV droops with additional derivative terms have been used to achieve proper sharing of active and reactive power between the DGs. The droop equations for DG j are given by:

$$\omega_j = \omega^* - m_j(P_j - P_j^*) - m_{d,j}\frac{d}{dt}(P_j - P_j^*), \qquad (1)$$

$$E_j = E^* - n_j(Q_j - Q_j^*) - n_{d,j}\frac{d}{dt}(Q_j - Q_j^*), \qquad (2)$$

where ω_j and ω^* are the angular frequency of the DG and its nominal value, respectively. E_j and E^* represent the droop control voltage reference and its nominal value, while m_j and n_j are the conventional droop gains. The gains $m_{d,j}$ and $n_{d,j}$ are the derivative action droop gains, which are used for improving the stability margins and transient performance. They were required for the MG since the electrical lines were relatively short. P_j^* and Q_j^* are the active and reactive power

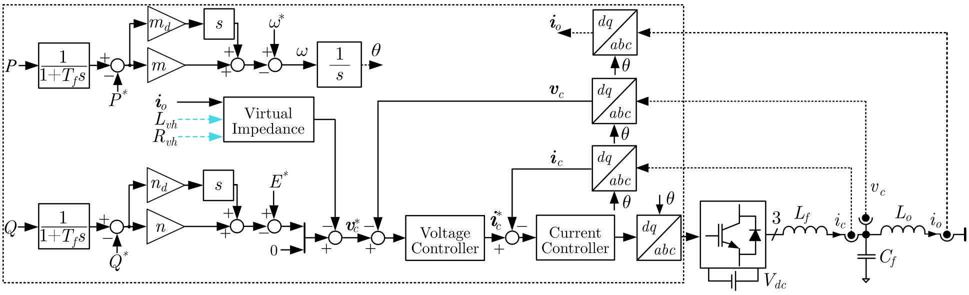

Fig. 3. Electrical and control diagram of a DG unit, including internal control loops, VIs and droop controllers. The VI values specified by the MGCC are highlighted.

references, while P_j and Q_j are filtered active and reactive powers given by:

$$P_j = \frac{1}{1+T_f s}(v_{cd,j} i_{od,j} + v_{cq,j} i_{oq,j}), \tag{3}$$

$$Q_j = \frac{1}{1+T_f s}(v_{cq,j} i_{od,j} - v_{cd,j} i_{oq,j}), \tag{4}$$

where T_f is the low-pass filter time constant. In the rest of the paper, subscript j will be omitted whenever possible for the sake of clarity. The angle used for dq-transformations is θ_j, which is obtained by integrating the angular frequency ω_j.

C. Outer VI Control

Virtual impedances are typically adopted to improve reactive power sharing in islanded MGs [31]. Depending on the ratio between reactance and resistance and the desired control strategy, both virtual inductances and resistances are commonly employed at the fundamental frequency. In addition, VIs that only address specific harmonics (i.e. harmonic VIs) can be used to improve the harmonic sharing. In this work, individual harmonics are extracted using multiple synchronous reference frames [17]. If both fundamental and harmonic VIs are employed, the resulting voltage reference can be calculated as follows:

$$\boldsymbol{v}_c^* = [E^* \quad 0]^T - \boldsymbol{Z}_{v,f} \boldsymbol{i}_{o,f} - \sum_h \boldsymbol{Z}_{v,h} \boldsymbol{i}_{o,h}, \tag{5}$$

where h is the harmonic number and f is the fundamental frequency ($h = 1$), $\boldsymbol{v}_c^*$ is the modified voltage reference, $[E^* \quad 0]^T$ is the voltage reference provided by the droop controller, $\boldsymbol{i}_{o,f}$ and $\boldsymbol{i}_{o,h}$ denote the fundamental and harmonic component h of the output current, while $\boldsymbol{Z}_{v,f}$ and $\boldsymbol{Z}_{v,h}$ are the VIs for the fundamental and harmonic frequency h, respectively. The latter is calculated as follows:

$$\boldsymbol{Z}_{v,h} = \begin{bmatrix} R_{v,h} & -h\omega L_{v,h} \\ h\omega L_{v,h} & R_{v,h} \end{bmatrix}, \tag{6}$$

where $R_{v,h}$ and $L_{v,h}$ are the virtual resistance and inductance, respectively, and ω is the rotational frequency of the SRF calculated by the droop controller.

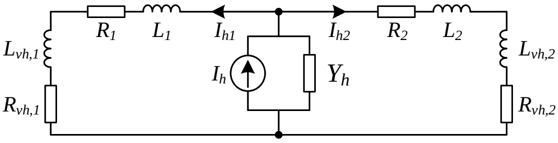

Fig. 4. Simplified electrical model at harmonic frequency of two parallel DGs and a load.

D. Harmonic Sharing in Microgrids

The diagram in Fig. 4 will be used to highlight the trade-off between voltage harmonics and sharing of current harmonics, and to introduce the notation used in the rest of the paper. The model represents the equivalent circuit of two DGs and a load, at a specific harmonic frequency (h). The load is modelled as a Norton equivalent consisting of a current source (I_h) and a parallel admittance (Y_h). The DGs are modelled by their harmonic VIs ($L_{v,h}$ and $R_{v,h}$), while the electrical lines are modelled by a series connection of inductance and resistance (L and R). The equivalent impedances of the DGs are the sum of the virtual and physical impedances. These are denoted Z_1 and Z_2 for DG1 and DG2, respectively. The harmonic currents drawn by DG1 and DG2 with respect to the harmonic load current are then given by:

$$\frac{i_{h1}}{I_h} = \frac{1/Z_1}{1/Z_1 + 1/Z_2 + Y_h}, \tag{7}$$

$$\frac{i_{h2}}{I_h} = \frac{1/Z_2}{1/Z_1 + 1/Z_2 + Y_h}. \tag{8}$$

Combining (7) and (8), the harmonic sharing between the two DGs can then be expressed as:

$$i_{h1} Z_1 = i_{h2} Z_2. \tag{9}$$

Thus, the DG with the smaller equivalent impedance will consume a larger share of harmonic currents. This issue can be solved by increasing the VI for the DG with the smallest equivalent impedance. If the physical feeder impedances are unknown, accurate current sharing can be achieved by using large VIs. However, this will produce a larger harmonic voltage drop at the terminals of the DGs, thereby deteriorating the voltage quality [14]. The feeder impedances can also be matched by using negative VIs for the DG connected by the largest physical impedance [17]. However, excessive use of

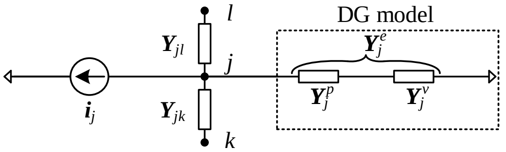

Fig. 5. General node used for the optimization, including a DG, load and interconnecting line admittances.

negative VIs might reduce stability margins, so this solution is commonly avoided.

III. PROPOSED OPTIMIZATION ALGORITHM

In this section, the proposed algorithm for improving the power quality is presented. First, the notation will be introduced, and the objective function will be chosen. Then, the constraints for the optimization problem will be explained.

A. Notation and Algorithm Overview

In the rest of the paper, matrices are uppercase and in boldface, while their elements are uppercase. Vectors are lowercase and in boldface, while their elements are lowercase. In order to explain the notation, Fig. 5 shows an electrical schematic of a generic node in the MG. Each node j is connected to at least one other node. In Fig. 5, node j is connected to nodes k and l via the line admittances $\boldsymbol{Y}_{jk}$ and $\boldsymbol{Y}_{jl}$, respectively. Any loads at the node are aggregated and represented by the current source $\boldsymbol{i}_j$. DGs are modelled by their equivalent admittance $\boldsymbol{Y}_j^e$, which consists of the physical admittance $\boldsymbol{Y}_j^p$ in series with the virtual admittance $\boldsymbol{Y}_j^v$. The latter is emulated by the DG controller, and its design and analysis represent the main contribution of this paper.

The optimization algorithm is run for each harmonic h. However, in order to simplify the notation, superscript h is omitted from the variables in the objective function and constraints.

B. Optimization Problem Formulation

The following objective function has been chosen:

$$\min \sum_{j=1}^{r} c_j \left((v_j^d)^2 + (v_j^q)^2 \right), \quad c_j \geq 0, \tag{10}$$

where c_j is a parameter that weights the importance of each node j, v_j^{dq} are the dq voltages for harmonic h and r is the number of nodes ($j = 1,\ 2,\ ...,r$). This function thus minimizes the harmonic voltages at the MG nodes. Although constraints introduced in following subsections will limit the maximum allowed harmonic voltages in the MG nodes, the objective function aims at further reducing them so that their adverse impact is minimized.

The decision variables for the system are the harmonic voltages of the MG nodes, $\{v_1^d, v_1^q, ..., v_n^d, v_n^q\}$, and the equivalent virtual admittances of the DGs, $\{G_1^e, B_1^e, ..., G_m^e, B_m^e\}$. The complete optimization problem is given with the objective function presented in (10), and the constraints given in (12), (17), (19), (20), (23) and (24). These constraints are explained in the following subsections.

C. Constraints Based on Nodal Admittance Matrix

Kirchhoff's current law represents a physical constraint for the optimization problem. This constraint ensures that the harmonic voltages are accurately calculated. This can be expressed by using the nodal admittance matrix for a given harmonic. For the node in Fig. 5, this is given by:

$$\boldsymbol{Y}_j \boldsymbol{v}_j - \sum_{k \in K_j} \boldsymbol{Y}_{jk} \boldsymbol{v}_k + \boldsymbol{Y}_j^e \boldsymbol{v}_j = -\boldsymbol{i}_j \quad \forall j, \tag{11}$$

where K_j is the set of nodes connected to node j, $\boldsymbol{v}_j$ and $\boldsymbol{i}_j$ are the harmonic voltages and load currents in the dq frame at node j, while $\boldsymbol{Y}_j = \sum_{k \in K_j} \boldsymbol{Y}_{jk}$ is the sum of the admittances connecting to node j, excluding $\boldsymbol{Y}_j^e$. Note that the two first terms on the left-hand side are linear with respect to their unknowns, while the third term is quadratic (recall that $\boldsymbol{Y}_j^e$ and $\boldsymbol{v}_j$ are unknowns). In order to avoid using complex quantities in the optimization algorithm, (11) is specified in terms of its conductance and susceptance, as given in:

$$\begin{bmatrix} G_{jk} & -B_{jk} \\ B_{jk} & G_{jk} \end{bmatrix} \begin{bmatrix} v_j^d \\ v_j^q \end{bmatrix} - \sum_{k \in K_j} \begin{bmatrix} G_{jk} & -B_{jk} \\ B_{jk} & G_{jk} \end{bmatrix} \begin{bmatrix} v_k^d \\ v_k^q \end{bmatrix} + \begin{bmatrix} G_j^e & -B_j^e \\ B_j^e & G_j^e \end{bmatrix} \begin{bmatrix} v_j^d \\ v_j^q \end{bmatrix} = - \begin{bmatrix} i_j^d \\ i_j^q \end{bmatrix} \quad \forall j. \tag{12}$$

D. Constraints on DG Equivalent Impedance

If a DG is connected at node j, its equivalent impedance is given by:

$$Z_j^e = \frac{1}{Y_j^e} = \frac{1}{Y_j^p} + \frac{1}{Y_j^v} = Z_j^p + Z_j^v, \tag{13}$$

where Z_j^p and Z_j^v are the physical and virtual impedances of DG j, respectively. To ensure a positive equivalent resistance, it is necessary to fulfil $\Re(Z_j^e) > 0$. Since $Y_j^e = G_j^e + jB_j^e$, this requirement can be rewritten as:

$$\Re(Z_j^e) = \Re\left(\frac{1}{G_j^e + jB_j^e}\right) = \frac{G_j^e}{(G_j^e)^2 + (B_j^e)^2} > 0. \tag{14}$$

Clearly, (14) is fulfilled if $G_j^e > 0$. Therefore, in order to have a safety margin for this requirement, the equivalent resistance of the DG is restricted to be larger than a factor (α_h) times the physical resistance:

$$\Re(Z_j^e) \geq \Re(Z_j^{e,min}) = R_j^{min} = \alpha_h \frac{G_j^p}{(G_j^p)^2 + (B_j^p)^2}, \tag{15}$$

where R_j^{min} is the minimum allowed equivalent resistance for DG j. Then, the constraint can be derived from (15):

$$R_j^{min} \leq \Re(Z_j^e) = \frac{G_j^e}{(G_j^e)^2 + (B_j^e)^2}, \tag{16}$$

which can be rewritten as a quadratic constraint as follows:

$$-G_j^e + R_j^{min}(G_j^e)^2 + R_j^{min}(B_j^e)^2 \leq 0. \tag{17}$$

Similarly, by restricting the reactance of the equivalent impedance to be larger than a factor times the physical impedance, the following result is obtained:

$$\Im(Z_j^e) \geq X_j^{min} = \alpha_h \Im(Z_j^p), \tag{18}$$

which can be rewritten as a quadratic constraint as follows:

$$B_j^e + X_j^{min}((G_j^e)^2 + (B_j^e)^2) \leq 0. \tag{19}$$

E. Constraints for Voltage Harmonic Distortion

The harmonic voltage of the MG nodes should be less than a limit specified by the applicable standard (e.g. [2]). This can be easily incorporated with the following quadratic constraint:

$$(v_j^d)^2 + (v_j^q)^2 \leq (V_h^{max})^2 \qquad \forall j, \tag{20}$$

where V_h^{max} is the maximum voltage value for the harmonic component h.

F. Constraints for DG Current Harmonic Sharing

The harmonic current of DG j is given by:

$$\boldsymbol{i}_j^{DG} = \boldsymbol{Y}_j^e \boldsymbol{v}_j. \tag{21}$$

While imposing perfect current harmonic sharing reduces the risk of overloading any single DG, it could also lead to excessive voltage distortion. Moreover, it could generate excessive losses since harmonics would need to travel through the distribution lines. Therefore, a certain degree of sharing between the DGs has been specified. This has been modelled by using the following constraint:

$$(1-\beta)\frac{S_j}{S_{tot}}\sum_{k=1}^{l}\boldsymbol{i}_k^{DG} \leq \boldsymbol{i}_j^{DG} \leq (1+\beta)\frac{S_j}{S_{tot}}\sum_{k=1}^{l}\boldsymbol{i}_k^{DG} \;\forall j, \tag{22}$$

where l is the number of DGs, $\beta \in [0,\, 1]$ is a parameter to be chosen by the designer that specifies the degree of sharing, S_j is the rated capacity of DG j and $S_{tot} = \sum_{j=1}^{l} S_j$ is the sum of the rated capacities of all DGs. If $\beta = 0$, then (22) turn into equality constraints, which enforces DG current harmonic sharing according to the available capacity of each DG. The sharing according to capacity is specified by the fraction S_j/S_{tot}. By setting $\beta > 0$, (22) take the form of inequality constraints, thus allowing the DGs to have unequal current harmonic sharing. This will make the DG(s) closest to the harmonic loads inject more harmonic currents, thereby reducing the distribution losses [21].

In order to have only real values for the optimization, the quadratic constraints in (22) can be rewritten as:

$$(1-\beta)\frac{S_j}{S_{tot}}\sum_{k=1}^{m}\begin{bmatrix} G_k^e & -B_k^e \\ B_k^e & G_k^e \end{bmatrix}\begin{bmatrix} v_k^d \\ v_k^q \end{bmatrix} \leq \begin{bmatrix} G_j^e & -B_j^e \\ B_j^e & G_j^e \end{bmatrix}\begin{bmatrix} v_j^d \\ v_j^q \end{bmatrix} \quad \forall j, \tag{23}$$

$$\begin{bmatrix} G_j^e & -B_j^e \\ B_j^e & G_j^e \end{bmatrix}\begin{bmatrix} v_j^d \\ v_j^q \end{bmatrix} \leq (1+\beta)\frac{S_j}{S_{tot}}\sum_{k=1}^{m}\begin{bmatrix} G_k^e & -B_k^e \\ B_k^e & G_k^e \end{bmatrix}\begin{bmatrix} v_k^d \\ v_k^q \end{bmatrix} \quad \forall j. \tag{24}$$

IV. CASE STUDY RESULTS

A. Case Study System Description

The basic elements of the test system are depicted in Fig. 1 and the values of the main parameters are included in Table I. The following modifications were made to the original benchmark model so that simulation and experimental results are on a similar scale:

1) Only the three largest DGs in the benchmark were used. The ratings of the converters were set to 15 kVA.
2) Line impedances were balanced and scaled up by a factor of five to be comparable to the available impedances in the laboratory. The relative magnitudes between impedances were kept as in the benchmark.
3) Two types of loads were considered: A linear load with power factor of 0.85, and a nonlinear load based on a diode rectifier. The latter also had a dc-side LC-filter with values $L = 84$ μH and $C = 235$ μF. The relative magnitude between the loads were kept as in the benchmark.

TABLE I

MAIN SIMULATION PARAMETERS FOR THE SYSTEM UNDER STUDY

Parameter	**Value**	**Parameter**	**Value**
S_n	15 kVA	L_f	2.3 mH
V_n	400 V	R_f	0.1 Ω
f_n	50 Hz	C_f	8.8 µF
V_{dc}	680 V	L_o	0.9 mH
f_{sw}	10 kHz	R_o	0.03 Ω
m	5e-5 rad/s/W	T_f	0.1 s
n	1e-4 V/VAr	$Z_{R3,R4}$	$50 + j31$ mΩ
$Z_{R4,R6}$	$100 + j63$ mΩ	$Z_{R6,R9}$	$149 + j94$ mΩ
$Z_{R9,R10}$	$50 + j31$ mΩ	$Z_{R3,R11}$	$43 + j27$ mΩ
$Z_{R4,R15}$	$192 + j121$ mΩ	$Z_{R6,R16}$	$43 + j27$ mΩ
$Z_{R9,R17}$	$43 + j27$ mΩ	$Z_{R10,R18}$	$43 + j27$ mΩ

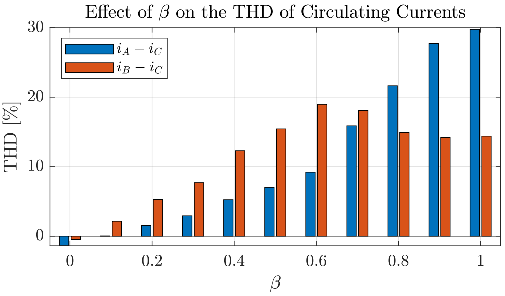

Fig. 6. THD of the circulating currents between DGA and DGC, and DGB and DGC, when the value of β is modified.

Simulations were done by using Matlab/Simulink and the SimPowerSystems toolbox. The simulation included realistic effects such as pulse width modulation (PWM) and the implementation of controllers in discrete time.

B. Steady-State Operation and Parameter Selection

In this section, the trade-off between harmonic sharing and voltage quality was explored for different values of β. From the theoretical point of view, this effect is summarized in the objective function (10), and in the constraints (23) and (24). For this scenario, all the nodes included linear loads, whereas nonlinear loads were applied at nodes R16 and R17.

Fig. 6 shows the THD of the currents that circulate between the DGs ($i_A - i_C$ and $i_B - i_C$) for different values of β. It can be seen that $\beta = 0$ leads to a very low THD value. This happens because the output currents of the DGs are very similar, meaning that current harmonics are accurately shared. This result is in good agreement with the constraint in (22), which forces equal harmonic sharing for $\beta = 0$.

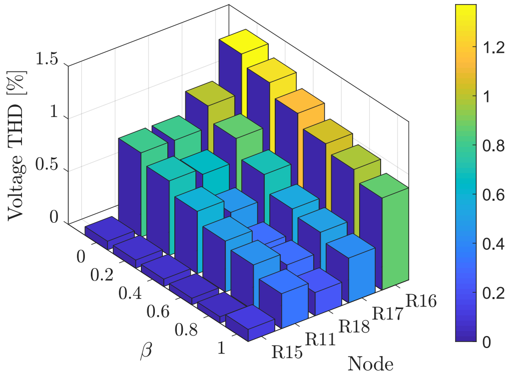

Fig. 7. THD value at representative nodes, for different values of β.

TABLE II
IMPEDANCE OF NONLINEAR (NL) AND LINEAR (L) LOADS AT THE SYSTEM NODES

Load	$t = 0$ s	$t = 1$ s	$t = 7$ s
$Z_{R11,nl}$	-	-	87.2Ω
$Z_{R15,l}$	$20.12 + j12.47\Omega$	$20.12 + j12.47\Omega$	$20.12 + j12.47\Omega$
$Z_{R16,l}$	$20.12 + j12.47\Omega$	$20.12 + j12.47\Omega$	$20.12 + j12.47\Omega$
$Z_{R16,nl}$	-	$36.98\,\Omega$	$25.89\,\Omega$
$Z_{R17,nl}$	-	$230.11\,\Omega$	$184.09\,\Omega$
$Z_{R18,l}$	$43.91 + j27.21\Omega$	$43.91 + j27.21\Omega$	$43.91 + j27.21\Omega$

If the value of β increases, it is evident that the THD of the circulating currents increases as well. This happens because the algorithm takes advantage of this degree of freedom to improve the voltage quality at the MG nodes. To highlight this feature, Fig. 7 shows the resulting voltage THD at representative nodes of the MG, for different values of β. Clearly, the voltage THD reaches its maximum value for $\beta = 0$, and it decreases for all nodes in the system as the parameter β increases. These results illustrate how the trade-off between current harmonic sharing and voltage quality can be easily adjusted by changing a single parameter (β) in the optimization algorithm.

C. Transient Performance and Parameter Update

In addition to the steady-state performance, the effect of load variations and changes in the VIs in the DGs was explored. To this end, different transient events were simulated for the MG depicted in Fig. 1. The load impedance values for the nonlinear (nl) and linear (l) loads are summarized in Table II. The timing of these events is as follows:

1) At $t = 0$ s, the simulation is started with linear loads connected at nodes R15, R16 and R18. The harmonic VIs are set to be equal to the fundamental VIs.
2) At $t = 1$ s, nonlinear loads are connected at nodes R16 and R17.
3) At $t = 4$ s, the proposed optimization algorithm is used to calculate a set-point for the harmonic VIs and the parameters are updated in the DGs. The optimization is done with $\beta = 0$, thus enabling equal sharing of the harmonic currents.
4) At $t = 7$ s, the nonlinear load is increased at nodes R11, R16 and R17.
5) At $t = 10$ s, the optimization algorithm is fed with the new data, and the new values of the VIs are calculated and updated in the DGs.
6) At $t = 13$ s, the optimization algorithm is executed again, but this time $\beta = 0.2$, thereby allowing some degree of freedom for unequal current harmonic sharing.

The resulting magnitudes of the harmonic currents for the three DGs are shown in Figs. 8(a)-(d), while the magnitude of harmonic voltages in percent of the base voltage are shown in Figs. 8(e)-(h).

As shown in Figs. 8(a)-(d), using the same value for the VIs at the fundamental and harmonic frequencies leads to an unequal distribution of the harmonic currents. Once the optimized harmonic VIs are calculated and updated at $t = 4$ s, the harmonic currents are accurately shared between the DGs. Moreover, the harmonic components of the voltage nodes also reduce. This occurs because the optimized VIs can be set much smaller than the fundamental VI, thereby reducing the equivalent impedance seen by the load harmonic current sources. After the load increase at $t = 7$ s, the current harmonic sharing is worsened. However, the relative differences between the harmonic currents are still small. Hence, even though the VI values are optimal for a specific operating condition, the design is robust against parameter variations. Naturally, the harmonic voltages at the MG nodes also increase as a result of the load increase. At $t = 10$ s, the optimization algorithm is executed again for the updated values of the operating point. As expected, the current is again shared between the DGs and the magnitude of the harmonic voltages is decreased significantly. At $t = 13$ s, the optimization algorithm is executed again, but this time for $\beta = 0.2$ to allow unequal current harmonic sharing. Fig. 8 shows that this selection clearly worsened the current harmonic sharing. However, the 5th, 7th and 13th voltage harmonics are greatly reduced, while the 11th harmonic is almost unaffected. Therefore, the overall voltage quality of the MG clearly improved.

D. Effect of Inaccurate Line Impedances in the Optimization

In practical applications, the line impedance values are not accurately known. Therefore, there will be a mismatch between the impedance values used for the optimization and the actual impedances. To study the possible effect of this, the transient simulation in Section IV-C was modified to include a random error of ±10 % in the line impedance values. The resulting harmonic currents and voltages are shown in Fig. 9. As the results were similar for all harmonics, only the results for the 5th harmonic are shown. It can be observed that the results are similar to those obtained with exact values. After applying the optimized set-points for the VIs at $t = 4$ s, the current sharing is significantly improved. However, compared to the original case, the differences are larger. The same occurs after the new set-points are applied at $t = 10$ s. When allowing for unequal current harmonic sharing at $t = 13$ s, a clear mismatch between the currents can be observed. Meanwhile, the harmonic voltages are generally reduced when optimized

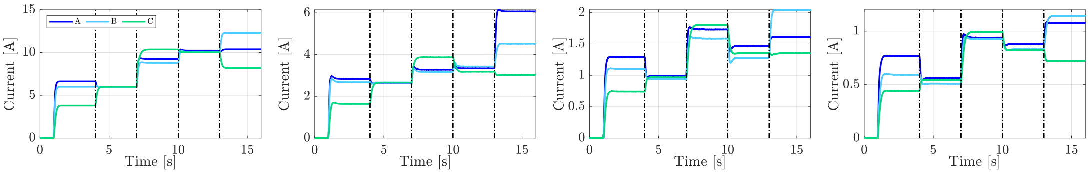

(a) 5th (b) 7th (c) 11th (d) 13th

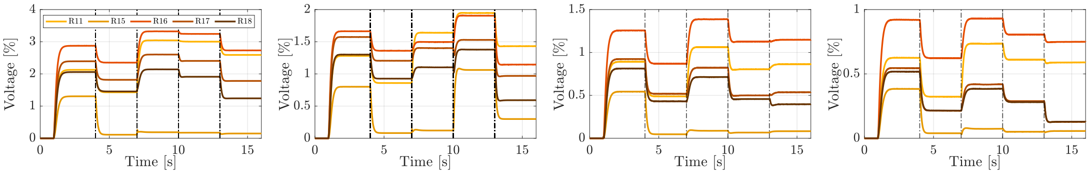

(e) 5th (f) 7th (g) 11th (h) 13th

Fig. 8. Transient performance of the MG together with the proposed optimization algorithm. (top) Harmonic currents for DGA, DGB and DGC. (bottom) Harmonic voltages for nodes R11, R15, R16, R17 and R18. The transient events are defined in Section IV-C.

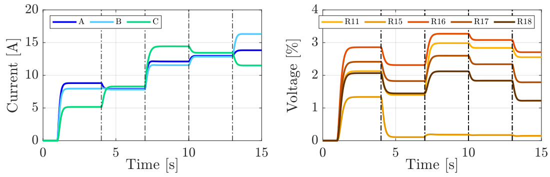

(a) 5th (b) 5th

Fig. 9. Transient performance of the MG. Inaccurate line impedance values are used in the optimization algorithm. (a) Harmonic currents for DGA, DGB and DGC. (b) Harmonic voltages for nodes R11, R15, R16, R17 and R18.

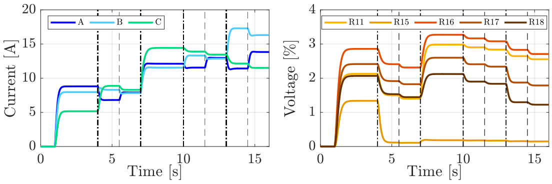

(a) 5th (b) 5th

Fig. 10. Transient performance of the MG. Inaccurate line impedance values are used in the optimization algorithm, and a time-delay in updating the VIs of DGA is added. (a) Harmonic currents for DGs A, B and C. (b) Harmonic voltages for nodes R11, R15, R16, R17 and R18.

VI values are used. This is particularly the case when allowing for unequal current sharing. These results show that the proposed method provides adequate results even if the values of the line impedances are not known accurately.

E. Effect of Time Delay in Communication Link

In previous subsections, the VIs were updated simultaneously for all DGs. However, in practical applications, these values are sent via communications and therefore they will be updated asynchronously. This effect will be studied here by adding a time delay in the communication channel. In particular, for the case presented in Section IV-D, an additional delay of 1.5 s will be added to the communications of DGA. As the delay effect was similar for all harmonics, only the results for the 5th harmonic will be presented.

The resulting DG harmonic sharing and selected node harmonic voltages are shown in Fig. 10. The dashed-dotted lines indicate the time instances when the VIs of DGB and DGC are updated. Meanwhile, the dashed lines indicate the times when the VIs of DGA are updated. By comparing Fig. 10 with Fig. 9, it is clear that the current is correctly shared when the VIs of all the DGs are updated. Also, the harmonic voltages are the same in steady state. In addition, it can be seen that the current sharing is improved even if the VIs are not updated for all the DGs.

V. EXPERIMENTAL VERIFICATION

The basic features of the proposed optimization algorithm were tested in the laboratory facilities of IMDEA Energy. Compared to the simulation case, some aspects were simplified in order to make the implementation viable. However, the results were kept in the same scale so that simulation and experimental results can be compared qualitatively.

A. Prototype Description

Fig. 11 presents an electrical schematic of the laboratory facilities. Two converters rated at 15 kVA and one rated at 75 kVA were used as DGs. Compared to the simulation results, one 15 kW converter was replaced with a 75 kW one. Otherwise, the MG was not able to withstand the sudden connection of the emulated loads. The dc sides of the DGs were kept constant at 680 V by using rectifiers with isolation transformers. All DGs were controlled as shown in Fig. 3. The dc-link capacitor values were 1 mF and 2 mF for the 15 and 75 kVA converters, respectively. Two resistive linear loads with a maximum rating of 30 kW were connected to nodes R15 and R10. In addition, mixed loads (including linear and nonlinear consumption) were emulated by using two 15 kVA converters and one 75 kVA converter. These were connected to nodes R4, R6 and R9. Emulated loads were connected to the grid by using isolation transformers,

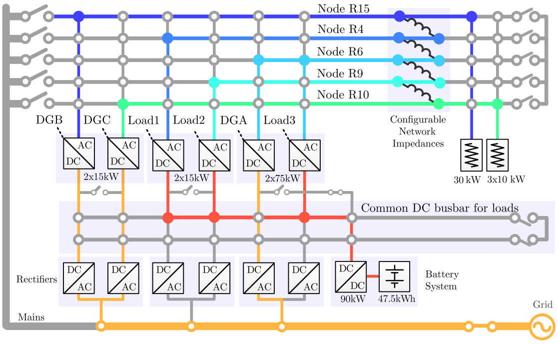

Fig. 11. Electrical schematic of the laboratory facilities. (red) Common-dc bus for loads, (yellow) isolated DC voltages for DGs and (blue and green tones) MG nodes.

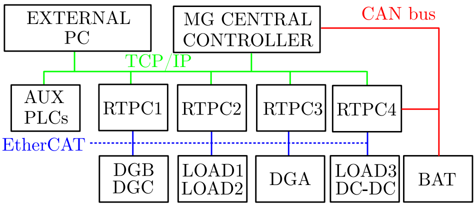

Fig. 12. Communication infrastructure of the laboratory facilities. (blue) EtherCAT, (green) TCP/IP and (red) CAN bus.

while their dc sides were connected by using a dc busbar. In order to consume power during the experiments, the dc voltage was maintained constant at 680 V by using a 90 kW dc-dc converter coupled to a Li-ion battery rated at 47.5 kW/h. This capacity was enough to run tests during several hours. The switching and sampling frequencies were set to 10 kHz and 8 kHz for the 15 kVA and 75 kVA converters, respectively. Pulse-width modulation (PWM) signals were generated by using the min-max method, and the dead-time was 2 μs. The control systems were implemented in embedded (real-time) computers NEXTCOM NISE3140.

Fig. 12 shows a schematic of the control and communication infrastructure of the laboratory facilities. The control of DGB and DGC was implemented in one real-time PC (RTPC), while the control of DGA was implemented in another RTPC. These RTPCs were connected to the VSCs via EtherCAT so that internal controllers were executed each sampling period. Also, they were connected to the laboratory network by using TCP/IP protocol. The battery was connected via CAN bus to the battery converter and the central controller. For extended details of the laboratory facilities, see [32].

B. *Implementation Aspects*

Even though simulations provided adequate and robust results, the practical implementation required several modifications to the original control scheme. These are listed here:

1) During the experiments, it was observed that stability of the resonant controllers was highly dependent on the operating conditions. Therefore, an automatic commissioning procedure was developed and executed before they were turned on. This procedure included an identification of the plant dynamics at the harmonic frequencies. In addition, a significant coupling between the dq components of the VIs was observed. Therefore, a decoupling system based on the identified plant dynamics was added to them.
2) The transient performance of the VIs was initially very fast. This produced unwanted oscillations that interacted with other elements in the MG (e.g. transformers). Therefore, low-frequency low-pass filters were included for the harmonic VIs.
3) The DGs were equipped with a soft-start sequence that allowed their connection and disconnection from the MG in a smooth way.
4) The droop controllers of DGs were adjusted by hand, according to the transient performance under load variations. Reactive power references were also adjusted by hand to avoid excessive circulating currents.
5) The values of the VIs were sent to the DGs via a TCP/IP network (not time synchronized). Therefore, their values were pre-calculated and sent to all the DGs at the same time.

C. *Experimental Results*

1) MG Operation Without VIs: The steady-state results for the tests are shown in Fig. 13 and Fig. 14. Fig. 14 (a) shows the waveforms of the phase-a output currents for the three DGs. The results were measured by using an oscilloscope. It can be seen that there are significant differences between them, especially for the current of DGA. The harmonic components of the output currents of the DGs and the voltage THD at the MG nodes can be found in Fig. 13 (left). The current harmonics consumed by DGA is much higher than DGB and DGC, mainly because DGA is located closer to the source of the harmonics. Also, the rating of the converter is higher (and then the physical impedance values are lower). There are more harmonic components in the output currents than expected because some of them were produced in transformers and other non-ideal hardware elements of the MG. Also, these additional currents increased the theoretical THD values, which are higher than the expected ones.

2) MG Operation for $\beta = 0$ and $\beta = 0.2$: The MG operation was also tested with the proposed VIs. In this case, the VIs were calculated offline, since the laboratory facilities were not adequate for calculating and updating the VIs through a time-critical communication channel. Fig. 13 (top) shows the harmonic content of the DGs output currents for (centre) $\beta = 0.2$ and (right) $\beta = 0$. Similarly, Fig. 13 (bottom) shows the THD at the MG nodes that were accessible. It can be seen that the general trend of the results is as expected. For $\beta = 0$, the harmonic current distribution is greatly improved compared to the case without VIs. Meanwhile, the THD at the MG nodes increased as a consequence of the power quality trade-off. These results highlight that the proposed control strategy provides adequate results. However, some aspects that are not commonly modelled in this type of research studies

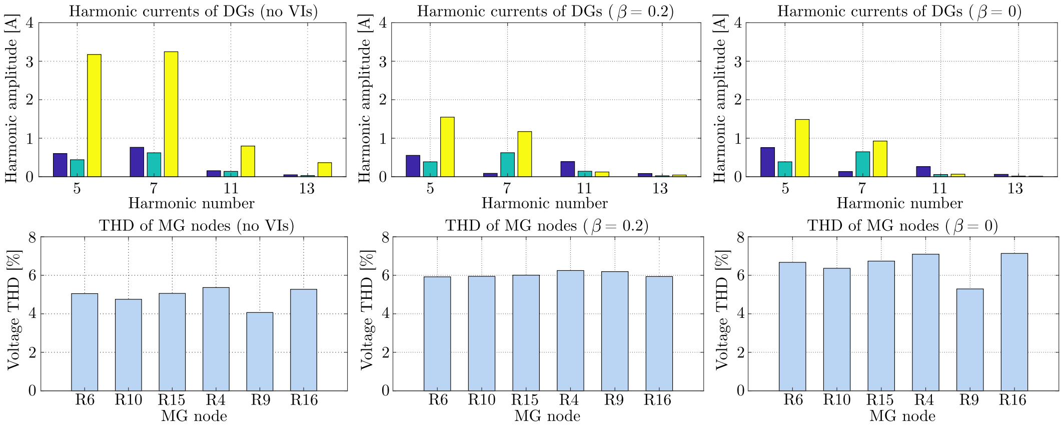

Fig. 13. (top) Current harmonics delivered by the DGs and (bottom) THD at accessible MG nodes. (left) No VIs, (centre) $\beta = 0.2$ and (right) $\beta = 0$. In the top, (blue) DGB, (green) DGC and (yellow) DGA.

(a) Output currents, no virtual impedaces

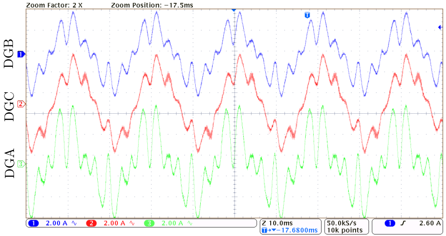

(b) Output currents, virtual impedances, $\beta = 0.2$

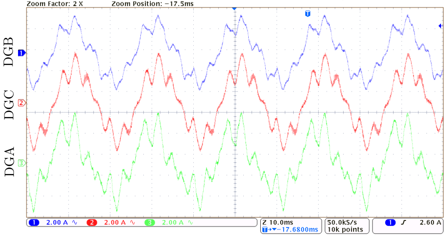

(c) Output currents, virtual impedances, $\beta = 0$

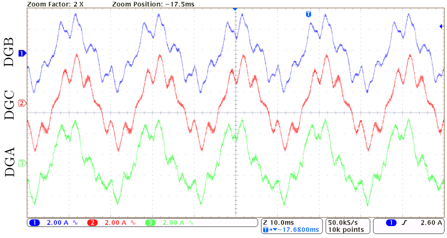

Fig. 14. Phase a output current for (blue) DGB, (red) DGC and (green) DGA. (a) Without VIs, and with VIs for (b) $\beta = 0.2$ and (c) $\beta = 0$.

(e.g. transformers and nonlinear sources of harmonics) should be considered in order to obtain more accurate results.

3) Transient Response of a DG with VIs: Fig. 15 shows the transient response of DGC variables when the VIs of that DG were turned on. The rest of the DGs were connected. In that instant, the current harmonics decreased, and their transient responses experienced overshoots. The voltage THD and the frequency of the DG slightly increased. The transient response of the harmonics was slower compared to the simulations since additional low-pass filters were used for the implementation.

4) Updating the VIs via Communications: In this section, the effect of updating the VIs on the entire system is explored. Fig. 16 shows the results obtained in the laboratory. The timing of the events is as follows:

1) At $t = 0$ s, the test starts. All the DGs and loads are connected. However, the VIs are not enabled.
2) At $t = 5$ s, the VIs calculated for $\beta = 0$ are sent via communications to the DGs. When the values are received, they are immediately updated in the controllers.
3) At $t = 14$ s, DGC is disconnected.
4) At $t = 20$ s, a new set of VIs is sent via communications to DGA and DGB.

The values of the VIs used for the experiments were pre-calculated and stored in the central PC. The resulting magnitudes of the harmonic currents for the three DGs are shown in Figs. 16(a)-(d), while the voltage THDs at the connection points are shown in Fig. 16(e).

Initially, the VIs were disconnected. Therefore, the currents were not distributed equally between the DGs. When the VIs were sent via communications to the DGs, the current harmonics were redistributed and the sharing improved with respect to the case without VIs. However, the current harmonic sharing was not perfect due the realistic elements of the laboratory facilities. As expected, the THD of the connection nodes increased due to the improved sharing. At $t = 14$ s DGC was disconnected, and therefore the harmonics were redistributed again between the remaining DGs. The voltage THDs also increased. Then, at $t = 20$ s, the new VIs were sent to DGA and DGB. For the 5th and 7th harmonic, the current sharing greatly improved, while the THD was maintained almost at the same level. The 11th and 13th harmonics were almost unaffected compared to the previous state.

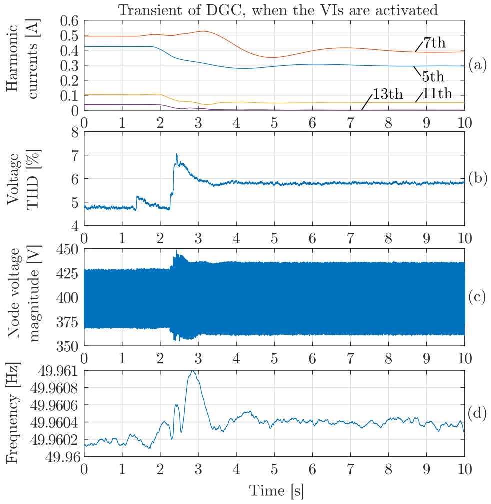

Fig. 15. Transient response of DGC when the VIs are turned on. (a) Current harmonics, (b) THD of the connection point, (c) voltage module at the connection point and (d) frequency of the DG.

VI. Discussion

A. Assumption of Known Line Impedances

One of the basic assumptions for the proposed method is that the MG topology and line impedance values are assumed to be known. Although this is a drawback for the method, this information is also needed for several system level functions [33, 34]. Moreover, this information has been used in similar MG applications [24]. In practical applications, the line impedances can be readily estimated when the type of conductor and the cable length is known [28], or more advanced methods on estimating the line impedances can be performed [35]. However, as shown in Section IV-D, the proposed method performs adequately despite having inaccurate knowledge of the line impedances.

B. Scalability of the Proposed Method

The computational and communication requirements as well as the optimization algorithm itself should be considered when discussing the scalability of the proposed method. The method in this paper targets improving the power quality in steady state. This makes sense in practical applications, as harmonics are measured based on average values over longer time intervals (e.g. 10 min for EN50160 [2]). Since the goal is to improve the power quality in steady state, the optimization at the MGCC is not time critical. Meanwhile, the harmonic load current measurements should be time synchronized. This is important irrespective of the size of the MG. Therefore, this does not affect the scalability of the proposed method. However, it should be noted that solving the optimization problem and updating the harmonic VIs are not time critical. Hence, the computational and communication requirements for the MGCC are low.

The scalability of the proposed optimization program largely depends on the type of program. It can be shown that the proposed algorithm is a quadratically constrained quadratic program (QCQP) [36]. Moreover, the proposed algorithm is convex. Clearly, this does not scale as well as linear programs. However, it scales adequately when the grid size is not excessive.

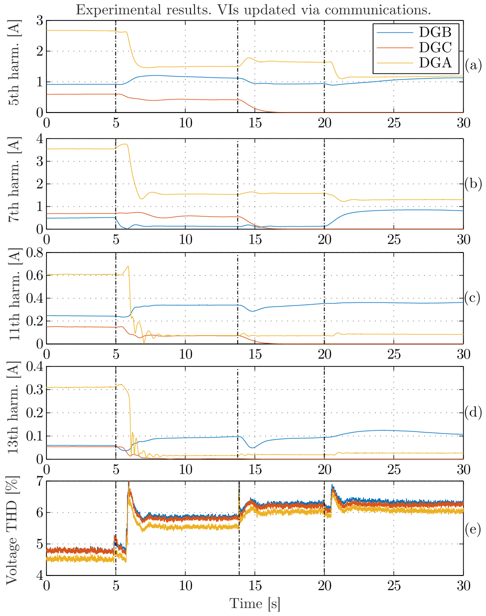

Fig. 16. VIs updated via communications in DGA, DGB and DGC. The VIs were readjusted so that the sharing is almost equal. Current harmonic (a) 5th, (b) 7th, (c) 11th and (d) 13th. (e) Voltage THDs.

VII. Conclusion

In this paper, an optimization algorithm for setting the harmonic virtual impedances of DGs in a multibus MG has been presented. The objective function minimized the harmonic voltages at selected nodes, while a degree of current harmonic sharing between the DGs was included as one of the constraints. With the algorithm, both the sharing between DG units and voltage quality can be improved at the same time and the power quality trade-off can be easily adjusted. Theoretical, simulation and experimental results were used to validate the main contributions of this work.

Theoretical results showed that power quality can be easily managed by changing the parameter β. It was shown that $\beta = 0$ provided accurate sharing of current harmonics. However, the voltage quality was worsened. As the value of β increased, the sharing of current harmonics was less accurate, but this gave degrees of freedom to greatly improve the voltage quality. Simulation results verified the theoretical developments. Also, it was shown that the values of the VIs can be modified without noticeable problems. Finally, the main contributions of the work were tested in an experimental platform. It was shown that the proposed VIs provided improvements in the harmonic sharing. However, the laboratory implementation required a number of modifications to achieve an adequate performance. In particular, it was difficult to guarantee the system stability under any operating conditions, so harmonic controllers needed to be adapted for each specific case. Also, it was noticed that unmodelled sources of harmonics (such as transformers and dead-time effects) can lead to significant modifications of the expected results.

REFERENCES

[1] *IEEE Recommended Practice and Requirements for Harmonic Control in Electric Power Systems.* IEEE Std. 519-2014, 2014.

[2] *Voltage Characteristics of Electricity Supplied by Public Electricity Networks.* CENELC Standard EN 50160:2010, 2010.

[3] *IEEE Standard for Interconnection and Interoperability of Distributed Energy Resources with Associated Electric Power Systems Interfaces.* IEEE Std 1547-2018, 2018.

[4] D. E. Olivares, A. Mehrizi-Sani, A. H. Etemadi, C. A. Cañizares, R. Iravani, M. Kazerani, A. H. Hajimiragha, O. Gomis-Bellmunt, M. Saeedifard, R. Palma-Behnke, G. A. Jiménez-Estévez, and N. D. Hatziargyriou, "Trends in microgrid control," *IEEE Transactions on Smart Grid*, vol. 5, no. 4, pp. 1905–1919, 2014.

[5] M. C. Chandorkar, D. M. Divan, and R. Adapa, "Control of Parallel Connected Inverters in Standalone ac Supply Systems," *IEEE Transactions on Industry Applications*, vol. 29, no. 1, pp. 136–143, 1993.

[6] T. L. Lee and P. T. Cheng, "Design of a New Cooperative Harmonic Filtering Strategy for Distributed Generation Interface Converters in an Islanding Network," *IEEE Transactions on Power Electronics*, vol. 22, no. 5, pp. 1919–1927, 2007.

[7] H. Moussa, A. Shahin, J. P. Martin, B. Nahid-Mobarakeh, S. Pierfederici, and N. Moubayed, "Harmonic Power Sharing with Voltage Distortion Compensation of Droop Controlled Islanded Microgrids," *IEEE Transactions on Smart Grid*, vol. 9, no. 5, pp. 5335–5347, 2018.

[8] J. He, Y. W. Li, and M. S. Munir, "A flexible harmonic control approach through voltage-controlled DG-grid interfacing converters," *IEEE Transactions on Industrial Electronics*, vol. 59, no. 1, pp. 444–455, 2012.

[9] M. Savaghebi, A. Jalilian, J. C. Vasquez, and J. M. Guerrero, "Secondary Control for Voltage Quality Enhancement in Microgrids," *IEEE Transactions on Smart Grid*, vol. 3, no. 4, p. 4799, 2012.

[10] L. Meng, F. Tang, M. Savaghebi, J. C. Vasquez, and J. M. Guerrero, "Tertiary control of voltage unbalance compensation for optimal power quality in islanded microgrids," *IEEE Transactions on Energy Conversion*, vol. 29, no. 4, pp. 802–815, 2014.

[11] X. Zhao, L. Meng, C. Xie, J. M. Guerrero, and X. Wu, "A Unified Voltage Harmonic Control Strategy for Coordinated Compensation with VCM and CCM Converters," *IEEE Transactions on Power Electronics*, vol. 33, no. 8, pp. 7132–7147, 2018.

[12] X. Wang, Y. W. Li, F. Blaabjerg, and P. C. Loh, "Virtual-Impedance-Based Control for Voltage-Source and Current-Source Converters," *IEEE Transactions on Power Electronics*, vol. 30, no. 12, pp. 7019–7037, 2015.

[13] D. De and V. Ramanarayanan, "Decentralized parallel operation of inverters sharing unbalanced and nonlinear loads," *IEEE Transactions on Power Electronics*, vol. 25, no. 12, pp. 3015–3025, 2010.

[14] U. Borup, F. Blaabjerg, and P. N. Enjeti, "Sharing of nonlinear load in parallel-connected three-phase converters," *IEEE Transactions on Industry Applications*, vol. 37, no. 6, pp. 1817–1823, 2001.

[15] T. Vandoorn, B. Meersman, J. De Kooning, and L. Vandevelde, "Controllable harmonic current sharing in islanded microgrids: DG units with programmable resistive behavior toward harmonics," *IEEE Transactions on Power Delivery*, vol. 27, no. 2, pp. 831–841, 2012.

[16] J. Guerrero, J. Matas, L. Garcia de Vicuna, M. Castilla, and J. Miret, "Wireless-Control Strategy for Parallel Operation of Distributed-Generation Inverters," *IEEE Transactions on Industrial Electronics*, vol. 53, no. 5, pp. 1461–1470, 2006.

[17] X. Wang, F. Blaabjerg, and Z. Chen, "Autonomous Control of Inverter - Interfaced Distributed Generation Units for Harmonic Current Filtering and Resonance Damping in an Islanded Microgrid," *IEEE Transactions on Industry Applications*, vol. 50, no. 1, pp. 452–461, 2014.

[18] F. Göthner, O.-M. Midtgård, R. Torres-Olguin, and J. Roldan-Perez, "Virtual Impedance Design for Power Quality and Harmonic Sharing Improvement in Microgrids," in *2019 20th Workshop on Control and Modeling for Power Electronics (COMPEL)*, 2019.

[19] T. V. Hoang and H. Lee, "Virtual impedance control scheme to compensate for voltage harmonics with accurate harmonic power sharing in islanded microgrids," *IEEE Journal of Emerging and Selected Topics in Power Electronics*.

[20] M. Savaghebi, Q. Shafiee, J. C. Vasquez, and J. M. Guerrero, "Adaptive Virtual Impedance Scheme for Selective Compensation of Voltage Unbalance and Harmonics in Microgrids," in *2015 IEEE Power & Energy Society General Meeting*, 2015.

[21] C. Blanco, D. Reigosa, J. C. Vasquez, J. M. Guerrero, and F. Briz, "Virtual Admittance Loop for Voltage Harmonic Compensation in Microgrids," *IEEE Transactions on Industry Applications*, vol. 52, no. 4, pp. 3348–3356, 2016.

[22] S. Y. M. Mousavi, A. Jalilian, M. Savaghebi, and J. M. Guerrero, "Autonomous Control of Current-and Voltage-Controlled DG Interface Inverters for Reactive Power Sharing and Harmonics Compensation in Islanded Microgrids," *IEEE Transactions on Power Electronics*, vol. 33, no. 11, pp. 9375–9386, 2018.

[23] H. R. Baghaee, M. Mirsalim, G. B. Gharehpetian, and H. A. Talebi, "Unbalanced harmonic power sharing and voltage compensation of microgrids using radial basis function neural network-based harmonic power-flow calculations for distributed and decentralised control structures," *IET Generation, Transmission and Distribution*, vol. 12, no. 7, pp. 1518–1530, 2017.

[24] L. Meng and J. M. Guerrero, "Optimization for Customized Power Quality Service in Multibus Microgrids," *IEEE Transactions on Industrial Electronics*, vol. 64, no. 11, pp. 8767–8777, 2017.

[25] M. M. Hashempour, T. L. Lee, M. Savaghebi, and J. M. Guerrero, "Real-time supervisory control for power quality improvement of multi-area microgrids," *IEEE Systems Journal*, vol. 13, no. 1, pp. 864–874, 2019.

[26] R. Keypour, B. Adineh, M. H. Khooban, and F. Blaabjerg, "A New Population-Based Optimization Method for Online Minimization of Voltage Harmonics in Islanded Microgrids," *IEEE Transactions on Circuits and Systems II: Express Briefs*, vol. 67, no. 6, pp. 1084–1088, 2020.

[27] E. H. Watanabe, R. M. Stephan, and M. Aredes, "New Concepts of Instantaneous Active and Reactive Powers in Electrical Systems With Generic Loads," *IEEE Transactions on Power Delivery*, vol. 8, no. 2, 1993.

[28] K. Strunz *et al.*, "Benchmark Systems for Network Integration of Renewable and Distributed Energy Resources," Task Force C6, CIGRE, Tech. Rep., 2014.

[29] J. Rocabert, A. Luna, F. Blaabjerg, and P. Rodríguez, "Control of Power Converters in AC Microgrids," *IEEE Transactions on Power Electronics*, vol. 27, no. 11, pp. 4734–4749, 2012.

[30] J. Roldán-Pérez, A. Rodríguez-Cabero, M. Ochoa-Giménez, A. García-Cerrada, and J. L. Zamora-Macho, "Discrete-time resonant controllers design for power conditioning applications," *Electric Power Systems Research*, vol. 164, pp. 31–38, 2018.

[31] J. M. Guerrero, L. G. Vicuña, J. Matas, M. Castilla, and J. Miret, "Output impedance design of parallel-connected UPS inverters with wireless load sharing control," *IEEE Transactions on Industrial Electronics*, vol. 52, no. 4, pp. 1126–1135, 2005.

[32] F. Huerta, J. K. Gruber, M. Prodanovic, and P. Matatagui, "Power-hardware-in-the-loop test beds: Evaluation tools for grid integration of distributed energy resources," *IEEE Industry Applications Magazine*, vol. 22, no. 2, pp. 18–26, 2016.

[33] Y. Levron, J. M. Guerrero, and Y. Beck, "Optimal power flow in microgrids with energy storage," *IEEE Transactions on Power Systems*, vol. 28, no. 3, pp. 3226–3234, 2013.

[34] D. Shi, C. Jin, Z. Zhang, F. H. Choo, K. L. Hai, and P. Wang, "Implementation of hardware-in-the-loop simulation workbench for a hybrid AC/DC microgrid," *2017 IEEE Power and Energy Society Innovative Smart Grid Technologies Conference, ISGT 2017*, 2017.

[35] S. Han, D. Kodaira, S. Han, B. Kwon, Y. Hasegawa, and H. Aki, "An Automated Impedance Estimation Method in Low-Voltage Distribution Network for Coordinated Voltage Regulation," *IEEE Transactions on Smart Grid*, vol. 7, no. 2, pp. 1012–1020, 2016.

[36] S. Boyd and L. Vandenberghe, *Convex Optimization.* Cambridge University Press, 2004.

Fredrik Göthner was born in Oslo, Norway, in 1992. He received the M.Sc. degree in electrical power engineering in 2017 from the Norwegian University of Science and Technology (NTNU), Trondheim, Norway, where he is currently working toward the Ph.D. degree on the control of converters in microgrids. His main research interests include control of power electronics and issues related to stability and power quality in microgrids.

Raymundo E. Torres-Olguin received the B.Sc. degree in electromechanical engineering from the University of San Luis Potosí, Mexico, in 2004, M.Sc. degree in control and dynamical systems from the Applied Mathematics Department, Research Institute of Science and Technology of San Luis Potosí (IPICYT), Mexico, in 2006, and Ph.D. degree in electric power engineering from the Norwegian University of Science and Technology (NTNU), Norway, in 2013. From 2012, he has worked as a research scientist in SINTEF Energy Research located in Trondheim, Norway. His main research interest includes control of power electronics for the integration of renewable resources, dc transmission and microgrids.

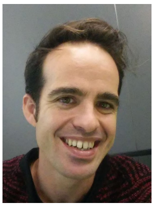

Javier Roldán-Pérez (S'12-M'14) received a B.S. degree in industrial engineering, a M.S. degree in electronics and control systems, a M.S. degree in system modeling, and a Ph.D. degree in power electronics, all from Comillas Pontifical University, Madrid, in 2009, 2010, 2011, and 2015, respectively. From 2010 to 2015, he was with the Institute for Research in Technology (IIT), Comillas University. In 2014, he was a visiting Ph.D. student at the Department of Energy Technology, Aalborg University, Denmark. From 2015 to 2016 he was with the Electric and Control Systems Department at Norvento Energía Distribuida. In September 2016 he joined the Electrical Systems Unit at IMDEA Energy Institute. In 2018, he did a research stay at SINTEF Energy Research, Trondheim. His research topics are the integration of renewable energies, microgrids, and power electronics applications.

Ole-Morten Midtgård (M'03) was born in Tromsø, Norway, in 1967. He received the M.Sc. and Ph.D. degrees in Electric Power Engineering from the Norwegian University of Science and Technology (NTNU), Trondheim, Norway, in 1992 and 1997, respectively. He is currently Head of Department at NTNU's Department of Electric Power Engineering, where he has been a Professor since 2012. Previous employments include 5 years at ABB and 8 years tenure at the University of Agder, Grimstad, Norway. Prof. Midtgård is an elected member of the Norwegian Academy of Technological Sciences (NTVA) and of Agder Academy of Sciences and Letters. He has broad research interests, which in addition to power electronics include electromagnetic computations, and applications such as microgrids, integration of PV in smart grids, and electric aviation.

Appendices

Appendix A

Complete Description of Optimization Algorithm

In this section, the detailed optimization algorithm presented in Section 3.3 is presented. First, the notation will be introduced. Subsequently, the objective function and the constraints will be given.

A.1 Notation and Algorithm Overview

In the following description, matrices are uppercase and in boldface, with uppercase elements. Vectors are lowercase and in boldface, with lowercase elements. To describe the notation, consider the electrical diagram of a generic node j in Fig. A.1. Each node is connected to at least one other node. Here, node j is connected to nodes k and l via the line admittances $\boldsymbol{Y}_{jk}$ and $\boldsymbol{Y}_{jl}$. Any loads connected to the node are aggregated and represented by the current source $\boldsymbol{i}_j$. Any DGs connected to the node are modeled by an equivalent admittance ($\boldsymbol{Y}_j^e$). This consists of a series connection of a virtual and physical admittance, respectively denoted as $\boldsymbol{Y}_j^v$ and $\boldsymbol{Y}_j^p$. The equivalent admittance is included as a decision variable and finding its optimal value is the main goal of the algorithm.

The optimization algorithm is run for each harmonic addressed by virtual impedances. However, the notation is simplified by omitting superscript h in the formulation of the optimization algorithm.

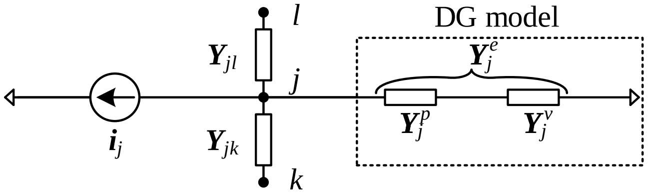

Figure A.1: General node used for the optimization, including a DG, load, and interconnecting line admittances.

A.2 Optimization Problem Formulation

The main objective is set to minimize the harmonic voltage at the microgrid nodes. Mathematically, this is expressed by the following objective function:

$$\min \sum_{j=1}^{r} c_j \left((v_j^d)^2 + (v_j^q)^2 \right), \quad c_j \geq 0, \tag{A.1}$$

where c_j is a parameter, v_j^{dq} are the dq voltages for harmonic h at node j, and r is the number of nodes ($j = 1,\ 2,\ ...,\ r$). The parameter c_j can be used to weight the importance of each node j, in case any node(s) have stricter requirements on the voltage quality.

In addition to the equivalent admittances of the DGs, the harmonic voltages of the microgrid nodes form the decision variables for the algorithm. The complete optimization program is given by the objective function presented in (A.1), and the constraints given in (A.3), (A.8), (A.9), (A.10), (A.13), and (A.14). In the following, the constraints are explained.

A.2.1 Constraints Based on Nodal Admittance Matrix

The first constraint is given by Kirchhoff's current law, which represents a physical restriction. For the node in Fig. A.1, this is given by:

$$\boldsymbol{Y}_j \boldsymbol{v}_j - \sum_{k \in K_j} \boldsymbol{Y}_{jk} \boldsymbol{v}_k + \boldsymbol{Y}_j^e \boldsymbol{v}_j = -\boldsymbol{i}_j \quad \forall j, \tag{A.2}$$

where K_j is the set of nodes connected to node j, $\boldsymbol{v}_j$ and $\boldsymbol{i}_j$ are the harmonic voltages and load currents in the dq frame at node j, while $\boldsymbol{Y}_j = \sum_{k \in K_j} \boldsymbol{Y}_{jk}$ is the sum of the admittances connecting to the node, excluding $\boldsymbol{Y}_j^e$. Since both $\boldsymbol{Y}_j^e$ and $\boldsymbol{v}_j$ are decision variables, the third term in A.2 is quadratic. To avoid the use of complex quantities in the algorithm, the constraint can be rewritten as follows:

$$\begin{bmatrix} G_{jk} & -B_{jk} \\ B_{jk} & G_{jk} \end{bmatrix} \begin{bmatrix} v_j^d \\ v_j^q \end{bmatrix} - \sum_{k \in K_j} \begin{bmatrix} G_{jk} & -B_{jk} \\ B_{jk} & G_{jk} \end{bmatrix} \begin{bmatrix} v_k^d \\ v_k^q \end{bmatrix} + \begin{bmatrix} G_j^e & -B_j^e \\ B_j^e & G_j^e \end{bmatrix} \begin{bmatrix} v_j^d \\ v_j^q \end{bmatrix} = - \begin{bmatrix} i_j^d \\ i_j^q \end{bmatrix} \quad \forall j. \tag{A.3}$$

A.2.2 Constraints on DG Equivalent Impedance

The equivalent impedance of a DG connected at node j is given by:

$$Z_j^e = \frac{1}{Y_j^e}. \tag{A.4}$$

A positive equivalent resistance can be ensured by enforcing $\Re(Z_j^e) > 0$. With $Y_j^e = G_j^e + jB_j^e$, this requirement can thus be rewritten as:

$$\Re(Z_j^e) = \Re\left(\frac{1}{G_j^e + jB_j^e}\right) = \frac{G_j^e}{(G_j^e)^2 + (B_j^e)^2} > 0. \tag{A.5}$$

Hence, $G_j^e > 0$ is necessary and sufficient for fulfilling this requirement. A safety margin can be added to this requirement by restricting the equivalent resistance of the DG to be larger than a factor (α_h) times the physical resistance:

$$\Re(Z_j^e) \geq \Re(Z_j^{e,min}) = R_j^{min} = \alpha_h \frac{G_j^p}{(G_j^p)^2 + (B_j^p)^2}. \tag{A.6}$$

where R_j^{min} is the minimum allowed equivalent resistance for DG j. The final constraint can then be derived from (A.6) as:

$$R_j^{min} \leq \Re(Z_j^e) = \frac{G_j^e}{(G_j^e)^2 + (B_j^e)^2}, \tag{A.7}$$

which can be rewritten as the following quadratic constraint:

$$-G_j^e + R_j^{min}(G_j^e)^2 + R_j^{min}(B_j^e)^2 \leq 0. \tag{A.8}$$

By similarly restricting the reactance of the equivalent impedance, the following quadratic constraint can be obtained:

$$B_j^e + X_j^{min}((G_j^e)^2 + (B_j^e)^2) \leq 0. \tag{A.9}$$

where $X_j^{min} = \alpha_h \Im(Z_j^p)$.

A.2.3 Constraints for Voltage Harmonic Distortion

Limits on harmonic voltages are specified by standards (e.g. EN50160). This can be included with the following quadratic constraint.

$$(v_j^d)^2 + (v_j^q)^2 \leq (V_h^{max})^2 \qquad \forall j, \tag{A.10}$$

where V_h^{max} is the maximum voltage value for the harmonic component h.

A.2.4 Constraints for DG Current Harmonic Sharing

One of the main features of the proposed optimization algorithm is that it ensures a certain degree of current harmonic sharing. This constraint will be described here. The harmonic current of DG j can be written as

$$\boldsymbol{i}_j^{DG} = \boldsymbol{Y}_j^e \boldsymbol{v}_j. \tag{A.11}$$

A certain degree of current harmonic sharing can be enforced with the following constraint:

$$(1-\beta)\frac{S_j}{S_{tot}}\sum_{k=1}^{l}\boldsymbol{i}_k^{DG} \leq \boldsymbol{i}_j^{DG} \leq (1+\beta)\frac{S_j}{S_{tot}}\sum_{k=1}^{l}\boldsymbol{i}_k^{DG} \quad \forall j, \tag{A.12}$$

where l is the number of DGs, $\beta \in [0,\ 1]$ is a parameter that specifies the degree of sharing, S_j is the rated capacity of DG j, and $S_{tot} = \sum_{j=1}^{l} S_j$ is the sum of the rated capacities of all DGs. Having $\beta = 0$ forces sharing of the harmonic current according to the capacity of each DG, which is given by S_j/S_{tot}. Meanwhile, allowing $\beta > 0$ implies a degree of freedom resulting from unequal current harmonics between the DGs.

To avoid complex quantities in the optimization algorithm, (A.12) can be reformulated as the following quadratic constraints:

$$(1-\beta)\frac{S_j}{S_{tot}}\sum_{k=1}^{m}\begin{bmatrix} G_k^e & -B_k^e \\ B_k^e & G_k^e \end{bmatrix}\begin{bmatrix} v_k^d \\ v_k^q \end{bmatrix} \leq \begin{bmatrix} G_j^e & -B_j^e \\ B_j^e & G_j^e \end{bmatrix}\begin{bmatrix} v_j^d \\ v_j^q \end{bmatrix} \quad \forall j, \tag{A.13}$$

$$\begin{bmatrix} G_j^e & -B_j^e \\ B_j^e & G_j^e \end{bmatrix}\begin{bmatrix} v_j^d \\ v_j^q \end{bmatrix} \leq (1+\beta)\frac{S_j}{S_{tot}}\sum_{k=1}^{m}\begin{bmatrix} G_k^e & -B_k^e \\ B_k^e & G_k^e \end{bmatrix}\begin{bmatrix} v_k^d \\ v_k^q \end{bmatrix} \quad \forall j. \tag{A.14}$$

Appendix B

Laboratory Facilities

The experimental verification was mainly performed at the National Smart Grid Laboratory (NSGL) at NTNU, but the Smart Energy Integration Lab (SEIL) at IMDEA Energy was also used. In the following, an overview of these laboratory facilities is presented.

B.1 National Smart Grid Laboratory

The NSGL is a versatile laboratory for the research and development of a variety of Smart Grid applications. A schematic diagram of the laboratory is seen in Fig. B.1. The thick black lines represent ac busbars, whereas the thick blue lines represent dc busbars. The ac busbars can be connected to the main grid or a model grid. As the laboratory contains a large amount of equipment, only the parts relevant to the thesis will be described in the following.

The main equipment needed for the tests were:

- *Two 60 kVA ac-dc Converters:* Two 2-level converters were used to validate the control scheme in paper I and the model in paper II. The converters are fitted with LCL filters and were connected to the busbars through delta-wye transformers with a turns ratio of 1.

- *200 kVA Power Amplifier:* The block denoted as EGSTON is a power amplifier with a bandwidth of 5 kHz. It has six outputs that can be configured in several ways. For the experiments in this thesis, it was used to provide a constant dc voltage to the converters. In addition, it served as the current-controlled voltage source converter to identify the system dynamics in paper I.

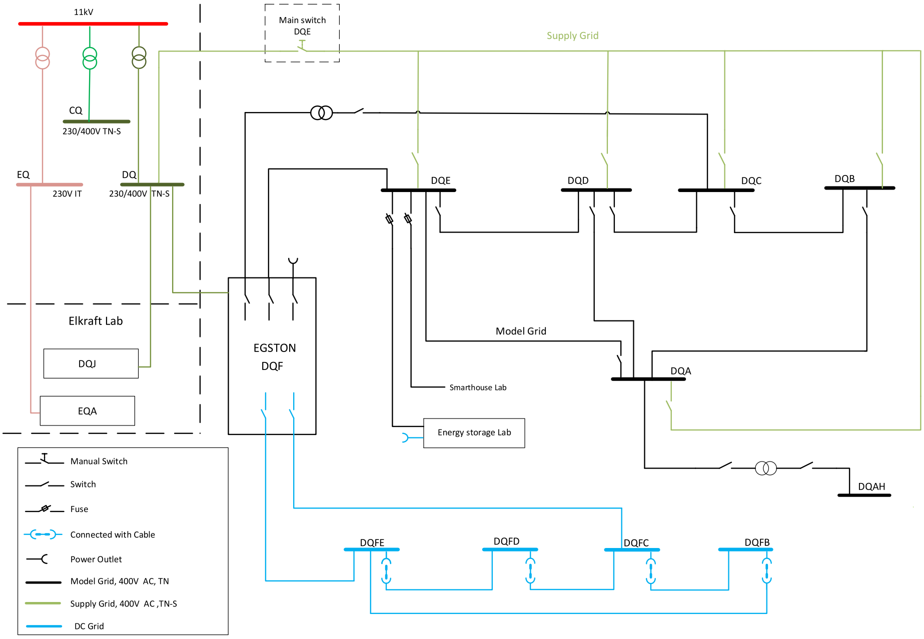

Figure B.1: Overview of the NSGL.

- *Electrical Lines and Loads:* Electrical lines were emulated by using external impedances, while a load bank was emulated by using a passive load rated at 20 kW.

The control of the converters and the EGSTON was implemented in Simulink and executed on an OP5600 real-time simulator by OPAL-RT. The communication was accomplished using a high-speed optical fiber bus.

B.2 Smart Energy Integration Lab

The SEIL is located at IMDEA Energy Institute, Móstoles, Madrid, Spain [93]. The laboratory can be used to emulate complex grid scenarios including primary, secondary and tertiary control levels. The laboratory includes hardware elements (converters, batteries, etc.) and control devices. The different technologies that form an electrical grid (PV, wind, electrical rotating machines, etc.) are emulated by using power-hardware-in-the-loop (PHIL) techniques or dedicated devices whenever possible. The laboratory topology can be easily reconfigured from a central computer so that manual modifications are avoided. The laboratory was used in validating the findings in paper II. An overview of the laboratory facilities is shown in Fig. B.2. Again, as the laboratory contains a large amount of equipment, only the parts relevant to the thesis will be described here.

The main elements used for the experimental verification in paper II were:

- *Four 15 kW ac-dc Converters:* Each converter is formed by a three-leg three-wire four-quadrant ac-dc converter. The outputs of these converters can be connected to the ac panel by using an LC or an LCL filter. They have a dc capacitor in the dc side and an additional uncontrolled rectifier that can be used to maintain the dc voltage constant. Also, each converter includes an isolation transformer with taps that can be connected either to the rectifier side or converter side. Each pair of converters (see the orange square in Fig. B.2) is controlled by a single embedded computer NEXTCOM NISE3140.

- *Two 75 kW ac-dc Converters:* The basic topology of these converters is similar to that of the 15 kW converters. However, one of them has four legs and it is controlled by a single real-time computer. The other one has the standard configuration, but it is connected through the dc side to a 90 kW dc-dc converter, which is used to control the Li-ion battery. The latter ac-dc converter and the dc-dc converter are controlled by using the same real-time computer.

- *One 90 kW dc-dc Converter:* This converter has three legs with standard buck configuration, which are connected through individual L filters to a configurable point. To run a single battery, each leg is connected to the same point and all of them are operated by using interleaved modulation. However, if required, they can be operated separately so that more than one battery can be controlled at the same time.

- *Li-Ion Battery:* This Li-Ion battery is connected to the low-voltage side of the dc-dc converter, and it has a capacity of 47.5 kWh. It is made of small Li-ion modules connected in series and parallel. Its rated voltage is 450 V. The battery is controlled by using a battery management system (BMS), which sends relevant information (state of charge (SOC), current, etc.) to the central controller (implemented in a CompactRIO platform) by using a dedicated CAN bus.

- *Load Banks:* There are two resistive load banks rated at 30 kW. One of them can be used to emulate unbalanced loads. Both banks can be configured in steps of 1 kW through a compactRIO controller. There is also a bank of balanced capacitive loads, which are configured by the same compactRIO platform.

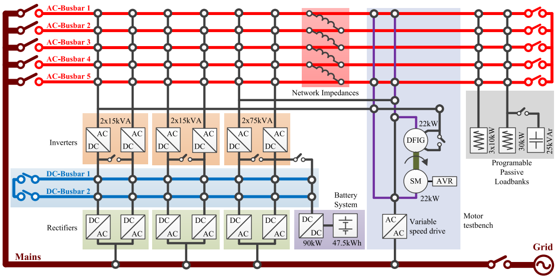

Figure B.2: Electrical diagram of the laboratory, including the main hardware elements.

- *An ac Distribution Panel:* This element is used to interconnect the different devices available in the laboratory. The state of the contactors is managed from a compactRIO platform (the same one used for the loads), which also measures voltages and currents to guarantee the safe operation of the laboratory.

- *A dc Distribution Panel:* The dc sides of all the converters can be interconnected by using a dc distribution panel. The dc panel includes dc breakers and isolation measurements to guarantee the safe operation of the interconnected devices.

- *A Set of Configurable Impedances:* There are five configurable impedances in the laboratory, which can be connected between the different nodes of the ac panel. Both the inductive and resistive parts can be configured independently. This PLC is connected to the CompactRIO so that the impedance can be configured from an external computer.

The primary and internal controllers of power converters are developed in Matlab/Simulink. Then, the controller is translated to c-code, compiled and executed on a real-time computer by using an automatic tool. The secondary part of the controller is formed by different compactRIO platforms and PLCs. These devices are used to automatically manage the laboratory interconnections and protections. All of these devices are connected by using TCP/IP protocol so they can exchange information. This information is also accessible from an external interface developed in Labview that is used to configure the laboratory topology. For extended details of the laboratory facilities, see [93].

ISBN 978-82-326-6149-7 (printed ver.)
ISBN 978-82-326-5358-4 (electronic ver.)
ISSN 1503-8181 (printed ver.)
ISSN 2703-8084 (online ver.)

NTNU
Norwegian University of
Science and Technology